ISSN 0915-6348

NATIONAL INSTITUTE FOR FUSION SCIENCE

The Frontiers of Pulse Power and Particle Beam Technology

W. Jiang (Ed.)

(Received - Apr. 14, 2006)

NIFS-PROC-64 June 2006

RESEARCH REPORT
NIFS-PROC Series

TOKI, JAPAN

The Frontiers of Pulse Power and Particle Beam Technology

Edited by Weihua Jiang

December 5-6, 2005
National Institute for Fusion Science
Toki, Gifu, Japan

Abstract

The papers appeared in this volume of research report have been presented at the "Symposium on Frontiers of Pulsed Power and Particle Beam Technology" held by National Institute for Fusion Science. They report the present status and recent progress in experimental and theoretical studies on pulsed power and particle beam technology and their applications.

Keywords: pulsed power, particle beam, plasma, z-pinch, extreme ultraviolet, x-ray, high power microwave, material processing, pulsed discharge, high voltage, plasma focus.

PREFACE

The collaborative research symposium on "Frontiers of Pulsed Power and Particle Beam Technology" was held at National Institute for Fusion Science (NIFS), Toki, on Dec. 5-6, 2005. This symposium was attended by 36 researchers and students from universities, institutes and industrial companies. At the symposium, 24 research papers were presented, each of them was followed by fruitful discussions. This symposium has provided an excellent environment for information exchange between the researchers and has promoted collaborations between NIFS and universities.

During the symposium, an LHD site tour was given by NIFS staffs especially for this symposium. The attendees have obtained an exceptional opportunity to enjoy a close look at the LHD experimental facilities and listen to the in-depth explanations by the NIFS researchers.

I would like to express my sincere thanks to all of the symposium attendees, all of the paper authors, and the staffs of National Institute for Fusion Science.

Weihua Jiang
Extreme Energy-Density Research Institute
Nagaoka University of Technology

NIFS 2005 Coordinated Research (Symposium)
Project Title: Frontiers of Pulsed Power and Particle Beam Technology
Project ID: NIFS05KKGJ001
NIFS Contact Person: Dr. Teruhiko Tazima

NIFS 2005 Coordinated Research (Symposium)
Frontiers of Pulsed Power and Particle Beam Technology

PROGRAM

Dec. 5 (Monday) (Room 415, Research Bldg. 2)

Chair : K. Ikuta (Tokyo Institute of Technology)

13:30	Current Control of Discharge-Pumped-Plasma EUV Source	Tokyo Institute of Technology	A. Kikuchi, K.Takahashi, M. Masnavi, M. Nakajima, T. Kawamura, M. Shiho, E. Hotta, and K. Horioka
13:50	Conversion Efficiency Calculations of Tin, and Xenon Plasmas for a Discharge-Based Extreme Ultraviolet Source	Tokyo Institute of Technology	M. Masnavi, A. Kikuchi, M. Nakajima (Tokyo Institute of Technology), A. Sasaki, T. Kawamura (Japan Atomic Energy Research Institute), E. Hotta, and K. Horioka
14:10	EUV Generation by Dense Plasma Focus	Gunma University	S. Kamoshida, T. Tsutsui, K. Shimoda, M. Satou
14:30	Dense Plasma Focus Driven by Repetitive High-Current Pulsed Power Generator	Nagaoka University of Technology	Y. Kubota, T. Yokoo, N. Oshima, W. Jiang, K. Yatsui (Nagaoka University of Technology, A. Tokuchi (Nichicon Kusatsu Co.)

14:30~15:00 Break

Chair : K. Takaki (Iwate University)

15:00	High-Energy-Density Physics Researches based on Pulse Power Technology	Tokyo Institute of Technology	K. Horioka, M. Nakajima, T. Kawamura, T. Sasaki, K. Kondo, Y. Yano
15:20	Abrasive Characteristics of DLC Thin Films Deposited by Plasma Ion Implantation	University of Hyogo	M. Yatsuzuka, K.Tomita、Y. Oka,N. Murata, M. Hirota
15:40	Magnesium Energy	Tokyo Institute of Technology	K. Ikuta

16:00~17:30 LHD Site Tour

Dec. 6 (Tuesday) (6F Conference Room, Research Bldg. 1)

Chair : K. Masugata (University of Toyama)

9:00	Application of Pulsed Streamer-like Discharge for Cyanobacteria Blooms Treatment	Kumamoto University	Z. Li, D. Wang, T. Namihira, S. Katsuki, H. Akiyama

9:20	EMTP Simulation for the Design of the Pulsed Power System Using MPC and BPFN	Kumamoto University	J. Choi,T. Yamaguchi, K. Yamamoto, T. Namihira, T. Sakugawa, S. Katsuki and H. Akiyama
9:40	Production of Atmospheric-Pressure Glow Using Inductive Energy Storage System Pulsed Power Generator	Iwate University	K. Takaki, H. Kirihara, C. Noda, S. Mukaigawa, and T. Fujiwara
10:00	Energy Efficiency of Pulsed Plasma Thruster	Tokyo Institute of Technology	T. Ikeda, M. Nakajima and K. Horioka

10:20~10:30 Break

Chair : K. Kamada (Kanazawa University)

10:30	Characteristics of Bipolar-Pulse Generator for Intense Pulsed Heavy Ion Beam Acceleration	University of Toyama	K. Igawa, T. Tomita, I. Kitamura, H. Ito and K. Masugata
10:50	Development of Intense Pulsed Heavey Ion Beam Diode Using Gas Puff Plasma Gun as Ion Source	University of Toyama	H. Ito, M. Higashiyama, S. Takata, I. Kitamura and K. Masugata
11:10	Investigations of the Plasma Dynamics and Emission of Ion Beams and Neutron within the Plasma Focus Device	University of Toyama	H.R. Yousefi, Y. Ejiri, H. Ito and K. Masugata
11:30	Simulation of Multichannel Arc Gap	Nagaoka University of Technology	S. Furuya, S. Suzuki, R. Ogata, S. Takano and J. Irisawa

11:50~13:00 Lunch

Chair : W. Jiang (Nagaoka University of Technology)

13:00	Generation of Microplasmas with a Liquid Materials and Their Characteristics	Tokyo Institute of Technology	N. Shirai, Y. Onaka, N. Nakagawara, S. Ibuka, K. Yasuoka, and S. Ishii
13:20	Plasma Spraying by Electromagnetic Acceleration Using a Copper Particle	Tokyo Institute of Technology	S. Hamada, M. Kanemaru, S. Ibuka, K. Yasuoka, and S. Ishii
13:40	Lasing of Recombination Pumped Soft X-ray Laser	Tokyo Institute of Technology	Y. Sakai, T. Komatsu, Y. Xiao, I. Song, M. Watanabe, A. Okino and E. Hotta
14:00	Development of High Repetition-Rate Pulse Generator Using SI-Thyristor	Nagaoka University of Technology	K. Nakahiro, W. Jiang, K. Yatsui (Nagaoka University of Technology) , M. Wake, K. Takayama (KEK), and N. Shimizu (NGK Insulators Ltd.)

14:20~14:30 Break

Chair : S. Furuya (Nagaoka University of Technology)

14:30	Effect of Focusing Field Error During Final Beam Bunching in Heavy-Ion-Beam Driven Inertial Confinement Fusion	Utsunomiya University	T. Kikuchi, S. Kawata (Utsunomiya University), M. Nakajima, and K. Horioka (Tokyo Institute of Technology)
14:50	5 GHz Superradiance Using Intense Electron Beams with Modified Energy waveforms	Kanazawa University	R. Nakajima, A. Osawa, T. Kurihara, R. Ando, K. Kamada (Kanazawa University) and N. S. Ginzburg (Russian Academy of Sciences)
15:10	The Planning Experiment on a High-Power Magnetron with Transparent Cathode	Nagaoka University of Technology	H. Yamazaki, K. Hashimoto and W. Jiang
15:30	Development of High Power, Short Pulse Large Orbit Gyrotron	University of Fukui, Nagaoka University of Technology	M. Kamada, T. Hayashi, La Agusu, I. Ogawa, T. Idehara, (University of Fukui) V. N. Manuilov (Nizhny Novgorod State University), K. Naito, T. Yuyama, K. Hashimoto, W. Jiang and K. Yatsui (Nagaoka University of Technology)
15:50	Three-Dimensional Particle-in-Cell Simulation of Large Orbit Gyrotron	Nagaoka University of Technology	K. Naito, W. Jiang, and K. Yatsui (Nagaoka University of Technology), M. Kamada and T. Idehara (University of Fukui)

16:10 Close

CONTENTS

List of participants

R. Ando (Kanazawa University)
J. Choi (Kumamoto University)
S. Furuya (Nagaoka University of Technology)
S. Hamada (Tokyo Institute of Technology)
K. Horioka (Tokyo Institute of Technology)
K. Igawa (University of Toyama)
T. Ikeda (Tokyo Institute of Technology)
K. Ikuta (Kawai Sekitan Kogyo Co., Ltd.)
H. Ito (University of Toyama)
W. Jiang (Nagaoka University of Technology)
K. Kamada (Kanazawa University)
M. Kamada (University of Fukui)
S. Kamoshida (Gunma University)
A. Kikuchi (Tokyo Institute of Technology)
T. Kikuchi (Utsunomiya University)
Y. Kubota (Nagaoka University of Technology)
T. Kurihara (Kanazawa University)
Z. Li (Kumamoto University)
K. Masugata (Toyama University)
M. Masnavi (Tokyo Institute of Technology)
K. Naito (Nagaoka University of Technology)
R. Nakajima (Kanazawa University)
K. Nakahiro (Nagaoka University of Technology)
T. Namihira (Kumamoto University)
A. Osawa (Kanazawa University)
Y. Sakai (Tokyo Institute of Technology)
M. Sato (Gunma University)
N. Shirai (Tokyo Institute of Technology)
T. Tazima (NIFS)
K. Takaki (Iwate University)
D. Tanaka (Kanazawa University)
T. Uchida (Gunma University)
M. Watanabe (Tokyo Institute of Technology)
H. Yamazaki (Nagaoka University of Technology)
M. Yatsuzuka (University of Hyogo)
H. Yousefi (University of Toyama)

Current Control of Discharge-Pumped-Plasma EUV Source

Atsushi Kikuchi,* Kensaku Takahashi, Majid Masnavi, Mitsuo Nakajima,
Tohru Kawamura, Makoto Shiho, Eiki Hotta, and Kazuhiko Horioka
Department of Energy Sciences, Interdisciplinary Graduate School of Science and Engineering, Tokyo Institute of Technology, 4259 Nagatsuta, Midori-ku, Yokohama 226-8502, Japan

To generate a high efficiency extreme-ultraviolet (EUV) source, effects of current profiles for controlling radiative plasmas based on xenon capillary discharge are experimentally investigated. Results obtained by a two-step current discharge show that the pinching phase can be maintained at a quasi-steady state by the additional current, and the plasma condition depends on the timing of the current in the pinching phase. Results also indicate that the two-step current discharge scheme is effective for prolonging the emission period of radiative plasma based on Z-pinch discharge. The current profile seems to have a significant potential for enhancing the conversion efficiency of capillary-discharged plasma.

Keywords: EUV source, Z-pinch, tapered capillary, high energy density plasma, conversion efficiency, double-pulse discharge

I. INTRODUCTION

Development of photolithographic technology for high performance semiconductor devices depends strongly on exposure wavelength of a light source. Up to now, the fine processing in the technology for projecting circuits onto a silicon wafer surface has been made possible by continuous reduction in the exposure wavelength. An extreme-ultraviolet (EUV) light source at around 13 nm is expected to be the most promising candidate for next generation lithography[1]. An effective wavelength region is limited in ±1% bandwidth centered at 13.5 nm, called in-band, due to the reflection characteristic of multilayer-coated optics, which is created based on Mo/Si mirrors, applied to EUV lithography system[2]. For the requirements such as at extremely short wavelength and within narrow bandwidth, radiation emitted from specific ions in a high energy density plasma generated with a compact device is likely to be the most effective source for semiconductor industry.

Three ionic systems (Xe, Sn, and Li) are of great interest as the efficient EUV emitter because of their potential for holding intense spectra within the above effective bandwidth[3–9]. Xe is an inert gas and thus has significant advantages with respect to easy-to-use as a target material, free from macro-particle debris and simple setup in comparison with other two solid-targets' at room temperature, which need complicated equipments such as target supply and removal systems.

Thus far, two major technologies for generating a plasma EUV source, gas discharge-pumped-plasma (DPP) and laser-pumped-plasma (LPP), have been widely investigated[3–9]. In DPP, the electrical energy stored in a capacitor bank is directly converted into the energy of emitting plasma. Therefore, DPP has several advantages from the viewpoints of high conversion efficiency (CE) from primary electrical energy to EUV, compact design and low cost compared with LPP.

Due to above-described points, we are investigating EUV emitting plasmas based on a Xe capillary discharge. The capillary discharge is probably one of the easiest configurations for generating EUV radiation in DPP. However, source components are inherently close to the hot plasma and are thereby exposed by large heat load. Furthermore, typical CE obtained in DPP are small, and this means that an enormous input power, at least over several tens of kilowatts, is required[10]. From these points of view, the most crucial issue for development of EUV sources based on discharge is to meet the required high output power in combination with the long lifetimes of source components[11]. Therefore, to meet these antithetical demands together, plasma conversion efficiency (PCE) defined as ratio of EUV in-band radiation to energy of emitting plasma[10, 12–14], which is quite low and dominates the total CE, has to be improved. It appears that the reason of low PCE is attributed mainly to short emission duration of Z-pinch based plasmas, which transiently fulfill the condition of plasma such as electron temperature (T_e) and electron density (n_e) suitable for emitting in-band radiation.

To improve the low CE, the radiative plasma has to be maintained as an EUV in-band source much longer. The photon energy of the emitted radiation depends on target material, ionization stage, and electron transition. The ionization stage is basically determined by the plasma parameters, T_e and n_e. In Xe plasma, the transitions responsible for in-band radiation occur only in ten-times-ionized Xe (Xe XI). For the radiation based on Xe XI, the plasma parameters have to be increased up to appropriate values, for instance $T_e \sim 30 - 40$ eV and $n_e \sim 10^{18} - 10^{19}$ cm^{-3}[10, 15]. For the generation of a long emission EUV source, the radiative plasma must be maintained at appropriate condition in a quasi-steady state. However, plasma parameters in pinching phase are dynamically controlled by the main discharge parameters such as capillary radius, initial gas pressure, and the cur-

*Electronic address: g04m3112@es.titech.ac.jp

rent shape. Then, in Z-discharge, the plasma transiently evolves through the optimum condition for in-band radiation during the pinching process. The plasma-dynamics in radial direction is principally controlled by the self magnetic field of the current pulse. Therefore, only the current has a significant potential for maintaining the radiative plasma as a radiation source at a quasi-steady state[16].

This paper reports the effects of current profiles for controlling radiative plasmas based on Xe capillary discharge experiments. Double-pulse discharge using a two-step current was selected for confining a pinch plasma at a quasi-steady state due to its simple system. In this study, the main purpose is to carry out the initial evaluations of the plasma-characteristics affected by an additional current. Therefore, the experiments using a waveform superimposed with two sinusoidal-like currents were performed only for the purpose of proof-of-principle. The radiative plasmas were generated with a tapered capillary and an X-ray diode was used to measure the time evolutions of plasma radiation.

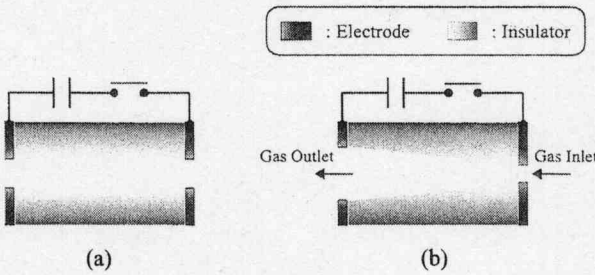

FIG. 1: Schematic of capillary shape (a) Conventional capillary (b) Tapered capillary.

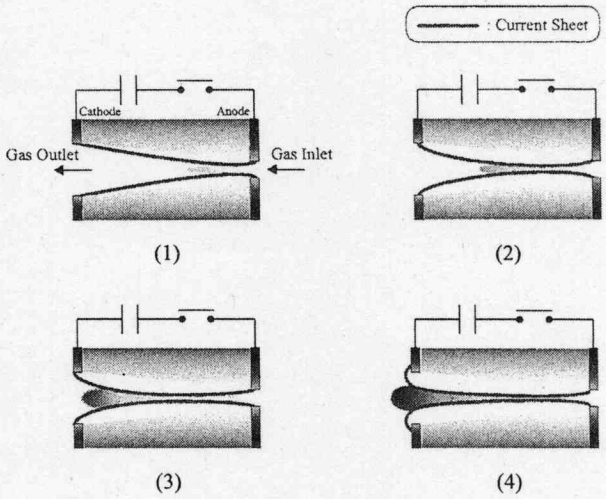

FIG. 2: Pinching-process in tapered capillary.

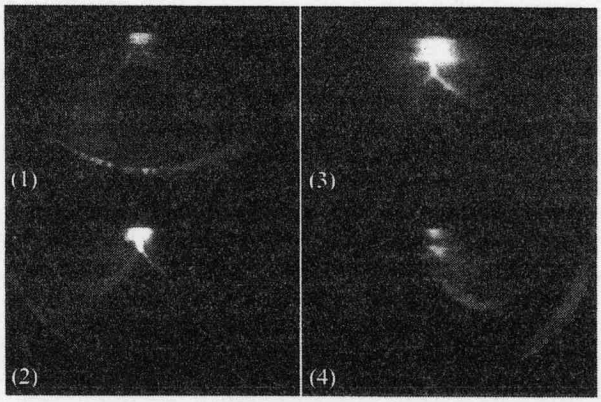

FIG. 3: Typical time evolution of Xe plasma profile.

II. EXPERIMENT

A. Plasma-dynamics in tapered capillary

Behaviors of Xe plasma in a tapered capillary have been experimentally investigated to evaluate its possibility for a bright EUV radiation source[17]. The tapered capillary discharge is suggested to generate a hot and point-like plasma outside of the capillary for the purpose of increasing collection solid angle and suppression of heat load to the source components in comparison with conventional capillary discharges. A schematic view of the conventional capillary with constant cross section is shown in Fig.1(a), and that of the tapered one in Fig.1(b). Xe gas is used as the working medium and supplied with supersonic injection through the tapered capillary from right (small radius) side to left (large radius) side in the figure.

Plasma-dynamics in the tapered capillary is different substantially from that in the conventional one. Figure 2 shows a conceptualistic pinching process in the tapered capillary. In the figure, the solid lines connecting both electrodes indicate current sheets and the objects wedged between the lines are transient plasmas. As shown, at first a pulse generator drives a high-current in Xe gas inside the capillary (Fig.2(1)). After that, a discharge plasma is compressed by magnetic pressure driven by self-magnetic field, so-called pinch effect. Note that, there exists a gradient of capillary-radius in the gas flow direction. The magnetic pressure of cylindrical plasma (P_B) is expressed simply

$$P_B \propto \frac{I^2}{r^2} \tag{1}$$

where I is the discharge current and r is the plasma-radius. As shown in the above equation, P_B varies depending on the location with different r along discharge axis inside the tapered capillary. Therefore, pressure difference is induced not only in radial direction but in ax-

ial direction ((Fig.2(2),(3)). Consequently, a hot dense pinch plasma, as a point-like source, is generated at downstream of the capillary (Fig.2(4)). A typical time evolution profile of Xe plasma observed by a fast framing camera (HADLAND PHOTONICS : Imacon 468) is shown in Fig.3. The pinch plasmas are ejected from the upper side toward the downside in the figure and their images are recorded by the camera through an acrylic window at the vertical direction to the discharge axis.

B. Double-pulse discharge

An ordinary discharge current has a LCR damped oscillation waveform, as shown in Fig.4(a). As mentioned at the closing paragraph of introduction, double-pulse discharge scheme using a two-step current (Fig.4(b)), is suggested to control the radiative plasma for prolonging the emission period.

The concept of the double-pulse discharge is roughly described as follows. A high current pulse driven by a first discharge starts to compress the cylindrical plasma. The plasma condition for EUV radiation is generally achieved with the maximum pinch at almost the same time as the current reaches at its peak. The second current is driven in the pinching phase before the plasma expands and it prevents the plasma to get out of the optimum condition for EUV radiation. Owing to the additional current, the pressure balance between the fluidic and magnetic pressure is controlled, and consequently the pinch plasma is maintained at a quasi-steady state, depending on the additional current profile.

The radiation source is characterized by the measurements of time evolution of EUV-signals obtained by an X-ray diode. The radiation characteristics observed by the double-pulse discharge are compared with the results of conventional single-pulse discharge. As a series of early-stage experiments, the measurements are performed for different delay time, which is defined as time interval from the start of the first discharge to that of the second discharge.

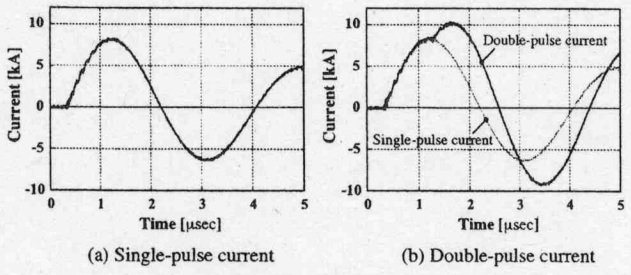

FIG. 4: Typical current waveform (a) Single-pulse (b) Double-pulse.

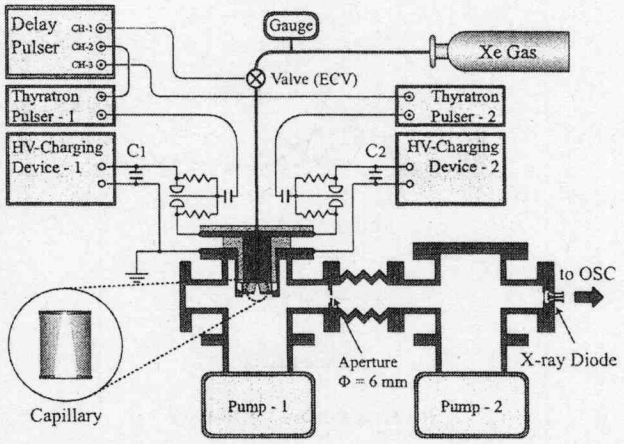

FIG. 5: Schematic of tapered-capillary discharge system.

C. Experimental setup

A schematic diagram of the experimental arrangement is shown in Fig.5. The capillary-length is 10 mm, inlet-diameter is 2 mm, and outlet-diameter is 5 mm. The cross section is gradually enlarged with constant gradient along the discharge axis. In addition, the capillary has a Laval nozzle structure and therefore Xe gas is accelerated through it with supersonic speed. This configuration is advantageous to recover the initial condition inside the capillary tube after discharge. The gas supply is controlled with an electrically controlled valve (ECV) for pulsed flow. As shown in the figure, two electrical circuits are used to investigate the effects of current shape for controlling the radiative plasmas, especially that of additional current for confining the pinch plasma at a quasi-steady state. A capacitor bank with capacitance of 0.4 μF is used in each circuit. Typically, the capacitor C_1 for the first discharge circuit was charged to 16 kV

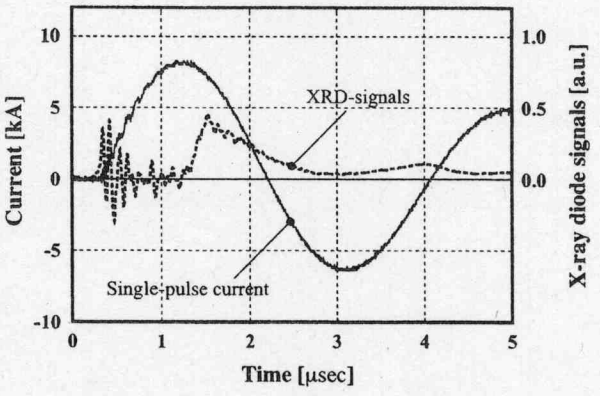

FIG. 6: Typical waveforms of discharge current and XRD-signals obtained by a single-pulse discharge.

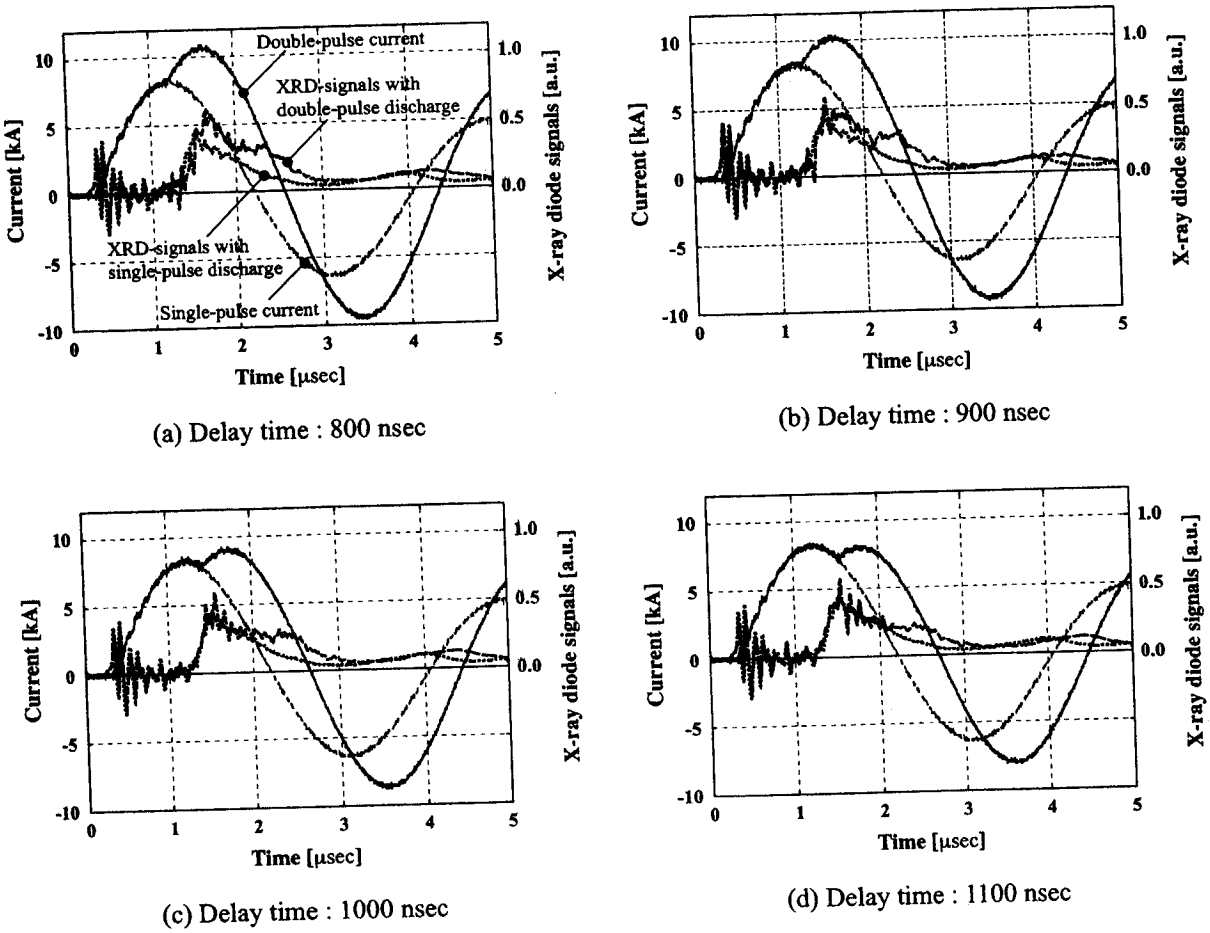

FIG. 7: Effects of current shapes on XRD-signals.

and C_2 for the additional discharge circuit to 10 kV. The X-ray diode (XRD), which has a gold photocathode of 20 mm diameter, is located at the vertical direction to the discharge axis and used to measure the time evolutions of EUV-signals from the pinch plasmas only ejected from the capillary. Bias voltage of the XRD was 500 V at negative polarity. The discharge and the measurement chamber are separated by an aperture of 6 mm diameter for differential pumping in order not to cause electric breakdown at the XRD. The center of the aperture is arranged in the same straight line with the optical path from exit of the capillary to the XRD. These chambers are evacuated to a pressure of less than 10^{-4} Torr by turbo-molecular pumps in combination with rotary vacuum pumps, respectively. The discharge current is measured by a Rogowski coil.

Although it is necessary to use semiconductor switches for highly repetitive discharges in commercial application, discharges are initiated by triggered spark gaps in this series of experiments, because the main purpose of this study is to confirm the principle; i.e., the effects of the additional current. Open time of the ECV, and timings of the first and the second discharge are controlled by a delay pulser. Initial gas density was defined by stagnation pressure fixed at 0.1 MPa, at upstream of the ECV.

III. RESULTS AND DISCUSSIONS

Typical results obtained by a single-pulse discharge are shown in Fig.6. In the figure, solid line and dot-line indicate a discharge current pulse and a time evolution of XRD-signal, respectively. A peak current of 8.15 kA was obtained. As shown, the plasma starts to radiate at the time of the current peak. This means that a high energy density plasma was ejected outside the capillary at that time.

Figure 7 shows a comparison of double-pulse discharge experiments and a single-pulse experiment with delay time of additional current as a parameter. Waveforms of discharge current and time evolutions of the plasma radiation obtained with delay time of 800 ns, 900 ns, 1000 ns, and 1100 ns are shown, respectively, in Figs.7(a), (b), (c), and (d). As shown, typical results of single-pulse

discharge are overlaid for comparison.

In Fig.6, the waveform of plasma radiation is monotonically decreasing after its peak value. In contrast to this result of single-pulse discharge, figure 7 shows that the radiation waveform obtained by the double-pulse discharge has a flat top region during about 2.0 - 2.5 μs in all of the figures. Furthermore, the shape at the flat top region are different by the addition timing of second current. This means that the pinching phase can be maintained at a quasi-steady state by the additional current, and besides, the plasma condition depends on the timing of second current in the pinching phase. In Fig.7(a), the second current pulse and the radiation waveform are respectively reached at each peak point approximately at the same moment, therefore the highest value of XRD-signals at the flat top region is obtained of the four results. As shown in Fig.7, the later the delay time is, the lower the value of the flat top is. In Fig.7(d), the addition timing of second current is obviously too late to maintain the pinch plasma as a hot and dense state. These results show existence of an optimum timing of the second current in the double-pulse discharge.

IV. SUMMARY

We have investigated the effects of two-step current profiles for controlling radiative Xe plasmas based on tapered capillary discharge. The experimental results indicate that the pinching phase can be maintained at a quasi-steady state by the additional current, and besides, the plasma condition depends on the addition timing of the second current in the pinching phase. From the results reported here, it was demonstrated that the current control is effective for maintaining a radiative plasma in the pinching phase at a quasi-steady state and thus has significant potential for enhancing the plasma conversion efficiency of the capillary-discharged EUV source. However, double-pulse discharge experiments using two sinusoidal-like currents were performed only for the purpose of proof-of-principle, and optimizations of current profile were not subsequently implemented. We are planning to confirm the radiation characteristic of discharge-pumped plasma EUV sources, and also to improve the current profile for efficient EUV plasmas.

Acknowledgments

This work was partly supported by NEDO (New Energy and Industrial Technology Development Organization) and EUVA (Extreme Ultraviolet Lithography System Development Association).

[1] D. Attwood, *SOFT X-RAYS AND EXTREME ULTRAVIOLET RADIATION: Principles and Applications* (Cambridge, New York, 1999)

[2] C. W. Gwyn, R. Stulen, D. Sweeney and D. Attwood, J. Vac. Sci. Technol. B **16** , 3142 (1998)

[3] M. A. Klosner and W. T. Silfvast, Opt. Lett. **23**, 1609 (1998)

[4] E. R. Kieft, J. J. A. M. van der Mullen, G. M. W. Kroesen and V. Banine, Phys. Rev. E **68**, 056403 (2003)

[5] U. Stamm, J. Phys. D **37**, 3244 (2004)

[6] E. R. Kieft, J. J. A. M. van der Mullen, G. M. W. Kroesen, V. Banine and K. N. Koshelev, Phys. Rev. E **71**, 026409 (2005)

[7] M. A. Klosner and W. T. Silfvast, Appl. Opt. **39**, 3678 (2000)

[8] M. A. Klosner, H. A. Bender, W. T. Silfvast and J. J. Rocca, Opt. Lett. **22**, 34 (1997)

[9] G. Schriever, K. Bargmann and R. Lebert, J. Appl. Phys. **83**, 4566 (1998)

[10] T. Krüchken, K. Bargmann, L. Juschkin and R. Lebert, J. Phys. D **37**, 3213 (2004)

[11] U. Stamm, J. Kleinschmidt, K. Gäbel, H. Birner, I. Ahmad, D. Bolshukhin, J. Brudermann, T. D. Chinh, F. Flohrer, S. Götze, G. Hergenhan, D. Klöpfel, V. Korobotchko, B. Mader, R. Müller, J. Ringling, G. Schriever, C. Ziener, Proc. of SPIE. **5374**, Emerging Lithographic Technology VIII, 133 (2004)

[12] M. Masnavi, M. Nakajima and K. Horioka, J. Plasma and Fusion Res. **79**, 1188 (2003)

[13] M. Masnavi, M. Nakajima, A. Sasaki, E. Hotta and K. Horioka, Jap. J. Appl. Phys. **43**, 8285 (2004)

[14] M. Masnavi, M. Nakajima, A. Sasaki, E. Hotta, and K. Horioka, Appl. Phys. Lett. **87**, 111502 (2005)

[15] M. Masnavi, M. Nakajima, T. Kawamura, E.Hotta and K. Horioka, NIFS-PROC-**61**, 10 (2005)

[16] K. Horioka, E. Hotta, A. Okino, T. Kawamura, M. Nakajima, M. Watanabe, M. Masnavi, S. R. Mohanty, S. Inho, A. Kikuchi, K. Takahashi, Proc-2005 EUVL Symposium, Sandiego, 2-SO-27, (2005)

[17] K. Horioka, E. Hotta, M. Shiho, M. Nakajima, T. Kawamura, M. Masnavi, N. Sakamoto, A. Okino, M. Watanabe, I. Song, A. Kikuchi, K. Iwata, Y. Honma, ISPP-2004;Proc. 5th Int.Sym. Pulsed Power and Applications, KERI Korea, (2004)

Conversion efficiency calculations of tin, and xenon plasmas for a discharge-based extreme ultraviolet source

M. MASNAVI, A. KIKUCHI, M. NAKAJIMA, A. SASAKI,† T. KAWAMURA, E. HOTTA, and K. HORIOKA

Department of Energy Sciences, Interdisciplinary Graduate School of Science and Engineering, Tokyo Institute of Technology, 4259 Nagatsuta, Midori-ku, Yokohama 226 - 8502, Japan

† Advanced Photon Research Center, Japan Atomic Energy Research Institute, 8-1 Umemidai, Kizu-cho, Souraku-gun, Kyoto 619-0215, Japan

Extreme ultraviolet (EUV) discharge-based lamps for EUV lithography (EUVL) need to generate extremely high-power in the spectrum band 13.5 ± 0.135 nm. A simplified model including steady-state collisional-radiative, and radiative transfer equation was developed to investigate the wavelength-integrated output lights in xenon (Xe), and tin (Sn) plasmas. Results indicate that higher conversion efficiencies compared to the so-called efficiency of a black-body source are formed in non-local thermodynamic equilibrium (non-LTE) region, viz., a suitable electron density region of discharge-produced plasmas. Due to the higher opacity of resonance transitions in Sn plasma, the optimum electron density region to maximize conversion efficiency of Sn-based source is an order lower than Xe case.

Keywords: extreme-ultraviolet lithography, EUV source, conversion efficiency, Z discharge, radiant exitance, opacity, collisional-radiative model

I. Introduction

Pulsed power generator-based Z discharge plasmas have proved to be an effective radiation source in the soft x-ray, and EUV spectrum bands. The latter is of great commercial interest because it is the extension of today's optical lithography toward a shorter wavelength. [1] In spite of the tremendous progress in the development of discharge EUV sources over the last several years, only Sn material demonstrated a large conversion efficiency (CE) of input power to emission in 2% bandwidth centered at wavelength λ = 13.5 nm, the so-called in-band radiation. Still, the failure in the heat removal from a discharge tube at the high input power level dictates us further investigation toward optimization of CE. Thereby, calculation results of the optimum regions of CE and spectral efficiency in the electron density-temperature space are presented for Xe, and Sn ions. Calculations have done using detailed atomic data of HULLAC code for charge states ranging from Xe^{8+}-Xe^{17+}, and Sn^{4+}-Sn^{13+}. Opacity effects on all of the level populations and line-broadening are considered using escape factor for a cylindrical geometry. The detailed calculation model and discussion will be reported elsewhere.

author's e-mail: majid@es.titech.ac.jp

II. Results

For a steady-state black-body radiator, viz., when the plasma is in LTE condition, CE is defined by fraction of the integrated radiant exitance, M_λ, in a wavelength interval and total plasma radiation, [2] as shown in Fig. 1.

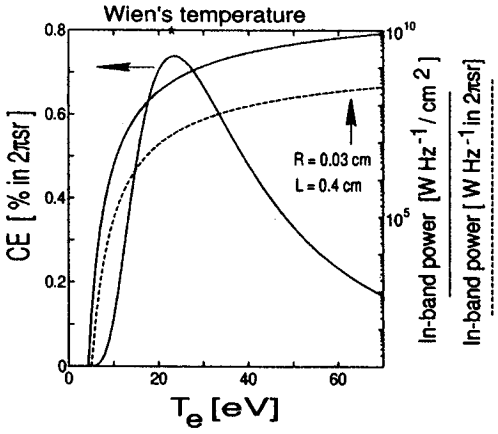

Fig. 1 CE of a black-body radiator (% in 2πsr) vs electron temperature T_e. Total in-band radiant exitance M_λ and corresponding M_λ for a cylindrical plasma with radius R = 0.03, and length L = 0.4 cm, are also shown.

In a low electron density n_e region relevant to discharge-based sources, the plasma is in non-LTE condition and different parts of spectrum saturated in different n_e region, since the transitions have different oscillator strength. With going to high n_e region, finally, the distribution of line transitions are same as gA distribution. [3] Here, g and A are the statistical weight and radiative decay rates of transitions, respectively. Therefore, it is worthwhile to find out optimum n_e region for maximizing CE using a collisional-radiative model.

A simple energy-balance equation of the following form is used to estimate maximum of CE for Z discharge type source

$$K = E_I + Y + E_l, \tag{1}$$

where K is the kinetic energy of plasma in implosion phase, E_I is the plasma internal energy, Y is the energy yield by radiation (namely, total radiated power, or, radiant exitance times emission duration), and E_l contains energy losses in neglected processes, for example, radiation from other excitation before pinching time (i.e., maximum compression). We assumed that E_l =0. This assumption is not so bad, when we take into account effect of Joule heating, in particular, in short pulse current. Please, note that, since the coupling efficiency of pulsed power to kinetic energy of plasma strongly depends on design of such systems and also initial plasma conditions, Eq. (1), does not include this factor. Thereby, the maximum CE can be written as [4,5]

$$\mathrm{CE(in\ 4\pi sr)} = \frac{\sum M_{\lambda 2\%} S_p \tau}{\sum M_\lambda S_p \tau + E}, \tag{2}$$

where $M_{\lambda 2\%}$ is the radiant exitance of transitions inside in-band region, S_p is plasma surface, τ is emission duration, and E is defined as the minimum energy needed to heat and ionize a plasma to a given ionization state for Xe case, and plus the cohesive energy for Sn plasma (3.14 eV/atom for Sn [6]). Equation (2), clearly implies that τ is of key importance in optimization of CE.

Typical ionization fractions of Xe, and Sn plasma vs T_e at steady-state approximation are shown in Figs. 2(a) and 2(b) for $n_e = 10^{18}$ cm^{-3}. Moreover, stem representations of M_λ for Xe, and Sn plasmas at two different n_e for a fix plasma dimension of R = 0.03, and L = 0.4 cm are shown in Figs. 3(a)-(b), and 4(a)-(b), respectively.

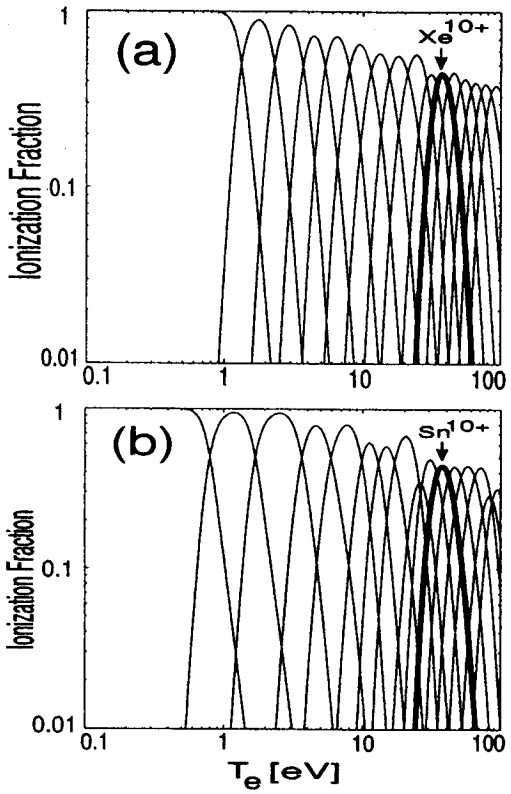

Fig. 2 (a) Ionization fraction of Xe, and (b) Sn, at n_e = 10^{18} cm^{-3}.

In Sn case, many charge states contribute to in-band region, while major contribution to in-band region in Xe plasma is due to the ten-times-ionized Xe.

Figures 5(a) and 6(a) represent contours of CE (% in 2πsr) vs n_e and T_e, for Xe, and Sn plasmas, respectively. Plasma conditions span for n_e and T_e, while keeping photon path length (R = 0.03 cm) constant. According to étendue limit ($\leq$ 3.3 mm^2 sr), the plasma length (L) assumed to be 0.4 cm. Additionally, Figs. 5(a) and 6(a) illustrate contours of emission durations, τ (dashed-line), log-scale, in units s. In fact, a realistic calculation of CE requires information about the plasma temperature-density history. For a gas-discharge cylindrical plasma column, some efforts have been made to model its dynamics such as the snowplow model and the slug model, or magneto-hydrodynamic (MHD) calculation. These calculations can be done [4] but they often shift the focus of calculation to fluid dynamics in most cases. Because we are interested primarily in the kinetics behavior, we estimated τ using different approach.

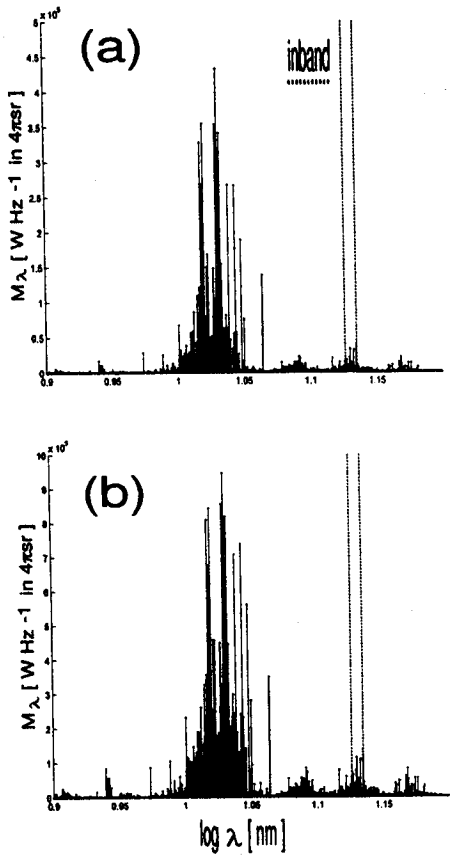

Fig. 3 Typical stem representation of M_λ of Xe at (a) n_e = 5 × 10^{18} and (b) 10^{19} cm^{-3}.

In Z discharge type transient plasmas τ is governed by (1) characteristics timescales of hydrodynamic behavior (2) ionization (τ_i), and recombination times of given ionization state at pinching phase. Thus, to estimate τ in Figs. 5(a) and 6(a), we have considered shorter time between (1) inertial confinement time (τ_c) and (2) ionization time of dominant charge state. Additionally, we introduced other time scale τ_l, viz., the time required when thermal energy of plasma converts to total radiation. Therefore, if τ_l being shorter than τ_i and τ_c, we consider this time. Comparing Figs. 5(a) and 6(a) reveals that CE in the Sn-plasma becomes maximize in low n_e compared to the Xe case, owing to the higher opacity of resonance transitions in the in-band region. With the increasing density, CE of Sn-based source continuously drops down, i.e., the spectral intensity distributions for all of the transitions approach to their intrinsic spectral radiance.

Assume that, plasma in duration τ, is magnetically confined and it is in ionization balance situation, namely, the ionization and recombination fluxes are the same. If we consider additional heating compensates radiation loss, for example Joule heating, in this case, we expect that CE approaches to the spectral efficiency (η), viz., put E = 0 in Eq. (2). Figures 5(b) and 6(b) show contours of η vs n_e and T_e for Xe, and Sn ions. Comparing Figs. 5(b) and 6(b) shows that the optimum spectral efficiency region of Sn-metal occurs at lower n_e compared to Xe. This characteristic and the fact that many charge states of Sn contribute to the in-band radiation are important in the magnetically confined Sn-based EUV source.

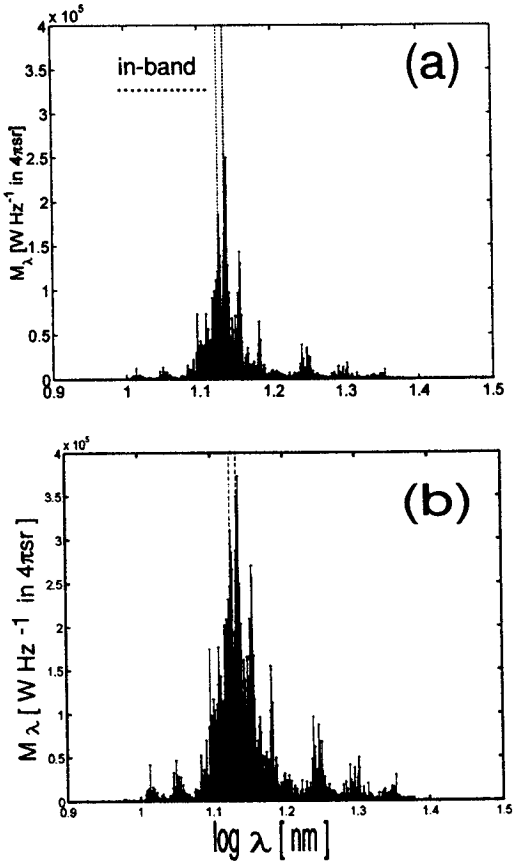

Fig. 4 Typical stem representation of M_λ of Sn at (a) n_e = 5 × 10^{18} and (b) 10^{19} cm^{-3}.

III. Conclusions

The calculation results show that large conversion efficiencies of Xe ($\simeq$ 0.45 % in 2πsr), and Sn-metal ($\simeq$ 3 % in 2πsr) plasmas are formed for the electron den-

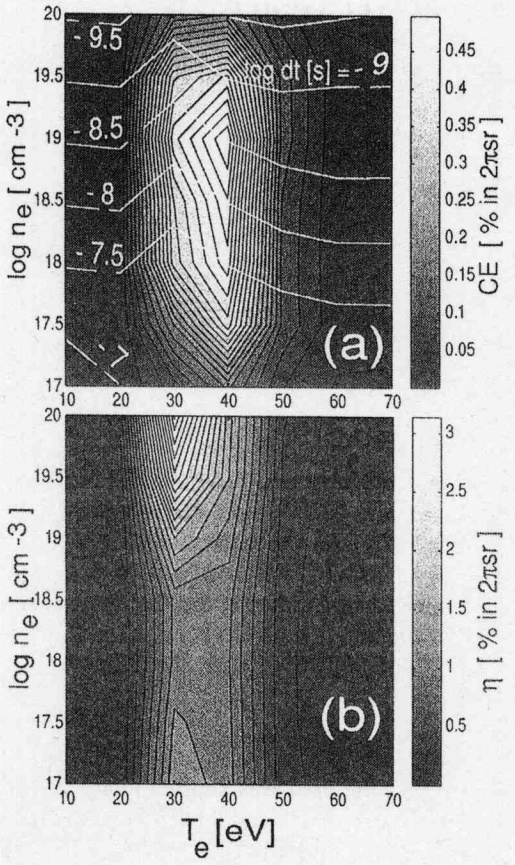

Fig. 5 (a) Contour of CE (% in 2πsr) for Xe plasma and log τ (s) which designated as dashed-line vs n_e and T_e for a cylinder plasma with 0.06 cm in diameter and 0.4 cm long. (b) Spectral efficiency η (% in 2πsr) vs n_e and T_e.

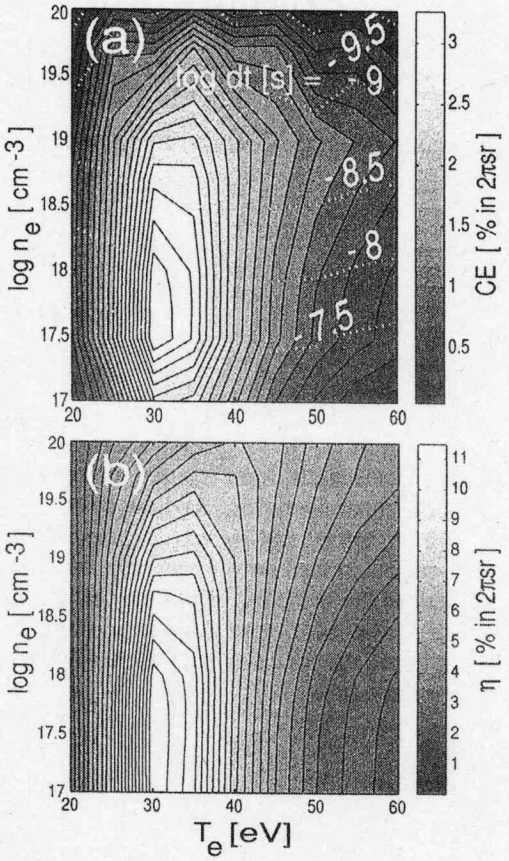

Fig. 6 (a) Contour of CE (% in 2πsr) for Sn plasma and log τ (s) which designated as dashed-line vs n_e and T_e for a cylinder plasma with 0.06 cm in diameter and 0.4 cm long. (b) Spectral efficiency η (% in 2πsr) vs n_e and T_e.

sity less than 10^{20} cm^{-3}. In Xe, $n_e \simeq 10^{19}$ cm^{-3}, $T_e \simeq 40$ eV, and in Sn case, $n_e \simeq 10^{18}$ cm^{-3}, $T_e \simeq 30$ eV, are estimated to be optimum regions for maximizing CE in discharge-based EUV source. The optimum region of the spectral efficiency of Sn plasma ($\eta \simeq 11$ % in 2πsr) occurs in very lower electron density region compared to Xe case.

Acknowledgments

The present work is partly supported by NEDO (New Energy and Industrial Technology Development Organization) and EUVA (Extreme Ultraviolet Lithography System Development Association) of Japan.

References

[1] See, for example, several presentations in, *International EUVL Workshop*, 27 February 2005, San Jose, CA. Available online: http://www.sematech.org; Directory: resources/litho/meetings/euvl/20050227/.

[2] M. A. Bramson, *Infrared Radiation, A Handbook for Applications* (Plenum, New York, 1968) p. 68.

[3] R. Radtke, Biedermann, J. L. Schwob, P. Manderlbaum, P. Doron, Phys. Rev. A **64**, 012720 (2001).

[4] M. Masnavi, M. Nakajima, A. Sasaki, E. Hotta, and K. Horioka, Appl. Phys. Lett. **87**, 111502 (2005), and references therein.

[5] T. Aota and T. Tomie, Phys. Rev. Lett. **94**, 015004 (2005).

[6] A. Anders, Appl. Phys. Lett. **80**, 1100 (2002).

Dense Plasma Focus Driven by Repetitive High-Current Pulsed Power Generator

Yugo Kubota, Tomoyuki Yokoo, Nobuaki Oshima, Weihua Jiang, Kiyoshi Yatsui

Extreme-Energy Density Research Institute, Nagaoka University of Technology, Japan

Akira Tokuchi

Nichicon Kusatsu Corporation, Japan

Abstract

A short wavelength light source is required for a resolution improvement in optical lithography of semiconductor manufacturing. And the development of extreme ultraviolet (EUV) light source with wavelength of ~ 13.5 nm is carried out by various research organizations. In this study, the experiments for EUV generation with high-current pulsed power generator have been carried out. And a plasma focus diode is used as a load. This paper describes the behavior of plasma that is observed by a high-speed camera during the discharge of 200 Hz burst mode. It was confirmed that the plasma has focused at a tip of the anode with the conditions of 40 Pa and 60 Pa. But it was not focusing with 80 Pa. When one compares the 1st and 900th discharge, the timing of focusing is about the same time.

I. Introduction

The fine processing technology of semiconductors is improving year by year and the semiconductors have made a high integration with a speed of 4 times at three years as it is known "Moore's Law". This high integration is supported by the development of optical lithography technology. A minimum process size in optical lithography follows Rayleigh's equation $R=k_1 \cdot \lambda/NA$ [1]. Where R, k1, λ and NA are resolution, proportionality factor, wavelength of light source and numerical aperture respectively. From here it is found that the more the wavelength of light source shortens, the more the minimum process size shrinks. In fact in optical lithography, g-line λ=436 nm), i-line (365 nm), KrF excimer laser (248 nm), ArF excimer laser (193 nm) have used as light source. And extreme ultraviolet (EUV) is presently drawing attention as light source of next generation for aspire to becoming more miniaturization [2].

It is known that EUV is radiated from Xe^{10+} ions. There are laser produced plasma (LPP) method [3] and discharge produced plasma (DPP) method [4] to generate this kind of high-temperature and high-density xenon plasma. In this study, research on generation of EUV light source by DPP has been carried out in consideration of the advantage that equipments are inexpensive price and a conversion efficiency is higher than LPP. A pulsed power generator has designed and manufactured, and operation tests have been demonstrated on the condition that the load was shorted along the way. A peak current was 40 kA and a pulse width was 400 ns with the load was shorted. [5]

This paper describes results of discharge tests with a plasma focus diode fits as the load in the generator. Changes of behavior of plasma associated with differences of a pressure in the chamber and the number of discharge were observed by a high-speed camera.

II. Experimental Setup

High-current pulsed power generator

The high-current pulsed power generator is required to produce pinch plasma by DPP. The value of current to cause pinch phenomenon is determined by the Bennett's equation [6]. The generator has designed and manufactured for EUV generation by DPP. The circuit diagram of the generator is shown on Fig.1. The circuit of this generator consists of a resonant charging unit (RCU) using semiconductor switch IGBT and a magnetic pulse compression (MPC) [7,8] unit.

In the RCU, a capacitor C_{DC} is charged through a resistor by DC power supply. After that, the current flows through a transformer TR by controlling switching operation of IGBT switch SW_1 and SW_2. A capacitor C_0 is charged with a pulse width that is dependent on the C_0 capacity and inductance of the secondary winding. In the MPC unit, when an IGBT switch SW_3 is closed and a magnetic switch MS_0

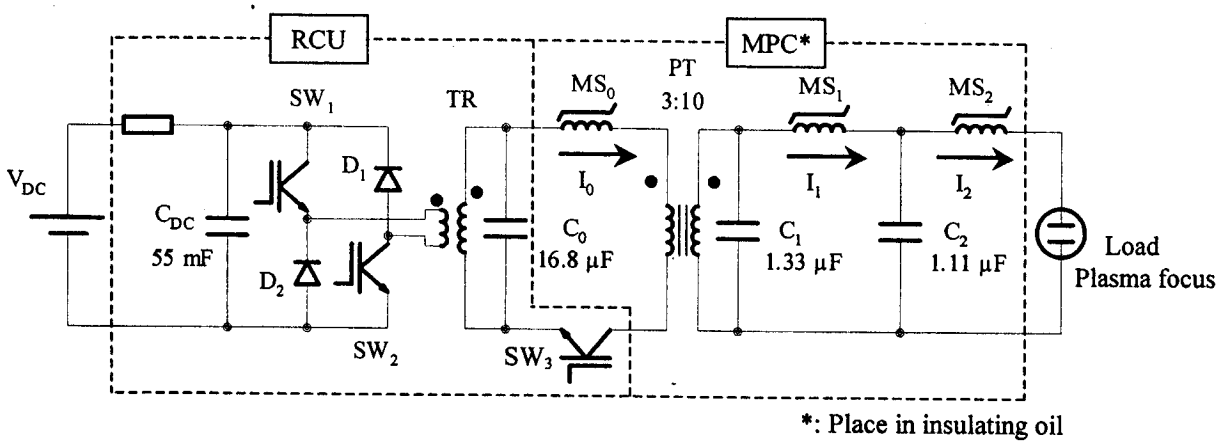

Figure 1. Circuit diagram of the pulsed power generator

saturates, a capacitor C_1 is charged by current flow through a pulse transformer PT with turn ratio is 3:10. The MS_0 is used for the purpose of reduction of energy dissipation in the SW_3. The SW_3 consists of IGBTs of 2 in series and 14 in parallel. After C_1 is charged, the energy is transferred from C_1 to the load via two-stage magnetic switches MS_1 and MS_2. The C_2 capacity is 1.11 μF and a voltage applied is approximately 4.2 kV. Therefore, a stored energy is approximately 10 J. The generator has coaxial structure for the purpose of inductance reducing. An inductance of C_2 – load loop that was calculated using the pulse width with shorted load was approximately 15.2 nH. This generator can operate at repetition rate of 200 Hz in continuous mode or 1 kHz burst mode. A chamber is directly connected with the generator, which is evacuated by rotary pump and turbo-molecular pump.

Plasma focus diode

A dense plasma focus (DPF) [9,10,11] with plasma focus diode has been used as the load. Figure 2 illustrates the load arrangement. The following is the principle of operation of DPF. First, when the high-voltage is applied between an anode and a cathode, a sheet plasma formed between the electrodes due to occur flashover discharge at the surface of insulator. This plasma sheet that is accelerated by the Lorentz force moves rapidly to the tip of the anode, which eventually focuses. The EUV is radiated from this high-temperature and high-density xenon plasma. In DPF, there is less erosion of the electrode than other type of discharge load due to the short duration of expose electrodes to the plasma by moving the plasma. And the timing of focusing can be controlled by the electrode configuration. Materials of the anode, the cathode and the insulator are stainless steel, copper and alumina respectively. The xenon gas is injected center of the anode and the helium is injected from the other port.

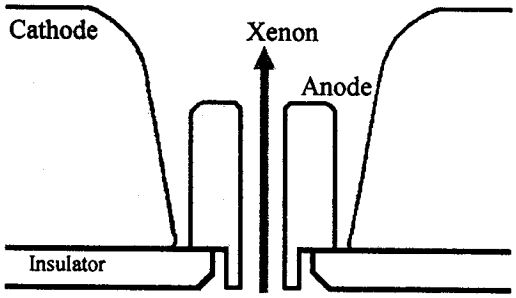

Figure 2. Plasma focus diode employed in the form of load.

III. Experimental result

Discharge tests have been carried out by using a high-current pulsed power generator. The visible-light photographs were taken by a high-speed camera. Table 1 shows the experimental conditions.

Table 1. Experimental conditions

Anode length	10 mm
Anode outer diameter	10 mm
Cathode inner diameter	13 mm
Anode material	Stainless steel
Cathode material	Copper
Insulator material	Alumina
C2 voltage	4.2 kV
Stored energy	10J
Repetition frequency	200 Hz
Gas flow rate	Xe, He 50 sccm
Exposure time	20 ns
Interval time	40 ns
Capturing duration	1st and 900th discharge
Pressure in chamber	40, 60, 80 Pa

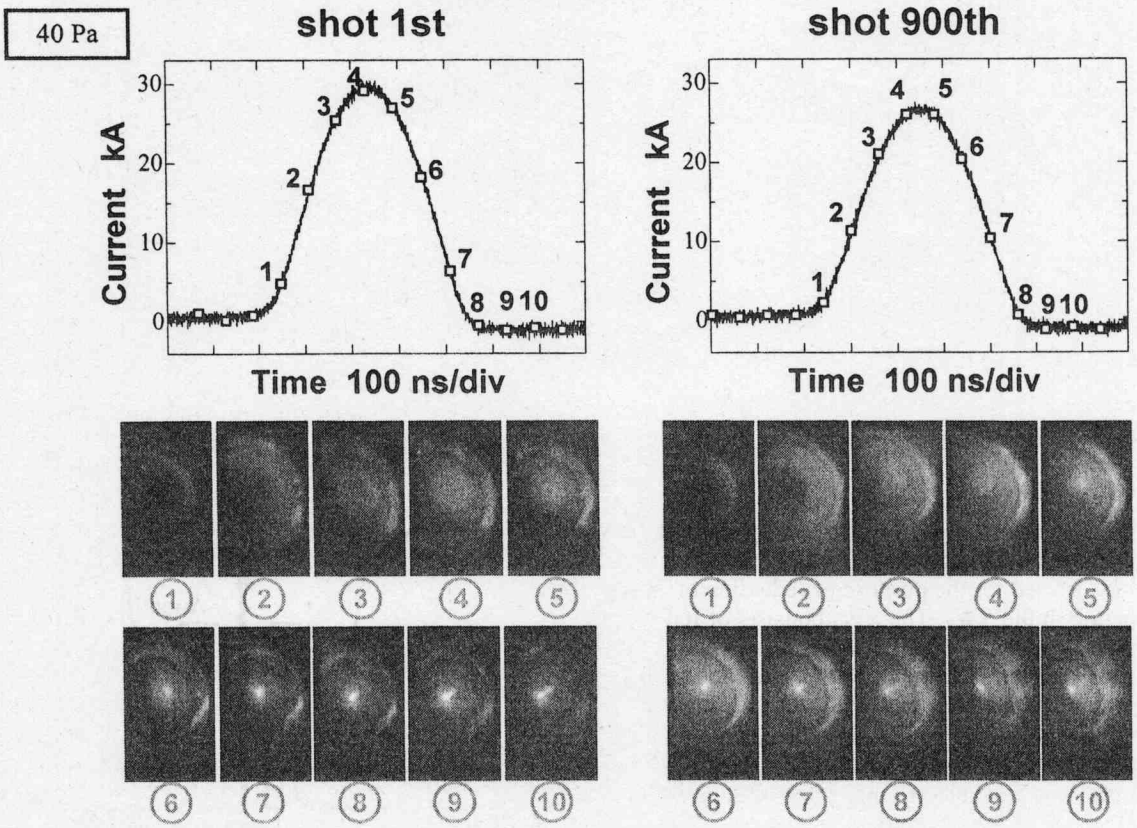

Figure 3. Current waveforms and photographs of electrodes during the discharge with 40 Pa.

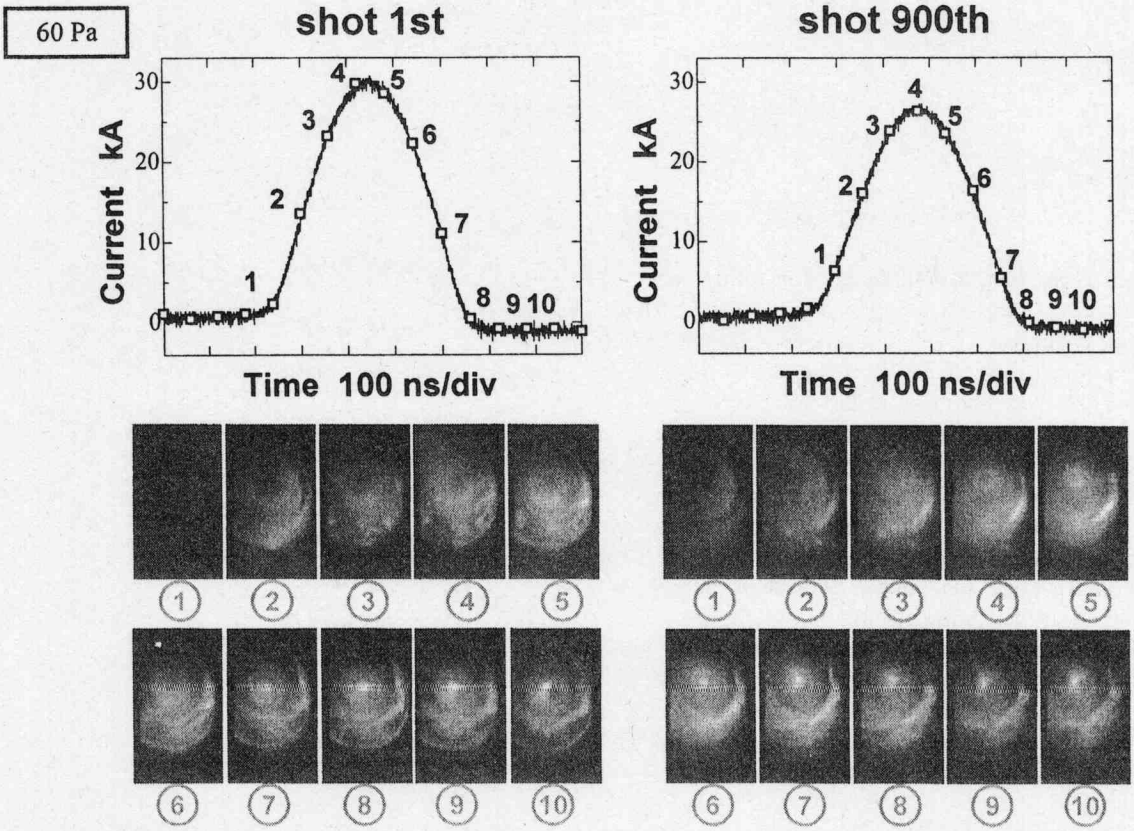

Figure 4. Current waveforms and photographs of electrodes during the discharge with 60 Pa.

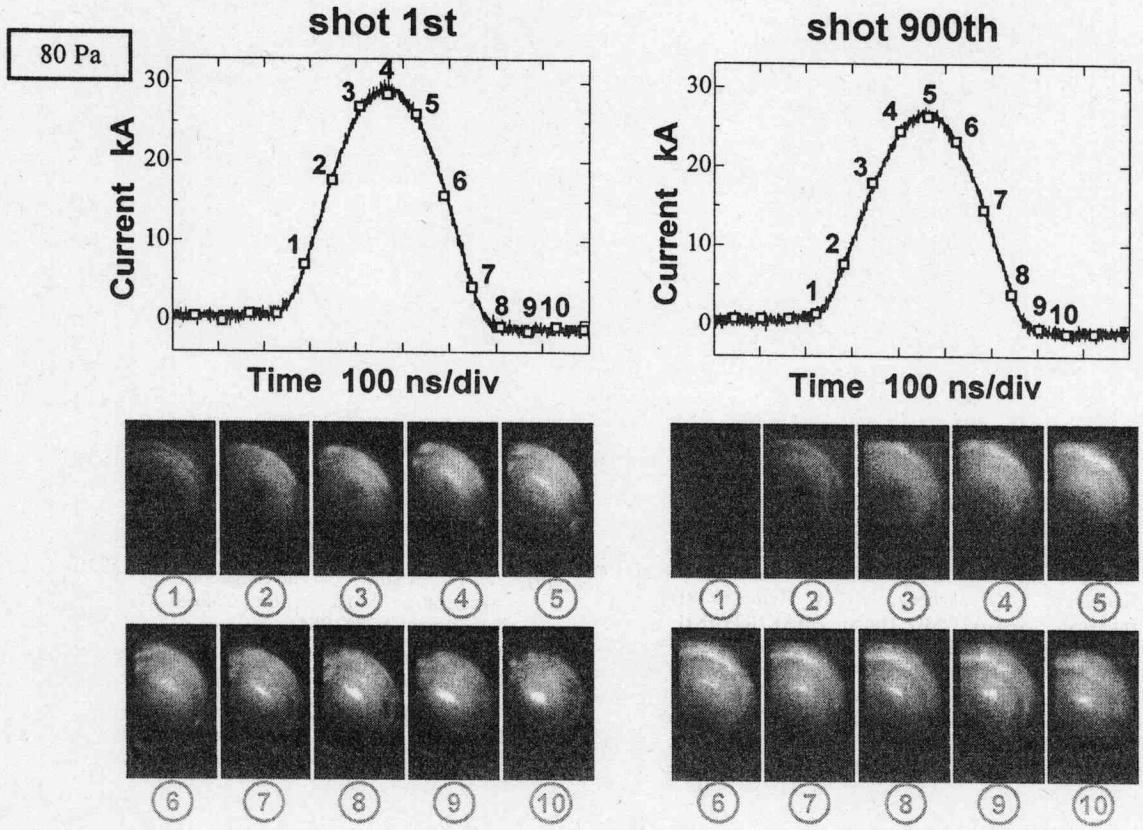

Figure 5. Current waveforms and photographs of electrodes during the discharge with 80 Pa.

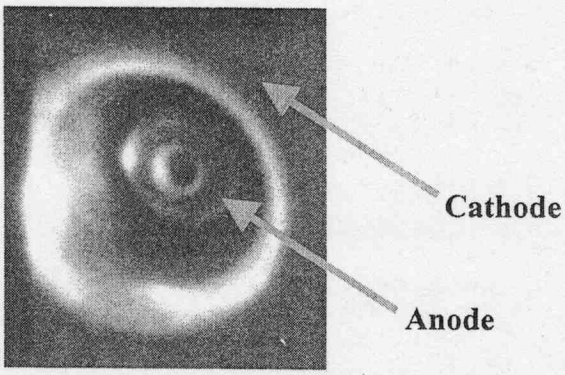

Figure 6. Picture of electrodes in light using a flash lamp

These photographs of electrodes taken with high-speed camera and the discharge current waveforms are shown in Figs. 3~5. In addition, Fig.6 is a picture of electrodes in light using a flash lamp. In Figs.3~5, the numbers of the photographs and the waveform relate to each other in terms of time. An emission of visible light can be seen between electrodes as discharge starting, and can be confirmed generating of plasma in the all photographs. It appears that the discharge is not arising at creepage surface of insulator but the vicinity of tip of the anode. However, the plasma moves to the center of tip of the anode with time, and focuses at a point.

And then the plasma is gradually attenuating. In addition, the timing of focusing with 60 Pa is later than 40 Pa, and the focusing is not arising with 80 Pa. This is attributed to the fact that the plasma couldn't focus during the passage of a current because the mass of plasma increased with the rising of pressure.

There is a little difference between peak values of current waveform when one compares the 1st and 900th discharge in the each photograph, but the timing of focusing is about the same time. Because the repetition frequency is 200 Hz, or the time cycle is 5ms, so previous discharge didn't influence the next discharge in the 900th discharge.

IV. Conclusions

Discharge tests using the high-current pulsed power generator have been carried out. The high-speed camera took the visible-light photographs. It was confirmed that the plasma has focused at the tip of the anode for gas pressure of 40 and 60 Pa. And the timing of focusing with 60 Pa was later than that of 40 Pa. The focusing was not confirmed with 80 Pa. This is attributed to the fact that the mass of plasma increased with the rising of pressure, timing of focus delayed. So plasma couldn't focus during the passage

of a current. In addition, it appears that the discharge is not arising at creepage surface of insulator but the vicinity of tip of the anode.

When one compares the 1st and 900th discharge, the timing of focusing is about the same time. Because the repetition frequency is 200 Hz, or the time cycle is 5ms, so previous discharge didn't influence the next discharge in the 900th discharge.

REFERENCES

[1] Katsuhiko Murakami, Tetsuya Oshino, Hiroo Kinoshita, Takeo Watanabe, Masato Niibe, Masaaki Ito, Hiroaki Oizumi, Hiromasa Yamanashi : "Ring-Field Extreme Ultraviolet Exposure System Using Aspherical Mirrors", Jpn. J.Appl.Phys., Vol.37, pp.6750-6755 (1998)

[2] NISHIMURA Hiroaki, SHIGEMORI Keisuke, NAKAI Mitsuo, FUJIOKA Shinsuke, SHIMADA Yoshinori, HASHIMOTO Kazuhisa, YAMAURA Michiteru, UCHIDA Shigeaki, MATSUI Ryoji, HIBINO Takahiro, OKUNO Tomoharu, TAO Yezheng, NAGAI Keiji, NORIMATSU Takayoshi, NAGATOMO Hideo, ZHAKHOVSKII Vasilli, FURUKAWA Hiroyuki, SUNAHARA Atsushi, KAWAMURA Tohru, NISHIKAWA Takeshi, MURAKAMI Masakatsu, NISHIHARA Katsunobu, MIYANAGA Noriaki, NAKATSUKA Masahiro and IZAWA Yasukazu : "Characterization of Extreme UV Radiation from Laser Produced Spherical Tin Plasmas for Use in Lithography", J. Plasma Fusion Res. Vol.80, No.4, p.325-330 (2004)

[3] Richard H. Moyer, Harry Shields, Armondo Martos, Steven W. Fornaca, Randall J. St. Pierre, Michael B. Peach : "Laser-Produce Plasma (LPP) Scale-up and Commercailization", Proc. of SPIE, vol.4343, p.249 (2001)

[4] I.V. Fomenkov, N. Böwering, C. L. Retting, S.T. Melnychuk, I. R. Oliver, J. R. Hoffman, O. V. Khodykin, R. M. Ness and W. N. Partlo : "EUV discharge light source based on a dense plasma focus operated with positive and negative polarity", J. Phys. D: Appl. Phys., 37, p.3266-3276 (2004).

[5] N. Oshima, Y. Kubota, T. Yokoo, K. Shimada, A. Tokuchi, W. Jiang and K. Yatsui : "Pulsed High-Current Generator for EUV Source Development", IEEJ Trans. FM, Vol.125, No.1, p.25 (2005)

[6] W. H. Bennett, " Magnetically Self-Focusing Streams " : Phys. Rev., Vol.45, 890 (1934)

[7] W. S. Meliville : "The Use of Saturable Reactors as Discharge Devices for Pulse Generators", Proc. of IEE, 98, p.185-207 (1951)

[8] K. Kurihara, S. Kobayashi, I. Satoh, K. Shibata, M. Shigeta, K. Masugata and K. Yatsui : "Magnetic pulse compressor using saturable transformer to excite excimer laser", Rev. Sci. Instrum. Vol. 63, No. 4, pp. 2138-2140(1992)

[9] J. W. Mather , "Investigation of the High-Energy Acceleration Mode in the Coaxial Gun", Phys. Fluids, Supplement, S28 (1964)

[10] J. W. Mather, "Formation of a High-Density Deuterium Plasma Focus", Phys. Fluids, Vol.8, No.2 (Feb. 1965)

[11] Yasuo Kato, Isao Ochiai, Yosio Watanabe, and Seiichi Murayama : "Plasma focus x-ray source for lithography", J. Vac. Sci. Technol. B6(1), Jan/Feb, p.195-198 (1988)

High-Energy-Density Physics Researches based on Pulse Power Technology

Kazuhiko Horioka, Mitsuo Nakajima, Tohru Kawamura, Toru Sasaki, Kotaro Kondo, Yuuri Yano

Department of Energy Sciences, Interdisciplinary Graduate School of Science and Engineering, Tokyo Institute of Technology, Nagatsuta 4259, Midori-ku Yokohama Japan 226-8502

Plasmas driven by pulse power devices are of interest, concerning the researches on high-energy-density (HED) physics. Dense plasmas are produced using pulse power driven exploding discharges in water. Experimental results show that the wire plasma is tamped and stabilized by the surrounding water and it evolves through a strongly coupled plasma state. A shock-wave-heated, high temperature plasma is produced in a compact pulse power device. Experimental results show that strong shock waves can be produced in the device. In particular, at low initial pressure condition, the shock Mach number reaches 250 and this indicates that the shock heated region is dominated by radiation processes.

Key-words; pulse power, high energy density, warm dense matter, shock wave, equation of state, electrical conductivity, radiation transport

1 INTRODUCTION

Properties of dense and/or high temperature plasma are of interests concerning the high energy density (HED) physics. We are working on two topics. The first one is a warm dense plasma made by exploding wire discharges in water and the second is a high temperature plasma induced by a strong shock wave. Both of those plasmas are driven by compact pulse power devices with laboratory scale.

A warm dense (WD) state is produced by a wire explosion in water using a small, cylindrically arranged, pulse power generator. Electrical conductivities are directly estimated from the voltage-current characteristics of the wire explosion. Compared with previous research [1], we intended to make a semi-empirical approach to the exploding wire plasma; we discuss the scaling of equation of state (EOS) and transport coefficients from comparisons of numerical calculations and experimental observations of hydrodynamic behaviors, which cylindrically evolve high density plasma. As the structure and the hydrodynamics of HED plasma are dominated by the EOS and the transport coefficient of them, we can discuss those values from the comparison of experiment observation and numerical simulation. In particular, we propose to use shock wave trajectories in water as a fitting parameter of the hydrodynamic behaviors.

The structure of strong shock waves in high-Z gas is expected to be completely different from that of conventional hydrodynamic shock waves, because relaxation processes and/or radiative

processes in the shock heated region affect the structure of shock wave itself [2].

For the discussion of such a complicated hydrodynamics, the geometry should be as simple as possible. The exploding plasma in water is tamped and stabilized by the surrounding water and it makes cylindrically expanding plasma. To make a well-defined, steady state, high temperature plasma, we designed a compact pulse power device, which has a pair of tapered electrodes and a cylindrical guiding tube. This configuration enables us to use one-dimensional assumption.

2 WIRE EXPLOSION IN WATER FOR WARM DENSE MATTER PHYSICS

In order to make warm dense plasmas, thin (50 μ m-100 μ m dia.) wires are exploded in a water-filled chamber. In the experiments, wire materials, their radius and the charge voltage are changed to make the plasma over a wide range of parameters.

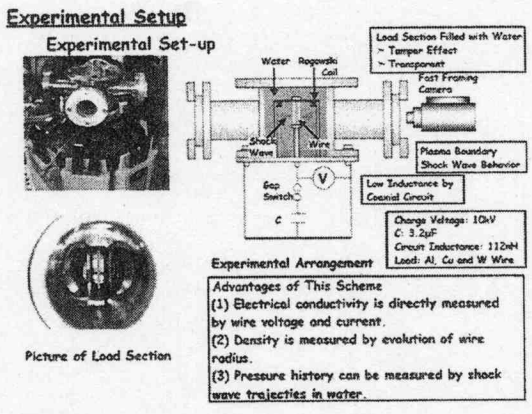

Fig.1 Experimental set-up and photograph of the device for exploding wire experiments

2-1 Experimental Arrangement

Figure 1 shows a schematic diagram of the exploding wire discharges in water [3,4]. A capacitor bank C, consists of cylindrically arranged 8x0.4μF low inductance capacitors. The stray inductance Ls of the device was estimated to be Ls=105μH and it drove the wire explosion in water with time scale of μsec. The current and the voltage are measured with a Rogowski coil and a resistive voltage divider. The evolutions of wire/plasma boundary and the shock wave are measured with fast streak/framing camera. From these measurements, we can directly estimate the electrical conductivities of exploding plasma.

2-2 Electrical Conductivity

Using the framing camera, the radius and the particle density was estimated to be typically $10^{21}cm^{-3}$ at 2μsec from start of the discharge. Figure 2 shows the evolution of electrical conductivities of aluminum (Al), copper (Cu), and tungsten (W) wires.

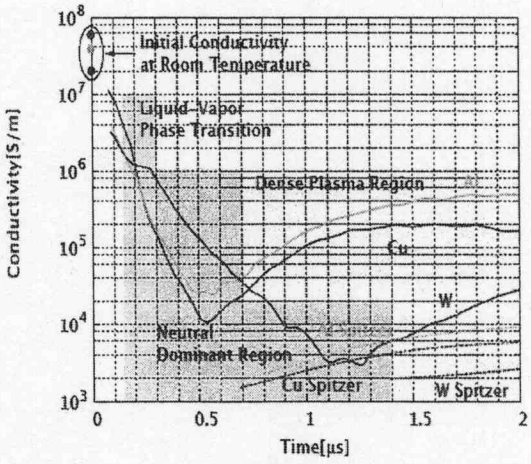

Fig.2 Evolution of conductivities for Al, Cu, and W wire explosion in water

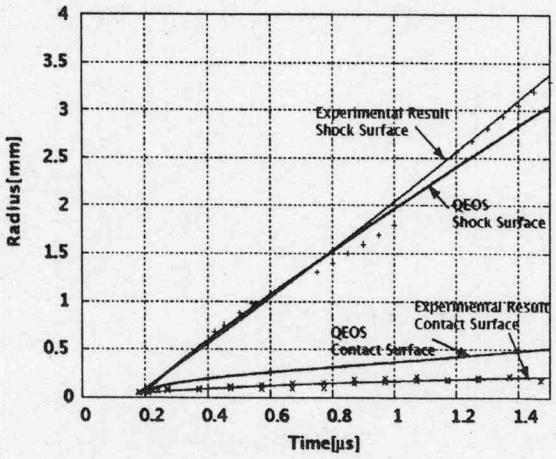

Fig.3 Experimental and numerical evolutions of wire/plasma boundary and shock surface in water

The dotted lines in the figure show theoretical values for conductivities based on a modified Sptzer's model, and as can be seen, the experimental observations of the conductivities are more that 10times of the theoretical values.

We calculate the hydrodynamic behavior of the exploding plasma and the shock wave propagation in water using a 1D magneto-hydrodynamic simulation. To make the calculation, we need EOS models and the transport coefficients. Figure 3 shows the comparison of numerical and experimental evolution of the shock wave and the plasma boundary for Al wire explosion. Experimentally obtained conductivities and Q-EOS model [5] are used in this calculation.

As the hydrodynamics are strongly dependent on the EOS model, we can evaluate its applicability in the parameter region of WD plasma, by using it as a fitting parameter. Especially the numerical shock trace is more strongly affected by that of plasma boundary ;i.e., the EOS model. Figure 4 shows an illustration of the shock trajectory induced by the plasma evolution. The exploding wire/plasma induces a cylindrically developing shock wave, as a piston, through "characteristics" in water. As illustrated in the figure, the shock trace expands the behavior of the plasma motion, both in space and time. This indicates that the shock wave trajectory in water is informative for estimation of the plasma pressure, i.e., for the EOS modeling.

3 FORMATION OF STRONG SHOCK WAVES WITH PULSE POWER DEVICE

Another compact pulse power device is constructed for generation of quasi-steady, one-dimensional, strong shock waves. The cross-section of the discharge region is gradually decreased with a pair of tapered electrodes. The shock wave induced by an electro-magnetically driven current sheet is guided through the tapered section to the top of electrodes. At the end of the electrodes, an acrylic guiding tube is attached to make one dimensional flow [6].

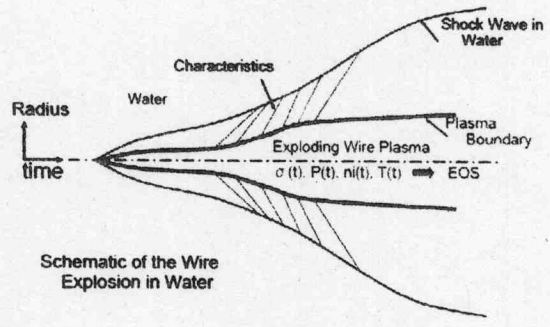

Fig.4 Schematic illustration of exploding wire discharges in water

3-1 Experimental Arrangement

The experimental set up of the pulse power device is shown in Fig.5. The acrylic guiding tube is advantageous to observe the shock wave propagation. The shock speed is measured by a fast framing/streak camera through the acrylic guiding tube. To drive the electro-magnetic pulse, twelve plastic capacitors are arranged in a cylindrical geometry. They are normally charged to 20kV and switched by a pressurized gap switch, which drove 160kA in the discharge chamber.

3-2 Experimental Results

Figure 6 shows typical experimental results. The solid line in the figure shows a criterion of radiative shock based on a steady state one dimensional flow [7]. As shown, the front velocity increased with the decrease of initial filling pressure of Xe. When the discharge chamber is filled with low pressure Xe gas, the shock Mach number M reached M=250, and, as shown in the figure, this value adequately exceeds the criterion for radiative shock waves.

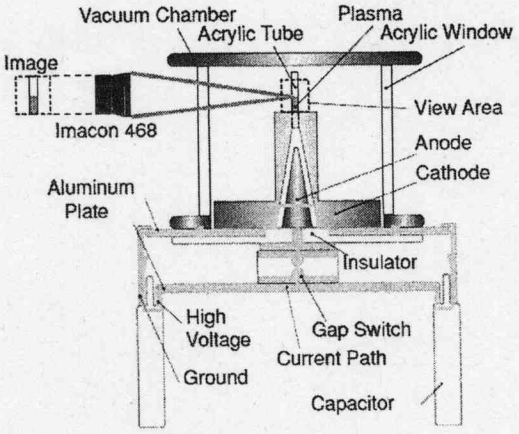

Fig.5 Experimental arrangement for shock heated high temperature hydrodynamics

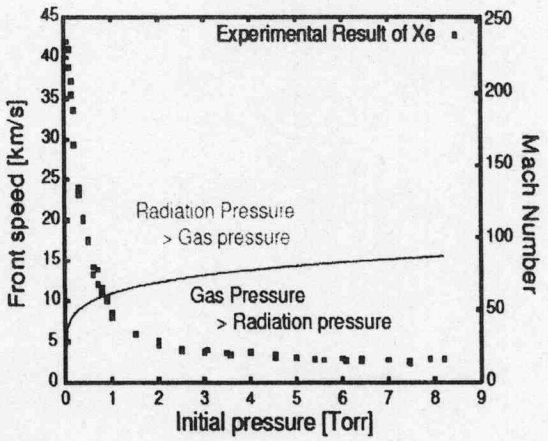

Fig.6 Observed front speed and shock Mach number versus initial filling pressure of Xe

A streak picture is shown in Fig.7, together with a typical numerical calculation of the electromagnetically driven flow of Xe. The upper part is the streak image of the flow and the lower shows a schematic of typical profiles of the relaxation region. In the calculation electron-ion and ionization relaxation process of the Xe plasma is estimated under an assumption of one-dimensional shock heated, steady flow.

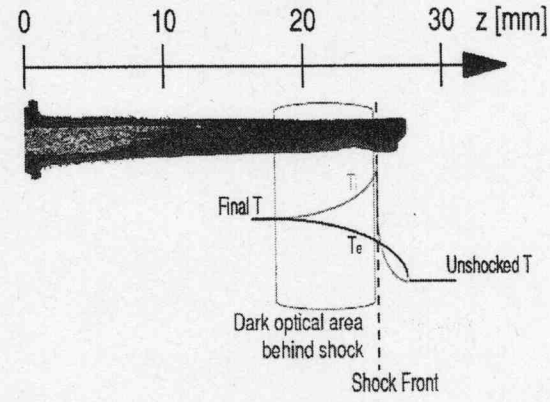

Fig.7 Streak image and typical temperature profiles of shock heated Xe plasma

When the front speed exceeds the criterion derived from the one dimensional simplified analysis, the streak image had an interesting structure [6]. The results indicate that structure of the shock heated region is dominated by the ionization relaxation in Xe plasma and its initial condition should be provided by a radiative process from the heated region. This means from the comparison of experimental observation and numerical calculation, we can quantitatively discuss the effect of radiation transport on the hydrodynamics of heated gas with a strong shock wave.

4 SUMMARY

Plasmas produced by compact pulse power devices are proposed for HED and/or WDM physics. Results show that plasmas made by wire explosion in water can be appropriate sources for scaling of the equation of state and transport coefficients in a wide range of parameters of warm-dense materials. Coupling parameter of the plasma is estimated to be at least 2, up-to discharge time of 2 μ sec. On the other hand, shock wave heated plasmas produced by pulse powered electro-magnetic force in a pair of conical electrodes, are demonstrated to be a suitable one-dimensional test sample for high temperature hydrodynamics involving ionization relaxation and a radiative energy transfer.

These devices can cover a dense moderate temperature region and a high temperature low density region in the density-temperature diagram for HED physics [8]. Advantages of these approaches are compactness, capability of making larger spatial and temporal scale plasmas, and also providing a well-defined condition, compared with those of high power laser methods.

Acknowledgement

This work was partially supported by the Ministry of Education, Culture, Sports, Science and Technology, Grant-in-aid for Scientific Research.

REFERENCES

[1] A.W.DeSilva and J.D.Katsourros, *Phys. Rev.*, **E-57**, 5945 (1998)

[2] Y.B.Zel'dovich and Y.P.Raizer, *Physics of Shock Waves and High Temperature Hydrodynamic Phenomena*, Academic, New York, (1967)

[3] K.Horioka, M.Nakajika, T.Mizoguchi, T.Sasaki, *Proc. 15th High Power Particle Beams*, St-Petersberg, 7053 (2004)

[4] SASAKI, T., NAKAJIMA, M., KAWAMURA,T., HORIOKA,K., *J. Plasma Fusion Res.*, **Vol.81**, No.12, pp.965-966 (2005)

[5] R.M.More, *Phys. Fluids.*, **Vol.31**, 3059 (1988)

[6] Kotaro Kondo, Mitsuo Nakajima, Tohru Kawamura, Kazuhiko Horioka, *Review of Scientific Instruments*, **Vol.77**, 036104 (2006)

[7] S.Bouquet, R.Teussier and J.P.Chieze, *Astrophys. J., Suppl. Ser.*, **Vol.127**, p.245 (2000)

[8] *Frontiers in High Energy Density Physics-The X-Games of Contemporary Science*, Edited by R.Davidson et.al., National Academies Press, (2003)

APPLICATION OF PULSED STREAMER-LIKE DISCHARGE FOR CYANOBACTERIA BLOOMS TREATMENT

Zi Li, Douyan Wang, Takao Namihira, Sunao Katsuki and Hidenori Akiyama

Department of Electrical and Computer Engineering, Kumamoto University 2-39-1 Kurokami, Kumamoto 860-8555, Japan.

ABSTRACT

Recently, cyanobacteria blooms (or water blooms) occurred on the surface of water bodies frequently and extensively due to the eutrophia of the water. That has been posed a more and more serious environmental problem worldwide. In this work, we try to use pulsed power technology to realize water blooms treatment. A stainless needle with 30 μ m in diameter was employed as a point discharge electrode, 15cm apart from the cylindraceous cathode, and applying a 2 μ s, 160kV pulse. A pulsed streamer-like discharge in water was obtained in the water filled with cyanobacteria cells (named as sample water in this paper). From the experimental result, it can be found that the discharge collapsed the intracellular structure - gas vesicles and the colonies of the cells sank to the bottom and didn't float up during 15 days after the discharge treatment.

I. INTRODUCTION

Cyanobacteria (often referred to as blue-green algae) are members of a group know as eubacteria or true bacteria [1]. They are a frequent component of many freshwater and marine ecosystems. Under certain conditions, especially where waters are rich in nutrients and exposed to sunlight, cyanobacteria may multiply to high densities - a condition referred to as a water bloom [6]. Large blooms of cyanobacteria can clog intake pipes and filter lines, and are aesthetically unappealing. When a bloom dies in a pond or shallow lake, severe oxygen depletion can produce objectionable odors and even cause fish kills. Some cyanobacteria produce substances that are extremely toxic, and are capable of causing serious illness or even death if consumed [1]. Recently, cyanobacteria outgrow rapidly and easy to form blooms in lakes and agricultural ponds because of the eutrophication. Therefore, the blooms of cyanobacteria have been posed a serious environmental problem all over the world. In this paper, we present of result of the effects of streamer-like discharge in water for the treatment of cyanobacteria blooms.

A Blumlein-type pulsed forming network (B-PFN) was employed to provide a 2 μ s, 160kV pulsed voltage to a point-to-plate electrode geometry and generate a tremendously high electric field and formed streamer-like discharge in sample water which was collected from Higawa Dam in Kumamoto, Japan.

II. EXPERIMENTAL APPARATUSES

A. Sample water from Higawa Dam

The sample used in the experiment was collected from Higawa Dam in Kumamoto, Japan. It was confirmed that the major genus was *M. aeruginosa*. *M. aeruginosa* with 3.2-6.6 μm in diameter are a typical genus of toxic cyanobacteria 4). It can be observed from Fig. 1 (a) that *M. aeruginosa* in the sample water appeared black in color. It can be also observed that hundreds or thousands of *M. aeruginosa* cells gathered together and formed the colonies and the colonies appeared to be small-green particles and floated in the water. Fig. 1 (b) shows a single cell of *M. aeruginosa* with 1000 times of magnification. It can be seen that the mucilaginous sheath (MS) surrounded cell of *M. aeruginosa*, and the gas vesicles (GVs) showed blackish appearance due to the refraction of background light. GVs are the special intracellular structure of the bloom-forming cyanobacteria genus [2]. GVs filled with gas. Therefore, cyanobacteria cells can float toward water surface to position in optimal sun light condition for growth [3]. The electrical conductivity of the sample water was 11.6 mS/m.

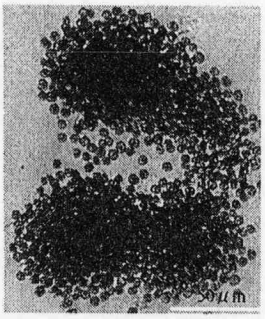

(a)

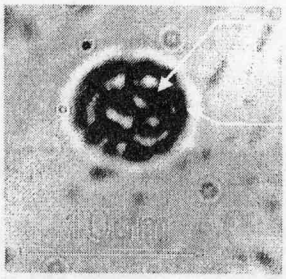

(b)

Fig. 1 *M. aeruginosa* sampled of Hikawa dam. 1: mucilaginous sheath (MS), 2: gas vesicles (GVs).

B. Pulsed streamer-like discharge system

Fig. 2 shows the schematic diagram of the pulsed power generator used in this work. The generator consisted of a positive dc source (E, HDV-50K3US, Pulse Electronic Engineering Co., Japan), the Blumlein type pulse forming network (B-PFN) and a pulse transformer (PT). A triggered spark gap switch (SGS) was used as a closing switch of B-PFN. B-PFN had 15 stages of LC ladder which were composed with 20 nF of capacitor and 0.2 μH of inductor. The characteristic impedance ($2\sqrt{L/C}$) and the pulse width ($2N\sqrt{LC}$) of B-PFN, calculated from capacitance (C) and inductance (L) of LC ladder, and number (N) of LC ladder stage, were approximately 6 Ω and 1.9 μs, respectively. The FINEMET™ (FT-3H, Hitachi Metals, Japan) was utilized as the core material of PT. PT had 5 of the winding ratio (windings: secondary windings = 1: 5). Therefore, the total characteristic impedance of the generator was computed at 150 Ω (6 Ω×5^2).

Fig. 3 shows the configuration of the discharge chamber used in this experiment. The needle to cylinder electrode was utilized as the discharge chamber. The needle electrode with 30 μm in tip curvature was put concentrically into the cylinder electrode with 300 mm in inner diameter and 180 mm in length. To enhance the electric field at the tip of needle electrode, the needle was covered with polyethylene insulator except the part of tip. In the experiment, the discharge chamber was filled with the sample water from Higawa Dam. The output from the pulsed power generator was connected to the needle electrode and the cylinder electrode of the discharge chamber was grounded. The charging voltage into B-PFN was fixed at +25 kV. In this case, the positive polarity of pulsed voltage was applied to the needle electrode. For the utilization of the maximum flux swing of PT core, the reset current of 2 A was flown near the PT core.

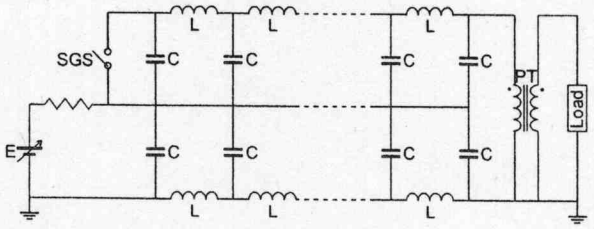

Fig. 2 Schematic diagram of pulsed power generator.

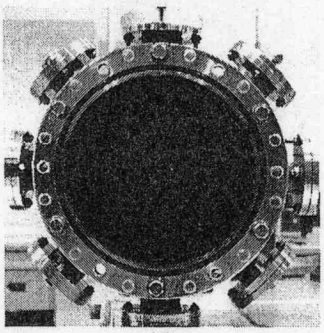

(a)

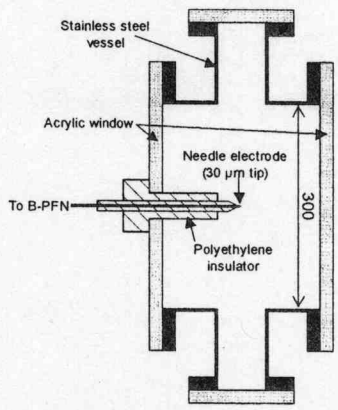

(b)

Fig. 3 (a) Photo of discharge chamber. (b) cross section of the chamber

III. EXPERIMENTAL RESULTS AND DISSUSIONS

A. Discharge treatment of M. aeruginosa

Fig. 4 (a) shows the photograph of the discharge

chamber soon after it was filled with the sample water of Hikawa dam. It can be seen that the colonies of *M. aeruginosa* were suspending in the entire discharge chamber. Fig. 5 shows the waveforms of applied voltage to and discharge current with through the discharge chamber with 160 kV and 500A of the peak value respectively. The input energy into the discharge chamber was calculated at 83 J/pulse. Fig. 6 shows the appearance of single discharge in the tap water with conductivity of 11.6mS/m. It was confirmed that the streamer-like discharges spread from the positive needle electrode toward the ground cylinder electrode and did not shift to an arc discharge. The diameter of discharge area was about 100 mm. Fig. 4 (b) shows the appearance of single discharge of the chamber after about 2 hours.

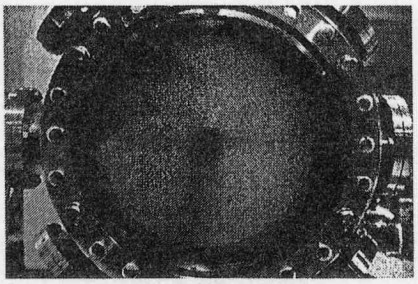

(a)

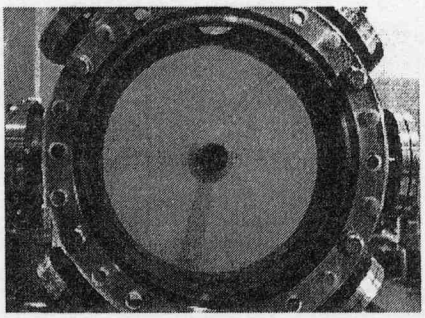

(b)

Fig. 4 Discharge chamber just after sample water injection (a) and 2 hours later after discharge (b)

***B. Diagnosis of* M. aeruginosa**

In order to diagnose *M. aeruginosa* conditions after applying discharge, a part of the discharge-treated *M. aeruginosa* was collected from the bottom of the discharge chamber and carried out the microscopical observation.

Fig. 7 shows the bright-vision photomicrographs (a: ×400 magnification, b: ×1000 magnification) of *M. aeruginosa* cells after single discharge treatment. As the result of the comparison of Fig. 1 with Fig. 7, it can be seen that the GVs in the cells of *M. aeruginosa* disappeared.

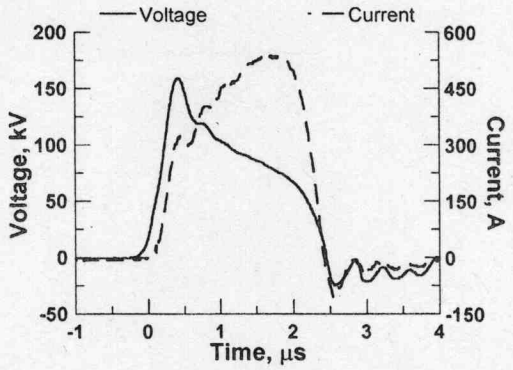

Fig. 5 Applied voltage to and discharge current through chamber

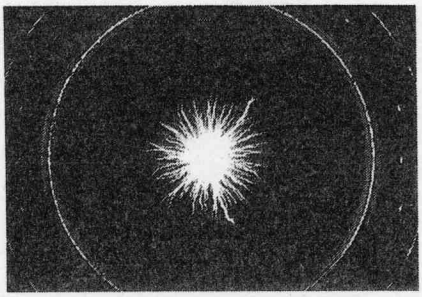

Fig. 6 Discharge appearance in chamber

It can be said that the GVs were collapsed by the pulsed discharge treatment. Furthermore, the discharge-treated *M. aeruginosa* were kept in a test tube for 15 days under 24℃ 12 hours sunlight. Fig. 7 shows the time dependence of the appearance of the test tube with the discharge-treated *M. aeruginosa*. It was observed that the discharge-treated *M. aeruginosa* didn't float up to the surface of water and changed color from green to yellow. Finally, they disappeared after 15 days from the discharge treatment. There is a possibility that the treated *M. aeruginosa* cells were catabolized by other bacteria or plankton in the sample water.

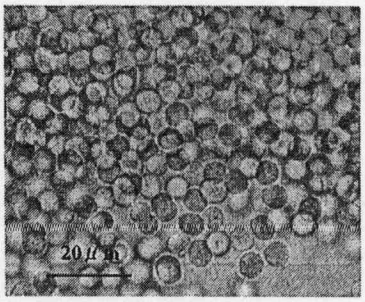

(a)

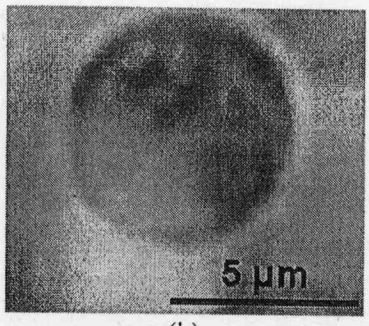

(b)

Fig. 7 *M. aeruginosa* after discharge treatment. (a) the colony, (b) single cell.

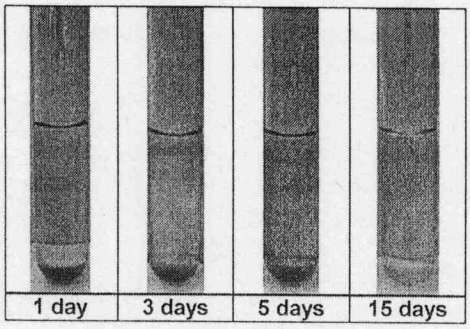

Fig. 8 Time dependence of discharge-treated *M. aeruginosa*

C. Discussion

It is well known that the pulsed streamer-like discharge in water can cause four physical phenomena, such as the intense electric field near the discharge electrode, the radical formation in the plasma, the ultraviolet irradiation and the shockwave generation [4]. What is the most impact factor in the *M. aeruginosa* treatment experiment should be considered. In this experiment, *M. aeruginosa* cells in the discharge chamber were treated by single discharge. It is obvious from Fig. 6 that the discharge didn't spread to the entire space of the discharge chamber. The radical formation has no effect at the outside of discharge region. And the use of UV radiation has been described for obtaining axenic cultures of cyanobacteria. [7]. Therefore, ultraviolet irradiation doesn't seem to play a role in influence on the cyanobacteria cells. As conclusion, the shockwave and pulsed electric field due to the pulsed streamer-like discharge in water are the most effective factors for *M. aeruginosa* treatment.

IV. CONCLUSIONS

Pulsed streamer-like discharge in water were used to treat *M. aeruginosa* cells from the Higawa Dam, Kumamoto, Japan. The following conclusions have been deduced:

1) After single discharge treatment, *M. aeruginosa* sank to the bottom and didn't float up since the GVs of the cells were collapsed by discharge;
2) Discharge-treated *M. aeruginosa* were gradually disappeared during 15 days;
3) There is a possibility that the pulsed streamer-like discharge will become one of effective options to treat cyanobacteria blooms.

REFERENCES

1) N. Scott, "Algae, Cyanobacteria and Water Quality", Agriculture and Agri-Food Canada, Water Quality Matters, 2002.
2) A. Howard, "Problem cyanobacteria blooms: explanation and simulation modeling", Transactions of the Institute of British Geographers, Vol.19, No. 2, pp.213-224, 1994.
3) A. Mlouka, K. Comte, A. Castets, C. Bouchier and N. Marsac, "The gas vesicle gene cluster from microcystis aeruginosa and DNA rearrangements that lead to loss of cell buoyancy", Journal of Bacteriology, Vol.186, No.8, pp.2355-2365, 2004.
4) H. Akiyama, "Streamer discharge in liquids and their applications", IEEE Transactions on Dielectrics and Electrical Insulation, Vol.7, No.5, pp.646-653, 2000.
5) A. Abou-Ghazala. S. Katsuki, Member, IEEE, Karl H. Schoenbach, Fellow, IEEE, F. C. Dobbs, and K. R. Moreira, "Bacterial Decontamination of Water by Means of Pulsed-Corona Discharges", IEEE Trans. Plasma Sci. 30(4):1449-1453, 2002.
6) Ingrid Chorus and Jamie Bartram, "Toxic Cyanobacteria in Water: A guide to their public health consequences, monitoring and management" published on behalf of WHO by:F & FN Spon,11 New Fetter Lane, London EC4) 4EE
7) R. D. HAMILTON and A. F. CARLUCCI, Nature (London) 211: 483-484 (1966).

EMTP Simulation for the Design of the Pulsed Power System using MPC and BPFN

J. Choi, T. Yamaguchi, K. Yamamoto, T. Namihira, T. Sakugawa, S. Katsuki, IEEE, and H. Akiyama

Kumamoto University, 2-40-1 Kurokami, Kumamoto 860-8555, Japan

ABSTRACT

In this paper, the authors have developed an all solid state pulsed power generator that consists of magnetic pulse compressor (MPC) and Blumlein-type pulse forming network (BPFN), which is operated with high repetition rate, long lifetime and high reliability for practical industrial applications such as laser exciters, decomposition of harmful gases, removal of volatile toxic compounds, water discharges and so on. And they have given a detailed explanation about the simulation methodology using Electromagnetic transient program (EMTP) in order to give a guidance for more efficient design of the pulsed power generator with MPC and BPFN. It was found that the simulation results and the experimental ones with manufactured MPC and BPFN showed a good consistency. Finally, large volume of streamer discharges was generated in water by the developed system.

I. INTRODUCTION

Since W. Melville described a magnetic pulse compressor (MPC) by using the nonlinear permeability of ferromagnetic materials in 1951 [1] as a breakthrough for the high repetition rate pulsed power generators, researches on MPCs have focused on high power pulse generation such as radar modulation, nuclear particle acceleration and impulse testing for a long time.

Comparatively recent developments of ferromagnetic materials [2,3] and semiconductor switches with excellent characteristics have allowed the high repetitive operation of magnetic switches (MS) with very low loss, and have made it possible to use the repetitive pulsed power generated by an MPC on practical industrial applications such as laser exciters, decomposition of harmful gases, removal of volatile toxic compounds, water discharges and so on [4,5,6,7] due to its high repetition rate, high stability and long lifetime.

Meanwhile, there are numerous applications in both physics and electrical engineering for short (t_p < 10 μs) electrical pulses. These applications often require that the pulses have a good square shape, i.e. they have fast rise and fall times (t_r, $t_f \ll t_p$) [8]. Although there are many ways for generating such pulses, the pulse forming network (PFN) is one of the simplest techniques. It is possible to control the pulse width of the output pulse voltage by varying the number of the units of the inductor and the capacitor. The Blumlein-type pulse forming network (BPFN) is very popular due to the fact that the power supply used to charge the network may have the same output potential as the required pulse amplitude.

Although there has been much need for the design and analysis techniques of the high repetition rate pulsed power generator using MPC and BPFN, there has been few studies concerning the simulation methodology of the MPC [9] and the BPFN, probably due to difficulties in the design of the nonlinear permeability of ferromagnetic cores for the MS and the pulse transformer (PT).

In this paper, the authors have developed an all solid state pulsed power generator, which is operated with high repetition rate, long lifetime and high reliability for industrial applications and given a detailed explanation about the simulation methodology using Electromagnetic transient program (EMTP) in order to give a guidance for more efficient design of the pulsed power generator with MPC and BPFN. It was found that the simulation results and the experimental ones with manufactured MPC and BPFN showed a good consistency. Moreover, much contribution of the proposed methodology is expected to the design of the nonlinear devices in the pulsed power field as well.

II. FUNDAMENTAL THEORY

Figure 1 shows a typical MPC circuit [8]. MS_u and MS_s refer to the unsaturated and the saturated inductances, respectively. And, suppose that $C_1 = C_2 = C_3 = C$ and $MS_s \ll L_1 \ll MS_u$. Referring to Figure 1, on switch closure the capacitor C_1, initially charged to a potential V_0, is discharged through the inductor L_1 into capacitor C_2. As the potential on C_2 rises a point is reached at which the magnetic switch MS will saturate. C_2 then discharges rapidly into capacitor C_3.

Consider the charging of capacitor C_2 from the previous capacitor C_1 via the inductor L_1. The voltage $V_2(t)$ on C_2 will be given by

$$V_2(t) = V_0 \frac{C_1}{C_1 + C_2}(1 - \cos\omega t) = \frac{V_0}{2}(1 - \cos\omega t) \quad (1)$$

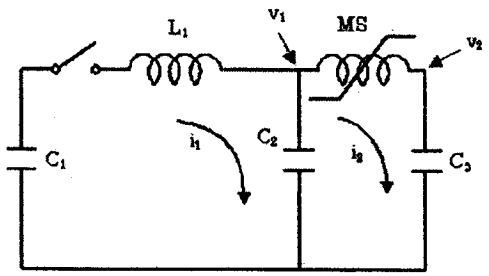

(a) Basic MPC circuit

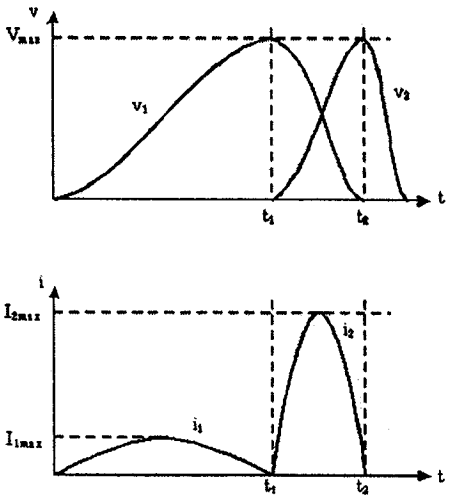

(b) voltage and current waveforms

Fig. 1. Operation of the basic magnetic pulse compressor.

where $\omega = \dfrac{1}{\sqrt{L_1 C_0}}$

And, the time t to charge C_2 is given by

$$t = \pi\sqrt{L_1 C_0} \qquad (2)$$

where $C_0 = \dfrac{C_1 C_2}{C_1 + C_2} = \dfrac{C}{2}$

As a result, the maximum voltage on C_3 is equal to the charging voltage V_0 on C_1, and the voltage amplification does not occur. The current amplification ratio η_c is given by

$$\eta_c = \frac{I_{2\max}}{I_{1\max}} = \frac{V_0\sqrt{\dfrac{C_0}{MS_s}}}{V_0\sqrt{\dfrac{C_0}{L_1}}} = \sqrt{\frac{L_1}{MS_s}} \qquad (3)$$

Figure 2 shows a typical Blumlein-type pulse forming network which consists of LC ladder networks. In the figure, the pulse transformer was attached to the network

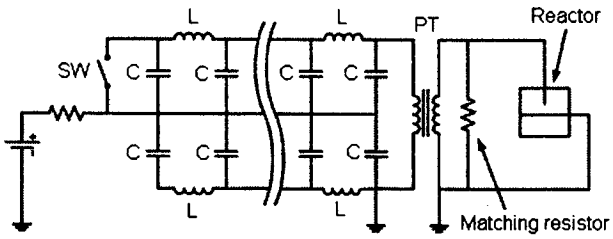

Fig. 2. Diagram of the Blumlein pulse forming network.

in order to obtain a higher output voltage. It is possible to control the pulse width of the output pulse voltage by varying the number of the units of the inductor and the capacitor in the BPFN. The pulse width τ is given by

$$\tau = 2N\sqrt{LC} \qquad (4)$$

where N refers to the number of units. And, the characteristic impedance of the BPFN is given by

$$Z = 2\sqrt{\frac{L}{C}} \qquad (5)$$

III. PULSED POWER SYSTEM COMPONENTS

The block diagram of the repetitive pulsed power system that we developed is shown in Figure 3. The developed system consists of MPC unit, BPFN unit and load unit.

A. MPC unit

The MPC consists of a charger, low inductance capacitors (C_0, C_1), saturable inductors (SI_0, SI_1), thyristor switch (Thy) and a pulse transformer (PT_1). The charger is high voltage power supply using resonant inverter (202A, LAMBDA EMI). An average capacitor charging rate is 2000 J/s(Joule per second). The capacitances of C_0 and C_1 are 6.6 μF and 200 nF, respectively. Fe-based nanocrystalline magnetic cores (FT-1H, Hitachi metals Ltd) were used as the magnetic switches (SI_0, SI_1). The thyristor is a high speed thyristor for pulsed power application (5STH20H4501,ABB). The magnetic assist by the saturable inductor (SI_0) follows the thyristor switching. Magnetic assist has the effect of reducing the switching loss of the thyristor [8]. The PT_1 has a function of step-up transformer. The voltage gain of the PT_1 is 6 (winding ratio, primary : secondary = 4 : 24). In the experiment, the applied voltage to and the discharge current through the needle to plane electrodes were measured using the voltage divider (EP-100K, Pulse Electronic Engineering Co., Japan) and the current monitor (Model 110A, Pearson Electronics, Japan), respectively. The Oscilloscope (HP54542A, Hewlett-Packard, USA) recorded the signal from the measurement devices.

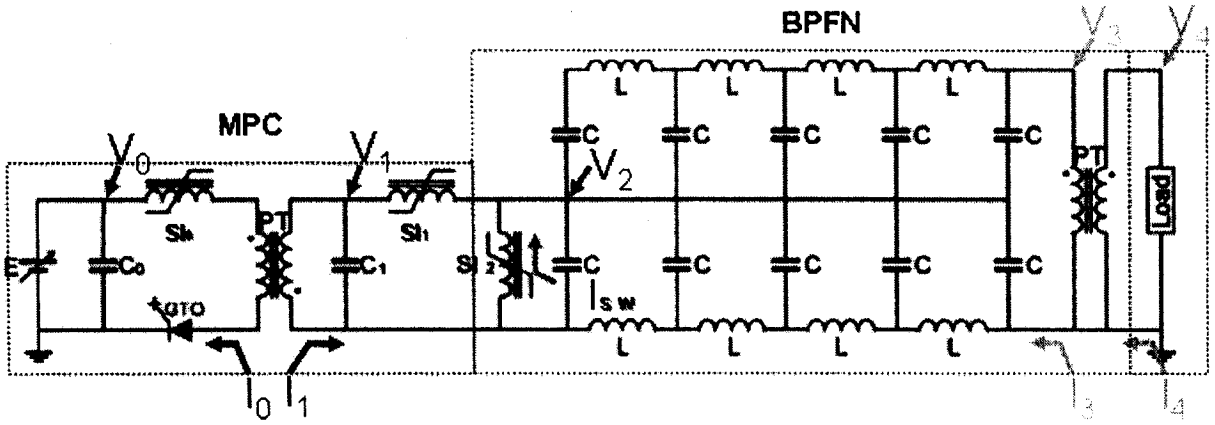

Fig. 3. Schematic diagram of the pulsed power system for water treatments.

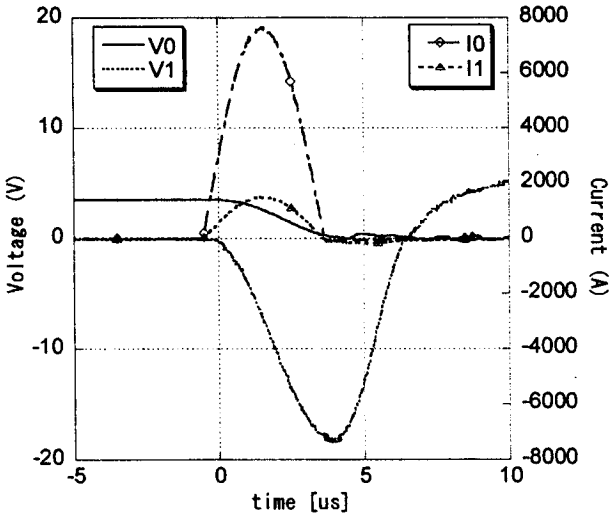

Fig. 4. Measured waveforms of V0, V1, I0 and I1.

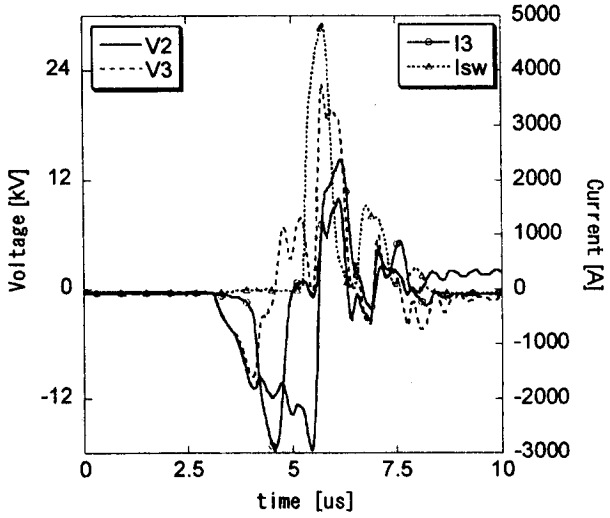

Fig. 5. Measured waveforms of V2, V3, I3 and I_{sw}.

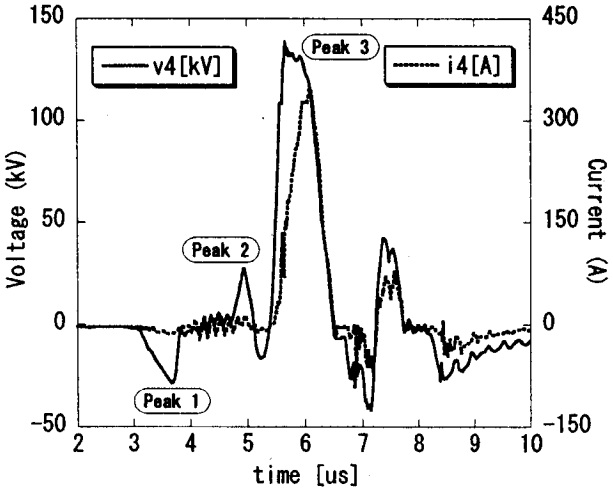

Fig. 6. Measured waveforms of V4 and I4.

The thyristor turns on after C_0 is fully charged up to 3.6kV by the charger, and then SI_0 saturates immediately after the assist time. The current I_0 with duration of 4.4 μs flows in the primary circuit of PT1. As a result, C_1 is charged to a high-voltage through the PT. In this time, SI_1 performs as a current blocking inductor for the charge time for C_1, also acts as a low inductance switch for the discharge time. Figure 4 shows the measured waveforms of V0, V1, I0 and I1, respectively.

B. BPFN unit

The BPFN unit consists of ceramic capacitors, inductors, a magnetic switch (SI_2), and a high voltage step-up pulse transformer (PT_2). The voltage gain of the PT_2 is 6 (winding ratio, primary : secondary = 1 : 6). The MPC is used as a charging generator for the BPFN. The BPFN is charged by the MPC output current. A maximum BPFN charging voltage is about -20kV. The capacitance and inductance of each stage in the BPFN are 20 nF and 500 nH, respectively. Therefore, the BPFN was designed to have the characteristic impedance of 10 ohm and the output pulse width of 1 μs. Figure 5 shows the measured voltage and current waveforms of V2, V3, I3

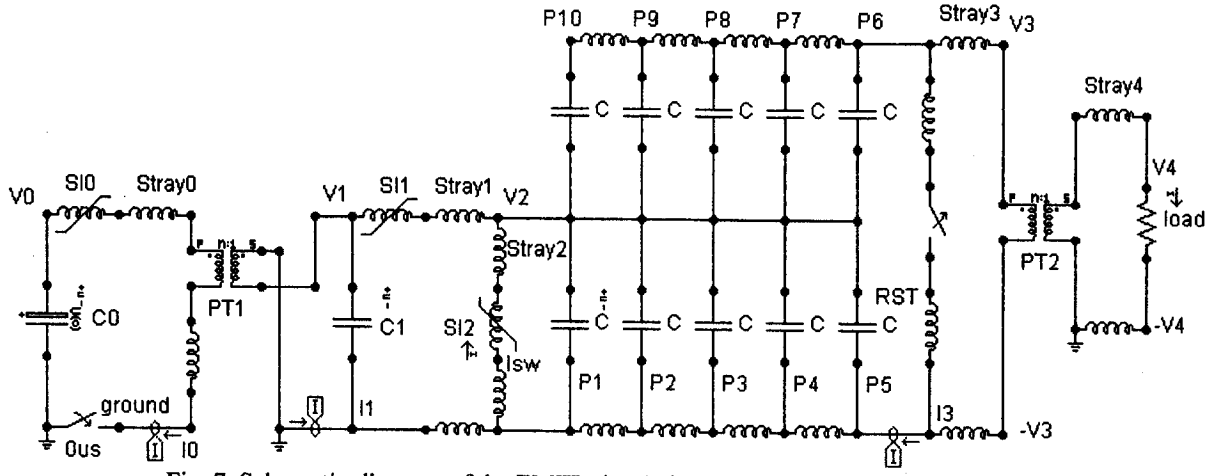

Fig. 7. Schematic diagram of the EMTP simulation circuit for the pulsed power generator.

and I_{sw}, respectively. In this figure, the charging process and the resultant output voltage of BPFN can be observed although the waveforms looks complicated due to the stray component in BPFN.

C. Load unit

The load consists of a point to plane electrode and a non-inductive resistor of 360 ohm in parallel, which is matched to the characteristic impedance of the BPFN unit. The needle to plane geometry electrode which was immersed into tap water (Conductivity: 25 mS/m) was used as the discharge electrode in this experiment. The radius of curvature at the needle tip was 30 μm. The distance between the tip of needle electrode and plane electrode was fixed at 100 mm.

Figure 6 shows the typical waveforms of the output voltage and current from the PT_2. The output voltage V4 has 3 inherent peaks, that is, Peak 1, Peak 2 and Peak 3. Peak 1 is due to the fact that the reset circuit is adopted for the maximal swing of PT 2, and that the peak appear till the core saturates in the negative direction. The Peak 1 is undesired, but it is an unavoidable result. Peak 2 is due to the un-uniform charging over the BPFN capacitors. This will be dealt with in following section. Peak 3 is the main output voltage peak. It will be observed that the peak voltage, rise time and pulse width (FWHM) were about 140 kV, 200ns and 1μs respectively.

IV. EMTP SIMULATION RESULTS

In this paper, EMTP was used to analyze the transient phenomena of the high repetition rate pulsed power generator with nonlinear elements such as the magnetic cores. Figure 7 shows the schematic diagram of the EMTP simulation circuit for the pulsed power generator which is originally based on that of figure 3.

Figure 8 shows the flux and current relationship for magnetic cores, SI0, SI1 and SI2, respectively, which were used in figure 7. The curves were derived from the B – H curves of the same magnetic core using the following relationship

$$\Phi = n \cdot B \cdot A \text{ and } I = H \cdot l / n \qquad (6)$$

Where Φ is flux, n is the number of turns, B is flux density, A is sectional area of the core, I is current, H is magnetic field, and l is average length of magnetic path of the core.

Table 1 shows the unsaturated and the saturated inductances of the magnetic switches. The ratio of the unsaturated inductance to the saturated inductance is 2240, which is due to the fact that the unsaturated relative permeability, μ_{ru} and the saturated relative permeability, μ_{rs} is calculated to 4480 and 2, respectively.

Before the performance verification of EMTP with the proposed circuit of figure 3 in comparison with the experimental results, the authors checked the stray inductances in the circuit as shown in Table 2. Stray inductances L0, L1, L2, L3 and L4 were minimized in manufacturing the pulsed power generator. Meanwhile, stray inductance L4 show quite a high value of 90 uH due to the long line to the load.

Figure 9 shows the simulated waveforms of V0, V1, I0 and I1, respectively. In the figure, energy transfer from C0 to C1 can be observed in the same way as figure 4. The simulation results show a good agreement with the experimental ones.

Figure 10 shows the simulated waveforms of V2, V3, I3 and I_{sw}, respectively. In the figure, the output voltage of the BPFN, V3 can be determined from the difference between voltage at P6 and voltage at P5 (in this case, stray inductance 3 can be neglected). Figure 11 explains the generation of Peak 2 and the output voltage V3. The output pulse has the pulse width of 1 μs, and the combination of the inductors and capacitors in the BPFN generated higher peak voltage than the charging voltage.

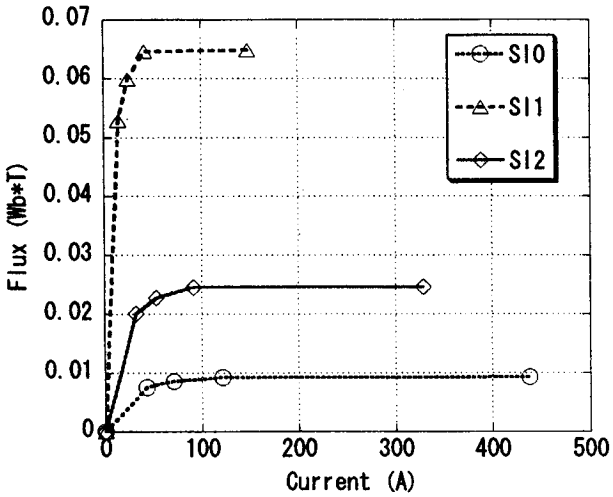

Fig. 8. Flux and current relationship for magnetic switches.

Table 1 Calculated Inductances of the magnetic switches for EMTP simulation.

	SI0	SI1	SI2
Lu	0.18 mH	3.7 mH	0.63 mH
Ls	0.08 uH	1.64 uH	0.28 uH

Table 2 Stray inductances used in the EMTP simulation circuit.

Stray L 0	Stray L 1	Stray L 2	Stray L 3	Stray L 4
0.50 uH	0.35 uH	0.16 uH	1.50 uH	90 uH

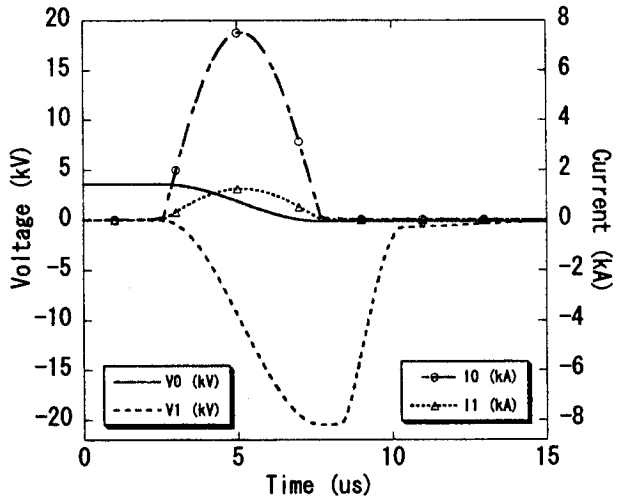

Fig. 9. Simulated waveforms of V0, V1, I0 and I1.

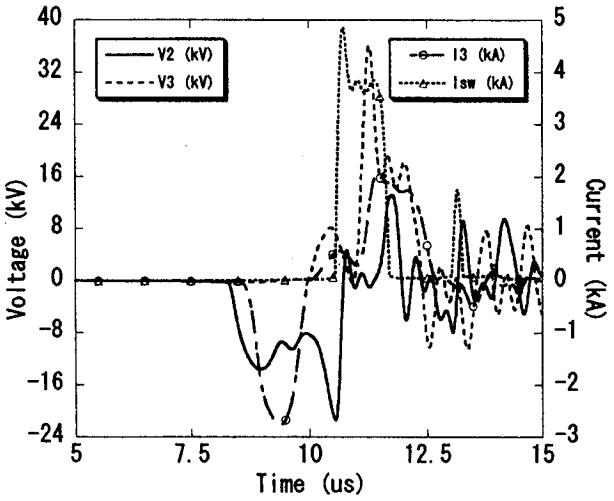

Fig. 10. Simulated waveforms of V2, V3, I3 and I_{sw}.

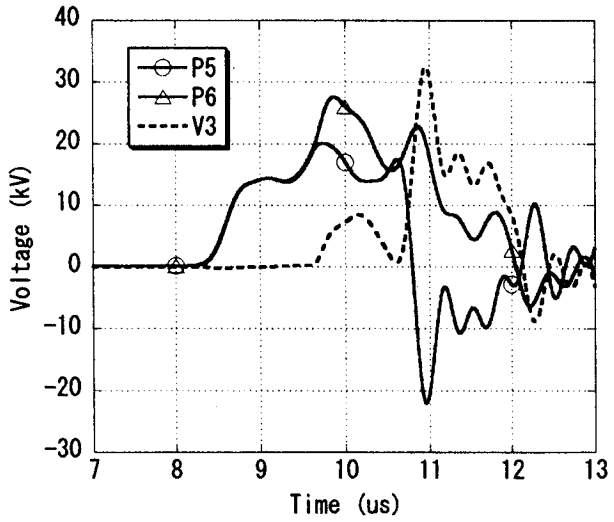

Fig. 11. Simulated voltage waveforms at point P5, P6 and V3 .

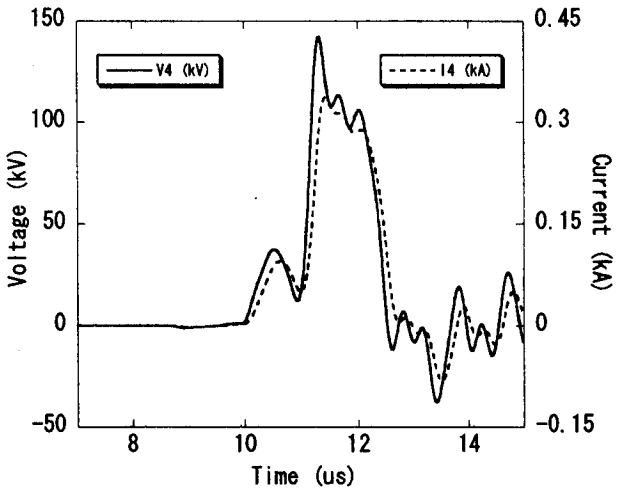

Fig.12. Simulated waveforms of V4 and I4.

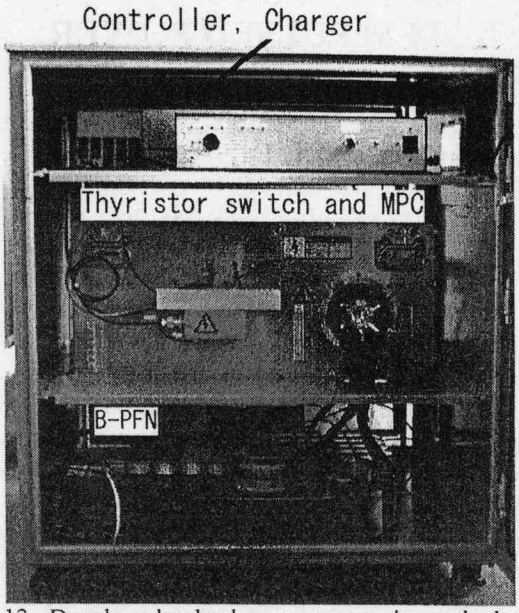

Fig. 13. Developed pulsed power system in a cube box.

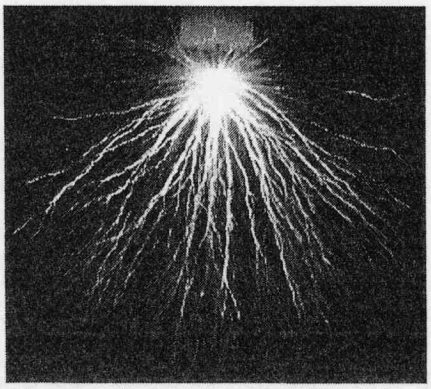
Fig. 14. Streamer discharge generated by the developed system in water.

Figure 12 shows the simulated output voltage of the over all system. It can be seen that Peak 1 in figure 6 can not be observed since the reset circuit for PT 2 was modeled as a bypass path with a switch in such a way of figure 7. By the proposed reset circuit, undesired Peak 1 was removed, while charging the BPFN was still successful.

V. STREAMER-LIKE DISCHARGE IN WATER

Large volume of streamer discharges was generated in water by the developed system as shown in figure 13. Figure 14 shows a photograph of a streamer discharge in water. The streamer discharge is growing radially from the tip of the positive point electrode. The propagation distance of the streamer is about 35 mm. These streamer-like discharges in water can produce a high electric field, high energy electrons, ozone, chemically active species, ultraviolet rays and shock waves, which readily sterilize microorganisms and decompose molecules and materials.

VI. CONCLUSIONS

The authors have developed an all solid state pulsed power generator, which is operated with high repetition rate, long lifetime and high reliability for industrial applications. The output voltage showed the peak voltage, rise time and pulse width (FWHM) of about 140 kV, 200ns and 1μs, respectively.

The feasibility of EMTP simulation for more efficient design of the pulsed power generator with MPC and BPFN was successfully studied with a good consistency with the experimental results.

Moreover, water discharges generated by the developed system succeeded.

VII. REFERENCES

[1] Melville W. S. "The Use of Saturable Inductors as Discharge Devices for Pulse Generators". *Proc. IEE* 98 (1951) 185-207

[2] S. Nakajima, S. Arakawa, Y. Yamashita and M. Shiho, "Fe-based nanocrystalline FINEMET cores for induction accelerators", Nuclear Instruments and Methods in Physics Research A 331 (1993) 318-322

[3] T. Sakugawa, H. Akiyama, "An all-solid-state pulsed power generator using a high-speed gate-turn-off thyristor and a saturable transformer", Electrical Engineering in Japan, Vol. 140, No. 4, pp.17-26, 2002

[4] W. Partlo, R. Sandstrom, I. Fomenkov, "A low cost of ownership KrF excimer laser using a novel pulse power and chamber configuration" , The International Society for Optical Engineering-SPIE , Vol. 2440, p.90, 1995

[5] T. Namihira, S. Tsukamoto, D. Wang, S. Katsuki, R. Hackam, H. Akiyama, Y. Uchida and M. Koike, "Improvement of NOx removal efficiency using short width pulsed power", IEEE Transactions on Plasma Science, Vol. 28, No. 2, pp.434-442, 2000

[6] Z. He, J. Liu, W. Cai, "The important role of the hydroxy ion in phenol removal using pulsed corona discharge", Journal of Electrostatics, Vol. 63, (Is. 4), pp. 371-386, (May 2005)

[7] E. Njatawidjaja, A. T. Sugiarto, T. Ohshima, M. Sato, "Decoloration of electrostatically atomized organic dye by the pulsed streamer corona discharge", Journal of Electrostatics, Vol. 63, (Is. 4), pp. 353-359, (May 2005)

[8] Paul W. Smith, "Transient Electronics Pulsed Circuit Technology", John Wiley & Sons, Ltd. 2002.

[9] Youngwook Choi *et al.*, "Analysis of the Pulsed Plasma Reactor Impedance for DeSOx and DeNOx", Jpn. J. Appl. Phys. Vol. 40 (2001) pp. 1108-1113.

PRODUCTION OF ATMOSPHERIC-PRESSURE GLOW USING INDUCTIVE ENERGY STORAGE SYSTEM PULSED POWER GENERATOR

K. Takaki, H. Kirihara, C. Noda, S. Mukaigawa, and T. Fujiwara

Iwate University, 4-3-5 Ueda, Morioka, Iwate 020-8551, JAPAN

ABSTRACT

An atmospheric pressure glow discharge was generated using a needle-array electrode in nitrogen, and the voltage-current characteristics of the glow discharge were obtained in a range from 1 mA to 60 A. A pulsed high-voltage with short rise time under 10 ns was used to generate homogeneous streamer whole discharge space simultaneously, which prevent the glow-to-arc transition caused by inhomogeneous thermalization. Semiconductor opening switch diodes were employed as opening switch to shorten the rise time. The glow voltage was almost constant until the discharge current became 0.3 A, whereas the voltage increased with the current higher than 0.3 A. Electron density and temperature in a positive column of the glow discharge at 60 A were obtained to 1.4×10^{12} cm^{-3} and 1.3 eV from calculation based on nitrogen swarm data.

1. Introduction

Research on atmospheric pressure glow discharges (APGD) is motivated by applications such as instantly activated reflectors and absorbers for electromagnetic radiation, surface modification, thin film deposition, dry etching, remediation and detoxification of gaseous pollution, sterilization, and light sources as gas lasers and excimer radiation [1]-[5]. Much of the efforts in generating stable glow discharges at atmospheric pressure have focused on preventing the onset of instabilities, particularly in the region close to the cathode, because of high electric field and consequently high power deposition compared to that in the positive column of the discharge [6].

A pulse voltage on preventing the thermal instability is commonly employed in the laser community to generate the pulsed glow discharges operated at current densities above threshold for the glow-to-arc transition [7]. This paper describes the generation of APGD in nitrogen gas using pulsed power supply which can generate pulse voltage consisted of a narrow over-voltage pulse and a long width pulse. A needle-array electrode instead of planar electrode was used to generate streamer discharges homogeneously between the electrodes and to keep the glow discharge stable for long duration. The properties of the APGD plasma such as voltage-current (V-I) characteristics, an electron density and an electron temperature are also described.

2. Experimental Setup

A schematic diagram of the experimental facilities is shown in **Fig. 1**. The grounded electrode plate with rounded edges is made of brass and set in the discharge chamber. The overall diameter and thickness of the electrodes are 10.7 cm and 1.5 cm, respectively. The needle-array electrode made of brass is set to the upper part of the chamber. The needle-array electrode consists of 331 needles which have a dimension of 1.3 cm in height and 50 μm in radius of the tip. Typical gap length d from needle tip to the electrode surface is 1.0 cm. The discharge chamber is evacuated with a rotary pump and is filled with the nitrogen gas to atmospheric pressure.

The power supply consists of 8.0 nF capacitor C, gap switch, 20 μH inductor L and semiconductor opening switch (SOS) diode. The capacitor C is charged up negatively to the voltage V_0 using a DC high voltage power supply. The charges are released from the capacitor by switching-on the gap switch mechanically, as the results, the current flow to the LC circuit through the SOS diode as forward-pumping current [8]. After the current direction reverses with LC oscillation, the reverse current is injected into the SOS. With the current

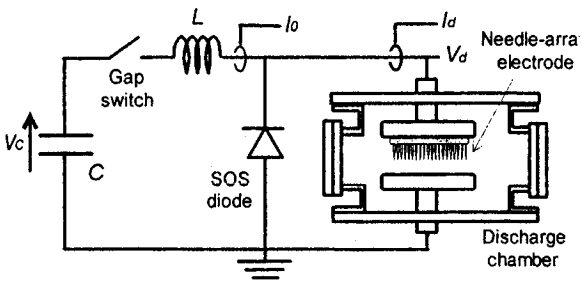

Figure 1 A schematic diagram of the experimental facilities used for generation of the atmospheric pressure glow discharge.

interrupted by the SOS, the high voltage pulse is applied to the needle-array electrode as a short nanosecond pulse. **Figure 2** shows the typical waveforms of the circuit current I_0, the capacitor voltage capacitor V_C, and the output voltage V_{out} which is measured at point of V_d shown in Fig. 1 without connecting to the discharge load. This nanosecond pulse produces the streamer discharges from all needle tips simultaneously. The streamer discharges are followed by the glow discharge with the charge remained in the capacitor C as shown by V_C in Fig. 2. The current and voltage are measured with Pearson 2878 current transformers and Sony-Tektronix high-voltage P6015A probes. The signals stored in a digitizing oscilloscope Tektronix TDS3054B are transmitted to a personal computer through a GP-IB cable in order to calculate the energy consumed in the discharge.

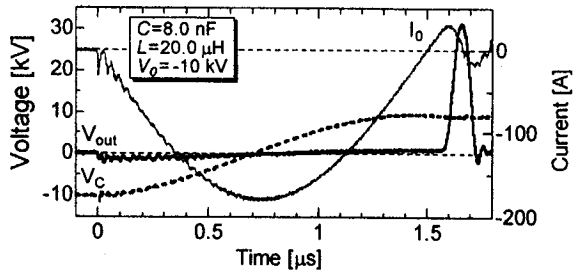

Figure 2 Typical waveforms of circuit current and voltages of the capacitor and the semiconductor opening switch diode at -10 kV charging voltage.

3. Experimental Results

3.1 Glow-to-arc transition

Representative waveforms of the transient glow discharge current and the voltage between the electrodes for three different charging voltages are shown in **Fig. 3**. When the narrow over-voltage pulse is applied to the needle-array electrode, the breakdown occurs and the discharge current rises rapidly. The long pulse voltage, which has an altitude of the voltage lower than charging voltage, follows the over-voltage pulse and keeps the glow discharge in a quasi-stable state, *i.e.* a transient glow phase. The glow discharge is sustained for 3 μs at -10 kV charging voltage as shown in Fig. 3(a) with glow current from 10 A to 3 A. At the time of 3 μs, the voltage collapses to a few hundred volts with glow-to-arc transition characterized by an appearance of a luminous spot on the cathode surface [6]. Figure 3 clearly shows that the quasi-stable state glow discharge current increases with increasing the charging voltage whereas the duration of the glow phase decreases.

Figure 4 shows the transient glow duration as a function of charging voltage at various gap lengths. Clearly, the glow duration increases with reducing charging voltage and with increasing gap length.

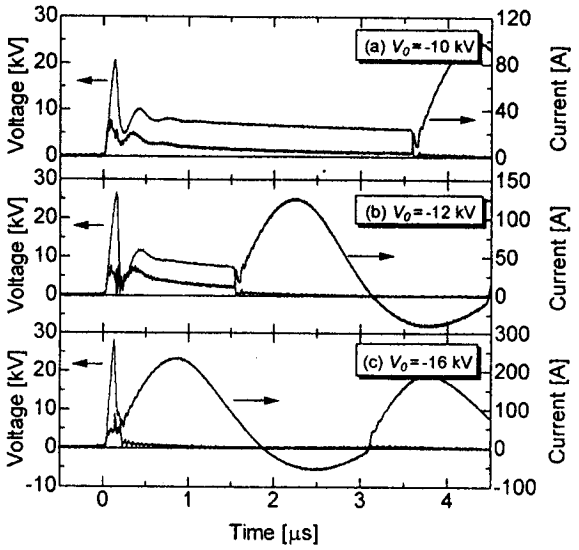

Figure 3 Voltage and current waveforms of the discharge for three different charging voltages. (C: 8 nF, L: 20 μH)

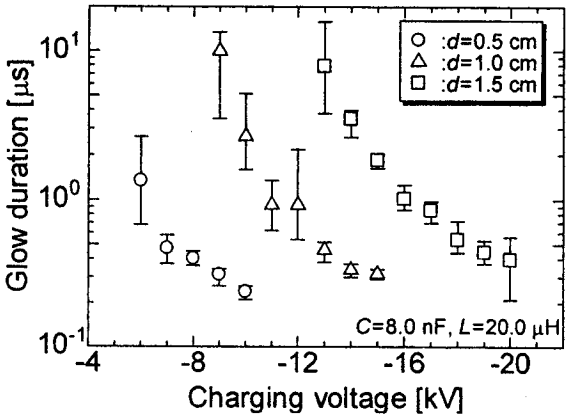

Figure 4 Glow phase duration as a function of charging voltage for three different gap lengths.

This result is due to the fact that energy fed into the discharge increases with the charging voltage and/or decreasing gap length. It was previously reported that the duration of a transient glow discharge of 3–15 A in nitrogen at pressures of 40–130 Torr is independent of gap length in a range of 0.2 to 7.0 mm [9]. This conclusion disagrees with the present result in which the glow duration depends on the gap length. The criterion for the glow-to-arc transition appears to be a certain quantity of surface density of the dissipated energy [10]. The power density on the cathode ϕ is given by

$$\phi = jV_K \qquad (1)$$

where V_K is cathode fall voltage. The current density j can be obtained by dividing glow current by the cathode area. Under the present experimental

conditions the glow current increases with gap length as shown in **Fig.5**. This means that the power density ϕ increases with the gap length. However, under the conditions of the previous work, the power density ϕ is dependent on the gap length due to the constant current density which is in agreement with the formula, $j = 400\times10^{-6}p^2$ A cm^{-2} for low-pressure normal glow discharge [7]. Thus the difference which exists in the previously reported dependence of the transient glow duration on the gap length may be explained by the different dependences of the dissipated power density on the gap length between the two investigations.

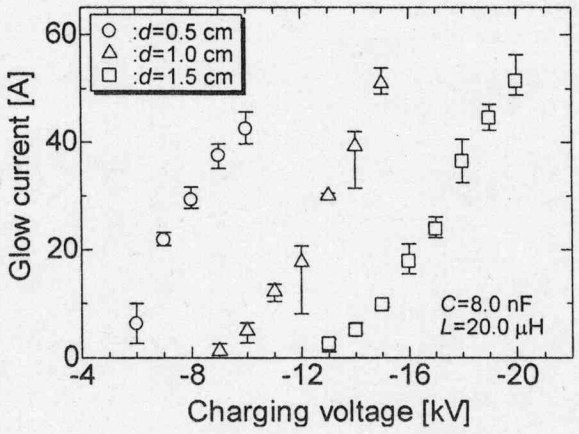

Figure 5 Glow current as a function of charging voltage for three different gap lengths.

3.2 Criterion for the glow-to-arc transition

Chalmers suggested that the criterion for a glow-to-arc transition is that a certain quantity of energy is consumed in the gap during the glow phase [11]. **Figure 6** shows the plots of the energy consumed in the discharge during the glow phase as a function of charging voltage for three different gap lengths. The consumed energies are calculated with

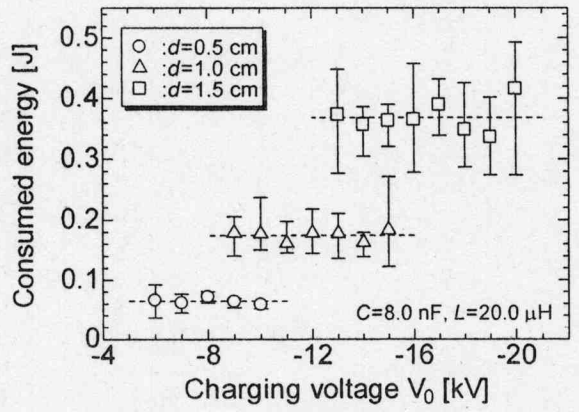

Figure 6 Consumed energy for glow-to-arc transition as a function of the charging voltage for three different gap lengths.

time-integration of the power, which is obtained by multiplying the discharge current with the voltage, during the time duration of the glow phase. The consumed energies are almost independent on the charging voltage though the measured values are scattered. The mean value of the consumed energy increases with increasing the gap length, 0.07 J, 0.17 J, and 0.37 J for 0.5, 1.0, and 1.5 cm in gap length, respectively. These values of the consumed energy can be used as a criterion for a glow-to-arc transition [6], [11]. The energy input to the discharge can be changed with the capacitor C, the inductor L, and/or inserting a damping resistor into the circuit in series. **Figure 7** shows the photographs of atmospheric glow discharge at -10 kV charging voltage. The gap length is 1.0 cm. The capacitance and the inductance are chosen to 4.2 nF and 12.6 μH, respectively, to satisfy above mentioned criterion as shown in Fig. 6. The glow discharges were generated with repetition rate of 50 Hz and the photographs were taken with exposure time of one second. The glow discharge successfully occurs without glow-to-arc transition as shown in Fig. 7. The glow discharges develop from all tips of the needle.

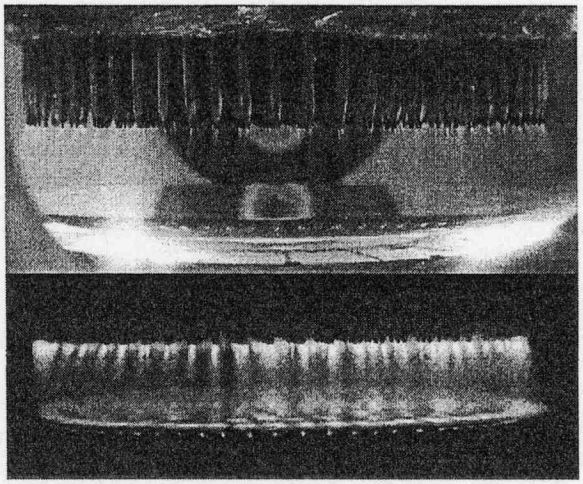

Figure 7 Photographs of atmospheric-pressure nitrogen glow discharge at 1.0 cm gap length. (C: 4.2 nF, L: 12.6 μH)

3.3 Voltage-current characteristics

A lot of processes in a direct current glow plasma are governed by the V– I characteristics of the discharge [12]. The V-I characteristics of a transient glow discharge can be obtained in wide current range from milliamps to larger than 100 A using the discharge current and the voltage waveforms [13]. **Figure 8** shows the V–I characteristics of the quasi-stable glow discharge in atmospheric pressure nitrogen gas at 1.0 cm gap length obtained in the same manner. The capacitance and the inductance are adopted as 8.0 nF and 20.0 μH, respectively. The

lines were overwritten at different charging voltage in order to obtain in wide current range. The glow voltage is almost constant, 3 kV, when the glow current is lower than 0.3 A. This independency of the voltage on the current is typical feature of a normal glow discharge [13]. The glow voltage increases from 3 kV to 14 kV with increasing glow current from 0.3 A to 60 A. The glow voltage is almost constant at lower current than 0.3 A while it increases with increasing current in a range larger than 0.3 A. This fact implies that the discharge changes from a normal glow to an abnormal glow at the discharge current of 0.3 A.

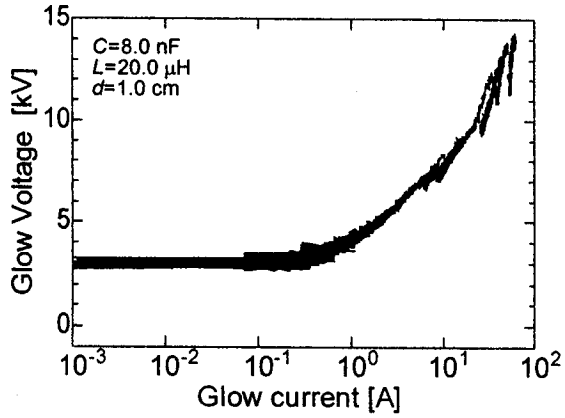

Figure 8 Current-voltage characteristics of nitrogen glow discharge at 1.0 cm gap length.

3.4 Electron density and temperature

The value of electric field in the positive column of the glow discharge can be predicted from glow voltage and cathode fall voltage, which is determined by "zero length voltage" extrapolating the potential distribution across glow discharge to zero gap length [14]. **Figure 9** shows the plotted gap voltage just prior to the glow-to-arc transition as a function of the gap length. The gap voltage

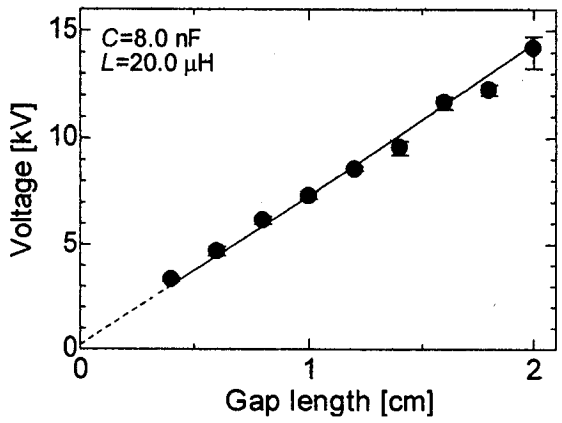

Figure 9 Glow voltage as a function of gap length for nitrogen atmospheric glow discharge.

decreases linearly with reducing gap length. The extrapolation of the potential distribution to zero gap length results in a voltage drop equal to 210 V, which is almost agree with the low-pressure data base [15]. In the normal glow mode (<0.3 A), the electric field of the positive column is roughly obtained to be 2.8 kV/cm, which is consistent to 1.1×10^{-16} Vcm^2 in reduced electric field *E/N*. The electron temperature Te can be calculated from swarm parameters of electrons in nitrogen as well-known Einstein's equation,

$$k_B T_e/e \approx D_e/\mu_e \qquad (2)$$

where μ_e, k_B and D_e are drift mobility, Boltzmann constant (1.38×10^{-23} JK^{-1}) and the diffusion constant, which can be expressed as a function of *E/N* [16]. As the results, the electron temperature is predicted to be 0.9 eV for the normal glow and 1.3 eV for abnormal glow at 60 A in glow current. The averaged electron density in the positive column can be estimated using formula,

$$N_e = j/eW \qquad (3)$$

where j, e, and W are current density, electron charge, and electron drift velocity, which also can be calculated as a function of *E/N* [16]. The current density j in the abnormal glow mode is determined by division of the total glow current by the cross section of the positive column; we assumed the cross section to 42.7 cm^2, which was the area of outline of needle-array positions. As the results, the electron densities are calculated to be 0.8×10^{10} cm^{-3} for normal glow (<0.3 A) and to be 1.4×10^{12} cm^{-3} for abnormal glow at 60 A in glow current.

4. Conclusion

The atmospheric pressure glow discharge was generated using a needle-array electrode in nitrogen, and the voltage-current characteristics of the glow discharge were obtained in a range from 1 mA to 60 A. The results show the glow voltage was almost constant until the discharge current became 0.3 A, whereas the voltage increased with the current higher than 0.3 A. Electron density and temperature in a positive column of the glow discharge at 60 A were obtained to 1.4×10^{12} cm^{-3} and 1.3 eV from calculation based on nitrogen swarm data.

The authors would like to thank Profs. H. Akiyama of Kumamoto University, H. Mase of Ibaraki University, and N. Sato of Tohoku University for their valuable discussions and comments. The authors would like to thank Mr. S. Kato of Iwate University for his cooperation. This work was supported by a Grant-In-Aid of Science Research from Japan Ministry of Education, Science and

Culture (JSPS Fellowship No 15075101).

References

[1] R. J. Stark and K. H. Schoenbach, *J. Appl. Phys.*, **85**, 2075-80 (1999).
[2] R. Prat, Y.J. Koh, Y. Babukutty, M. Kogoma, S.Okazaki, and M. Kodama, *Polymer*, **41**, 7355-60 (2000).
[3] T. C. Montie, K. Kelly-Wintenberg and J. R. Roth, *IEEE Trans. Plasma Sci.*, **28**, 41-50 (2000).
[4] M. J. Shenton and G. C. Stevens, *J. Phys. D: Appl. Phys.* **34**, 2761-68 (2001).
[5] E. E. Kunhardt, *IEEE Trans. Plasma Sci.*, **28**, 189-200 (2000).
[6] K. Takaki, D. Kitamura, and T. Fujiwara, *J. Phys. D: Appl. Phys.*, **33**, 1369-75 (2000).
[7] Yu. D. Korolev and G. A. Mesyats, "Physics of Pulsed Breakdown in Gases", URO-Press, Yekaterinburg, (1998), p.26, pp.133-159.
[8] M. I. Yalandin, S. K. Lyubutin, M. R. Oulmascoulov, S. N. Rukin, V. G. Shpak, S. A. Shunailov, and B.G.Slovikovsky, *IEEE Trans. Plasma Sci.*, **30**, 1700-4 (2002).
[9] T. Fujiwara,, H. Yamada, H. Taniguchi and K. Sugita, *Jpn. J. Appl. Phys.*, **31** 1470-2 (1992).
[10] T. Fujiwara, T. Sato, J. Sekikawa and H. Yamada, *J. Phys. D: Appl. Phys.* **27** 826-9 (1994).
[11] I. Chalmers, *J. Phys. D: Appl. Phys.*, **4**, 1147-51 (1971).
[12] L. J. Denes and J. J. Lowke, *Appl. Phys. Lett.*, **23**, 130 (1973).
[13] K. Takaki, D. Taguchi, and T. Fujiwara, *Appl. Phys. Lett.*, **78**, 2646-8 (2001).
[14] M. Cavenor and J. Meyer, *Aust. J. Phys.*, **22**, 155-67 (1969).
[15] K. Takaki, M. Hosokawa, T. Sasaki, S. Mukaigawa, and T. Fujiwara, *J. Adv. Oxid. Technol.* **8** (2005 in publishing)
[16] Y. Nakamura, *J. Phys. D: Appl. Phys.*, **20**, 933-8 (1987).

Energy Efficiency of Pulsed Plasma Thruster

T.Ikeda, M.Nakajima and K.Horioka

Department of Energy Sciences, Tokyo Institute of Technology, 4259 Nagatsuda, Midori-ku, Yokohama, 226-8502, Japan

A pulsed plasma thruster(PPT[1]) composed of a flashover plasma source and an electromagnetic pulsed driver is constructed and basic characteristics, such as voltage, discharge current, and plasma flux are investigated. In order to improve the specific impulse of PPTs, effects of late-time ablation on the plasma flux are discussed based on a consideration of the impedance matching between the driver and the flashover plasma. Results indicate a possibility of the impedance matching by adjusting the electrode geometry and the circuit parameter of the device.

I. INTRODUCTION

Propulsion systems can be divided into mainly two types. One is chemical propulsion generally used for launch from the earth and the other is electric propulsion which is often used in space. Exhaust speed of the propellant which most electric propulsion can achieve is 1-10 times that of chemical one by changing the propellant plasma state. High exhaust speed can save the propellant use, so electric propulsion is essential to missions in space.

As the technology in industrial world progress, diverse device can be downsized extending to satellite world, so that attention to small satellites is consequently increasing.

PPT is an electric propulsion needing no warm up time and no standby power, and particularly if solid propellant like Teflon is adopted, no tankage, feeding line and mechanical valves, so that can be easily downsized and more can get credibility which is an important element at the same time. PPTs also attract attentions for control of micro satellite which will appear in near future, because PPTs have a capability of pulsed operation and generate a tiny impulse bit as its characteristic and so can carry out precise digital control. Additionally there is a possibility of using for control and holding in oscillation for large scaled soft structure.

Development of a small thruster having high propulsion efficiency is urgently needed because satellite's life often depends on lack of the propellant. PPTs are able to operate in lower power compared to large or middle size thrusters which need relatively higher power like hall thruster or ion thruster and so on. However, PPTs also have defect; the propulsion efficiency is almost half compared with those thrusters. Recently a phenomenon called late-time ablation has been noted as the cause of the deficiency. It generates consecutive ablation from the propellant after discharge. Low energy particles caused by this phenomenon don't bring effective acceleration. Moreover, the particles having lower speed from surface of propellant consume the propellant as macro particles during the discharge. This makes the average exhaust speed lower, resulting in a decrease of propulsion efficiency. One of the factors of this macro particle formation is discordance of impedance matching of the apparatus and the generating plasma.

We fabricated a PPT which have two 1 μF oil filled condensers for main capacitor bank and measured the discharge current and the voltage waveforms. Our report includes discussion of the matching condition by changing the state of plasma and varying the voltage charged to capacitor bank.

II. EXPERIMENTAL APPARATUS

PPTs accelerate the propellant by electro-magnetic force and aerodynamic force.[2] A concept of propellant acceleration is schematically shown in Fig.1.

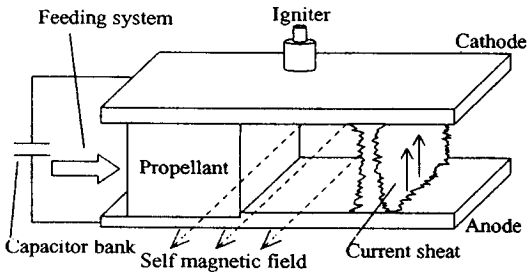

Fig.1: Schematic diagram of propellant acceleration in PPT

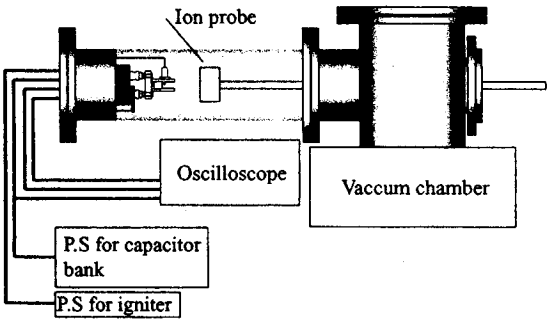

Fig.2: A sketch of experimental apparatus

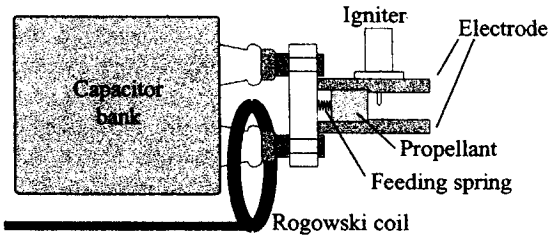

Fig.3: A sketch of our PPT

The parallel electrodes are charged to several kV by directly connected capacitor bank and a solid propellant fills the gap between the two electrodes.

When the igniter makes a high voltage pulse, a creepage discharge is induced between the igniter and the electrodes. The flashover generates a plasma on the surface of propellant filled in two electrode, then the plasma fills the electrode gap. As the plasma creates a well conductive channel, the stored charge flows at a burst mode through this channel between electrodes, and then the main discharge is induced. As the discharge deposits the electric energy onto a solid propellant surface, the propellant is ablated. Some of this ablated propellant receives gas dynamic acceleration induced by the high enthalpy gas expansion. A part of the ablated material becomes a plasma state and receives electromagnetic acceleration induced by the discharge current and self induced magnetic field. Ablated particles are exhausted from the thruster by these mechanisms. In addition, feeding system like a spring always maintains the propellant surface at same position.

Fig.2 and Fig.3 schematically displays the PPT adopted in our experiment. The PPT is arranged in a vacuum chamber at 2.5×10^{-5} torr. The PPT is driven by a 2 μF capacitor bank composed of two 1 μF condensers. Two electrodes are connected to the capacitor bank directly. The gap distance between the electrodes is 5 mm, and the width of electrode is 15 mm. This bank has charging voltage limit at 2.5 kV, so achieves maximum storage energy of 6.25 J. Using a Rogowski coil, the discharge current is measured, and a high voltage probe is used to measure the discharge voltage. To estimate the specific impulse, we use an ion probe.

III. RESULT & DISCUSSION

Fig.4 shows typical discharge current and voltage waveforms. This diagram includes the data

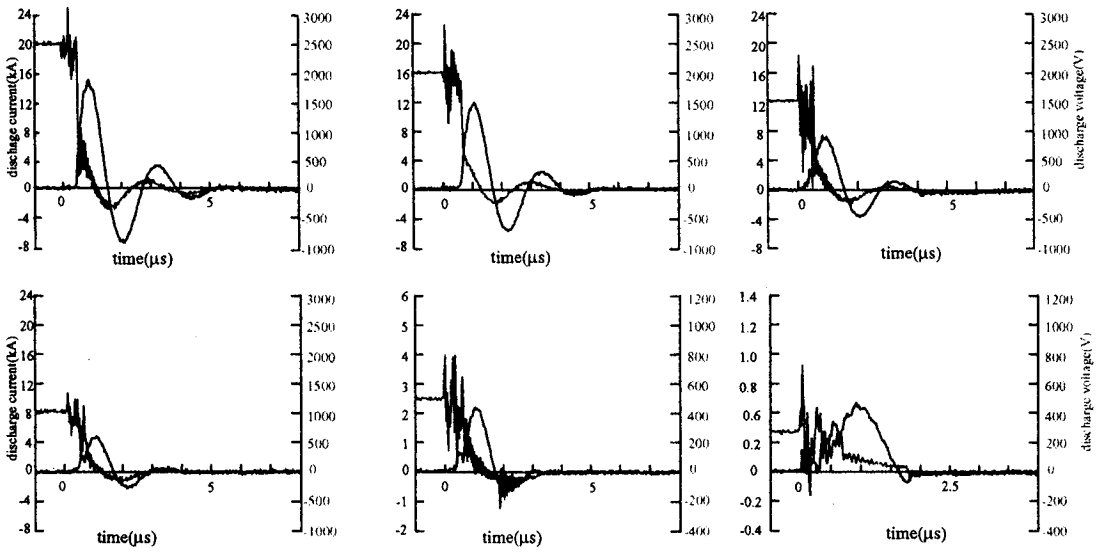

Fig.4: Typical discharge current and voltage waveforms

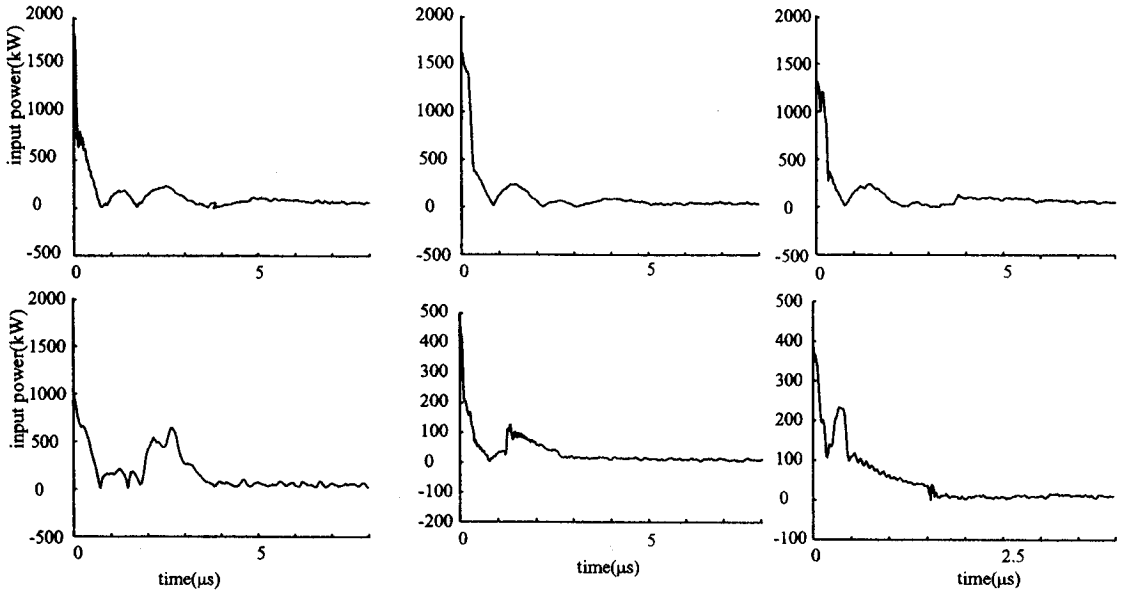

Fig.5: Typical power history

operated with charged voltages of 2.5 kV, 2.0 kV, 1.5 kV, 1.0 kV, 0.5 kV and 0.25 kV respectively. Paying attention to the current waveforms, we can see that the current peak in the second period is diminishing with decrease of the charging voltage and at 0.25 kV the waveform shifted to a critical dumping form. Even in this voltage level, the plasma luminescence generated by the flashover can be confirmed as same as other charging level, and rapid falling off cannot be observed in the current and voltage waveform. Fig.5 shows typical input power histories which are made from the absolute value of current and voltage product in Fig.4. From the figure, we can see that oscillating waveforms of input power are also gradually shifting to a simple damping waveform.

As described above, a possibility of impedance matching can be pointed out.[3-4] However, whether this impedance matching restrain the generation of low speed particles or not is necessary to know. This means we have to know how much high speed particles and low speed particles exist. In short, when we define M_t as the total propellant consumption mass, m_h as the high speed particles mass, m_l can be expressed as the low speed particles mass by;

$$m_l = M_t - m_h .$$

The prospect needs a measurement after several thousands shots because the propellant consumption mass per shot estimated to be order of μg. We can know propellant consumption mass by comparing the mass after several hundreds

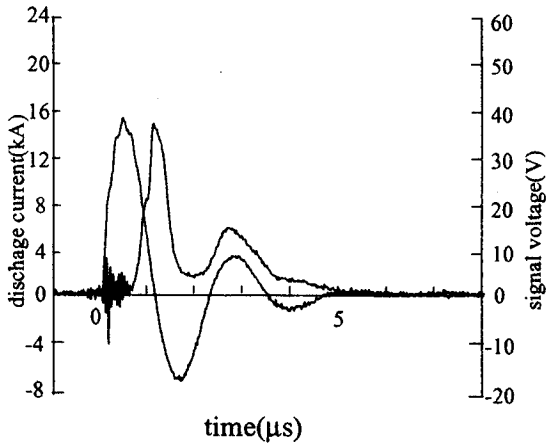

Fig.6: Typical ion probe signal at 2cm from the thruster

shots to the propellant mass measured beforehand. By the ion probe, we can get information of the plasma quantity and quality. To measure the total plasma by using this probe, we have to evaluate flux distribution.

Fig.6 shows a typical signal of the ion probe. As shown in the figure, the ion signal peaks at 0.5 μsec after the peak of discharge signal. The distance from the PPT' s front to the probe is 2 cm, accordingly the average plasma velocity is estimated to be 40 km/s. Moreover, from the waveform we can see that the plasma has two or three peaks. The waveform suggests that the second peak current also ablates the propellant surface and then second plasma is generated. If we assume that the second plasma is originated from

the second current peak, the second plasma velocity is estimated to be 20 km/s. Assuming that the plasma particles composed of high speed particles, using 40 km/s as v and 9.8 m/s^2 as g, the specific impulse of our PPT can be estimated to be 40 s from the next equation:

$$I_{sp} = \frac{v}{g}$$

To know the average velocity of the propellant, direct measurement of kinetic momentum[5] is needed because it is difficult to get precise information of the velocity profile of the plasma flow. If it is obtained, not only impulse a shot, but also the propulsion efficiency;

$$\eta_p = \frac{\frac{1}{2}\Delta m v^2}{W}$$

can be estimated, using the total electric energy W.

IV. SUMMARY

We have pointed out a possibility of impedance matching between generating plasma and the apparatus by the current of electric component and the discharge geometry, in this paper. By the ion probe measurement, we can approximately estimate the velocity of high speed particles. To get more information of the plasma flow, we are planning to use a fast streak camera to get the image data.

We are also planning to investigate the effect of electrode geometry and the input energy history on the formation of low energy particles.

As a future work, investigation is needed to know how impedance matching relate to the generation of low speed particles, by changing the input energy, electrodes geometry, including the electrode's width and the gap length.

REFERENCES

[1]Guman, W. J. and Williams, T.E. , "Pulsed Plasma Microthruster for Synchronous Meteorological Satellite (SMS)", AIAA Paper 73-1066, Nov., 1973.

[2]Jhan, R.G, "Physics of Electric Propulsion", McGraw-Hill, New York, 1968.

[3]Burton, R. L. and Turchi, P. J. "Pulsed Plasma Thruster", Jornal of Propulsion and Power, Vol.14, No.5,1998, pp.716-735.

[4]Gregory G Spanjers, Jason S. Lotspeich, Keith A. McFall, Ronald A. Spores, "Propellant Losses Because of Particulate Emission in a Pulsed Plasma Thruster", Jornal of Propulsion and Power, Vol4, No.4, 1998, pp.554-559.

[5]Cutler,W.H. , "Development of a microthrust stand for direct thrust measurement", AIAA Paper 68-577

Characteristics of Bipolar-Pulse Generator for Intense Pulsed Heavy Ion Beam Acceleration

K. Igawa, T. Tomita, I. Kitamura, H. Ito and K. Masugata
Faculty of Engineering, University of Toyama
3190 Gofuku, Toyama, 930-8555, Japan

Abstract

Intense pulsed heavy ion beams are expected to be applied to the implantation technology for semiconductor materials. In the application it is very important to purify the ion beam. In order to improve the purity of an intense pulsed ion beams we have proposed a new type of pulsed ion beam accelerator named "bipolar pulse accelerator (BPA) ". A prototype of the experimental system has been developed to perform proof of principle experiments of the accelerator. A bipolar pulse generator has been designed for the generation of the pulsed ion beam with the high purity via the bipolar pulse acceleration and the electrical characteristics of the generator were evaluated. The production of the bipolar pulse has been confirmed experimentally.

1. Introduction

Intense pulsed heavy ion beams (PHIB) have a wide area of applications including nuclear fusion and materials science, etc. In the past two decades, the PHIB has been used as a tool for surface modification process of materials[1-4] and a crystallization process of thin films[5]. The PHIB is also expected to be applied to a new ion implantation technology i.e. "pulsed ion beam implantation"to semiconductor, since the doping process and annealing process can be completed in the same time.

The PHIB can easily be generated in conventional magnetically insulated ion diodes using a flashboard ion source. However, the purity of the beam is usually very poor since many kinds of ions are produced simultaneously in the flashboard ion source. For example, the PHIB produced in a point pinch ion diode contains much kind of ions including protons, multiply ionized carbons, and organic ions[6]. Hence, the application of the PHIB to the pulsed ion beam implantation has been extremely limited.

A new type of pulsed ion beam accelerator named "bipolar pulse accelerator (BPA) "has been proposed in order to improve the purity of an intense pulsed ion beams[7]. A prototype of the experimental system was constructed to confirm the principle of the BPA[8]. The system utilizes B_y type magnetically insulated ion diode with an ion source of a coaxial gas puff plasma gun and operated with single polar negative pulse. The ions are successfully accelerated from the grounded anode to the drift tube by applying negative pulse of voltage 240 kV with the pulse duration of 100 ns to the drift tube. Pulsed ion beam with the current density 90 A/cm^2 and the pulse duration 50 ns was obtained at 40 mm downstream from the anode surface. It was found from Thomson parabola spectrometer (TPS) measurement that the ion beam consists of N^+ and N^{2+} with the energy 150-300 keV.

As the next step of the development of the BPA, a bipolar pulse generator was developed to carry out the bipolar pulse acceleration experiment. The design parameters of the bipolar pulse generator are negative and positive pulses of voltage ±200 kV and pulse duration 70 ns each. In the developed generator, the multichannel rail gap switch with an enhanced trigger circuit is employed as a main switch of a pulse forming line to generate the bipolar pulse. The characteristic of the switch and the electrical characteristics of the generator were evaluated. In this paper, these experimental results are described.

2. Basic concept of bipolar pulse accelerator

Figure 1(a) shows the conceptual drawing of the bipolar pulse accelerator. For comparison a conventional PHIB diode is also shown in Fig.1(b). The proposed BPA consists of a grounded ion source, a drift tube and a grounded cathode. As seen in Fig.1(a), The BPA is a 2-stage accelerator and operated with a bipolar pulse. When the bipolar pulse (V_1) is applied to the drift tube, ions produced in the grounded ion source are accelerated in the 1st gap toward the drift tube because at first the negative voltage pulse with the pulse duration τ_p is applied. After τ_p the polarity of the pulse is reversed and the positive voltage with the duration τ_p is applied to the drift tube. As a result, the ions are again accelerated in the 2nd gap toward the grounded cathode. The condition for the most effective acceleration is that the pulse duration of the negative voltage is adjusted to the time of flight delay of ions to pass through the drift tube, i.e. $\tau_p = L/v_i$, where v_i is the ion velocity after accelerated in the 1st gap and L is the length of the drift tube. This condition can be satisfied by adjusting the parameter of the bipolar pulse and the drift tube length. In the above condition, when the top of the ion beam reaches the 2nd gap the pulse is reversed and the whole ion beam is accelerated effectively. As seen in Fig.1, the merit of the proposed BPA is that the ion source can be installed on the grounded anode, while in the conventional PIB diode, the ion source is placed on the anode where the high voltage pulse is applied. This seems to be favorable for the active ion sources where ion source is powered by an external power supply.

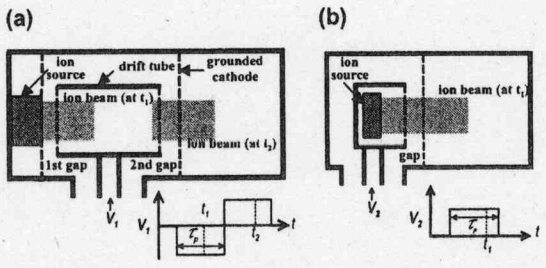

Fig.1 Conceptual drawing of (a) bipolar pulse accelerator and (b) conventional pulsed ion beam accelerator.

As above mentioned the bipolar pulse accelerator has the advantage of the improvement of the purity of the ion beam. As shown in Fig.2, assuming that ion source contains N^+ and impurity ions of H^+ in the proposed diode, let us consider the acceleration of the ions. In the case, ions of N^+ and H^+ are accelerated in the 1st gap toward the drift tube when the negative voltage is applied, where N^+ and H^+ ion beams are schematically described in Fig.2. As seen in this figure, the length of H^+ beam is much longer than that of N^+ due to the difference of the velocity. Here assuming that the length of the drift tube is designed to be same as the beam length of N^+ of duration τ_p at acceleration voltage V_p, it is, for example calculated to be 11.6 cm when $V_p = 200$ kV and $\tau_p = 70$ ns. When the voltage is reversed and the positive voltage is applied to the drift tube at $t = t_1$, N^+ beam of length 11.6 cm in the drift tube is accelerated in the 2nd gap. In contrast, since length of H^+ beam at $V_p = 200$ kV and $\tau_p = 70$ ns is 43.3 cm, 73 % of the beam is out of the drift tube at t_1 and it is not accelerated in the 2nd gap. Hence 73 % of H^+ beam is removed in the accelerator.

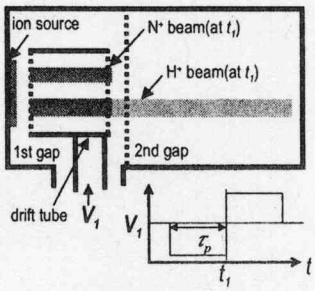

Fig.2 Principle of the improvement of the purity of the ion beam.

3. Experimental Setup

Figure 3 shows the cross-sectional view of the bipolar pulse generator developed in the present experiment. The output parameters of the designed generator are (-200 kV, 7 Ω, 70 ns) + (+200 kV, 7 Ω, 70 ns). The generator consists of a Marx generator and a water coaxial type pulse forming line (PFL). As shown in Fig.1(a), the line consists of three coaxial cylinders with a rail gap switch connected between the intermediate and the outer conductors on the end of the line and is charged

by a low inductance Marx generator with the output voltage 300 kV and the stored energy 1.6 kJ at a charging voltage(V_G) of 50 kV. The waveform of the bipolar pulse is very sensitive to the performance of the rail gap switch, that is, the time to reverse the pulse is dependent on the inductance of the switch. In order to realize the bipolar pulse with the fast reversing time and the fast rise time, the multichannel rail gap switch with an enhanced trigger circuit is utilized as the main switch of low inductance. The rail gap switch is operated with pure SF_6 and a mixture of SF_6 with N_2. The detailed structure of the rail gap switch is shown in Fig.3(b). The rail gap switch is constructed of a pair of main electrodes and a trigger electrode. The knife edged trigger electrode is placed between the main electrodes. These electrodes are carefully aligned and installed in the acrylic vessel.

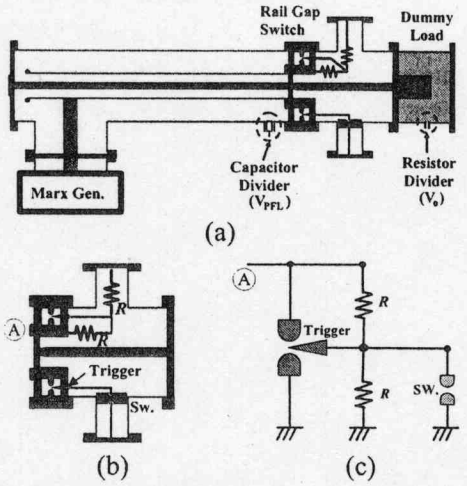

Fig.3 (a) Cross sectional view of the bipolar pulse generator utilized in experiment. (b) Detailed structure of rail gap switch. (c) Trigger circuit of rail gap switch.

Figure 3(c) shows the circuit of the rail gap switch with the enhanced trigger circuit. The trigger circuit consists of resistors of divider(R) and a self-breakdown spark gap switch, where ceramic resistors of 100 Ω are utilized as R. In the circuit, point A is connected to the intermediate conductor of the line and the trigger electrode is kept at the half of the charging voltage of the line in the charging phase. When the discharge gap switch is self-broken the potential of the trigger electrode is dropped to the ground level. As a result, breakdown of the rail gap switch is initiated and the bipolar pulse is transmitted to the load.

4. Experimental Results

Figure 4 shows the typical waveforms of the charging voltage of the PFL (V_{PFL}) and bipolar pulse output (V_0) and the photograph of the rail gap switch, where the rail gap switch is filled with the mixture of SF_6 with N_2 (SF_6 : N_2=1 : 1, total pressure 4.8 atm) and the pressure of the spark gap switch (SW) is optimized to produce a trigger pulse. The capacitive voltage divider and the resistor divider are applied to measure V_{PFL} and V_0, respectively (see Fig.3(a)). The production of the bipolar pulse has been confirmed by the experimental result in which the bipolar pulse of the first pulse (-115 kV, 65 ns) and the second pulse (+80 kV, 60 ns) can be seen just after the charging voltage of PFL reaches the peak 240 kV at $t \approx 185$ ns and the rail gap switch is triggered. The peak voltage of negative pulse is almost equal to the half of the PFL charging voltage as be expected. In contrast the voltage of positive pulse is smaller. The reduction of the voltage in the 2nd pulse seems to be due to the resistance of the rail gap switch. The bipolar pulse seems to be dull waveform with the rise time of 30 ns and the reversing time of 40 ns. This is considered to be due to the impedance mismatch between the PFL and the transmission line and to switching inductance of the rail gap switch.

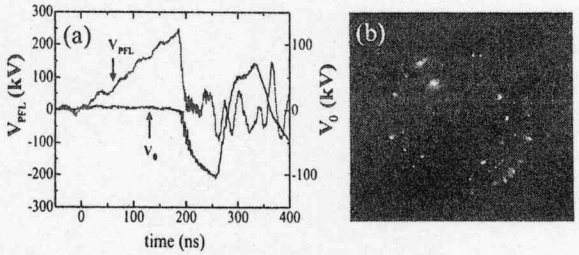

Fig.4 (a) Typical waveforms of PFL charging voltage (V_{PFL}) and bipolar pulse(V_0). (b) Photograph of rail gap switch at the shot.

It is found from Fig.4 that the number of conducting channels in the rail gap is around 15 and that the falling time (90-10 % fall time) of V_{PFL} is 10 ns. Considering that the characteristic impedance of the line between the outer and

intermediate conductors is 6.7 Ω, the switching inductance is estimated to be 22 nH.

For comparison, Fig.5 shows the waveforms of the PFL charging voltage in the case of (a) the rail gap switch is operated in triggered mode and (b) in self-breakdown mode when the rail gap switch was filled with pure SF_6. The fall time of V_{PFL} in the case with trigger and without trigger are 13 ns and 19 ns, respectively. Estimating the switching inductance from the fall time in the same manner, the corresponding inductances are 29 nH and 42 nH, respectively. This estimation indicates that the switching inductance is reduced by using enhanced trigger circuit and the mixed gas. In Ref.[9], it is reported that the switching inductance of the multichannel rail gap switch can be reduced to less than 10 nH when using the mixture of SF_6 with N_2. Although the bipolar pulse can be produced by the developed generator, there seems to be need for making improvements including the performance of the rail gap switch.

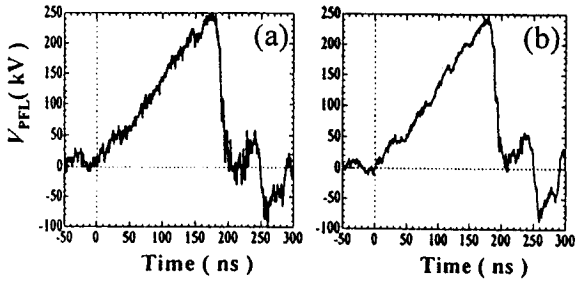

Fig.5 Waveforms of the PFL charging voltage for the case (a) with trigger and (b) without trigger.

5. Summary

We have developed the bipolar pulse generator to carry out proof of principle experiments of the bipolar pulse accelerator. The production of the bipolar pulse has been confirmed experimentally We have found that the performance of the rail gap switch is improved by using enhanced trigger circuit and the mixture of SF_6 with N_2. Further improvements of the bipolar pulse generator are now undertaken in order to produce the bipolar pulse with sharp rise time and reversing time.

Acknowledgement

This work is supported in part by the Research Foundation for the Electro Technology of Chubu and the Grant-in-Aid for Scientific Research from the Ministry of Education, Science, Sports and Culture, Japan.

参考文献

[1] A.D. Pogrebnjak, G.E. Remnev, I.B. Kurakin, A.E. Ligachev, Nucl. Instrum. & Methods in Phys. Res. B **36**, 286 (1989).

[2] G.E. Remnev and V.A. Shulov, Laser Particle Beam **11**, 707 (1993).

[3] D.J. Rej, H.A. Davis, M. Nastasi, J.C. Olson, E.J. Peterson, *et al.*, Nucl. Instrum. & Methods in Phys. Res. B **127/128**, 987 (1997).

[4] B.X.Han, H.T.Zhang, W.J.Zhao, S.Yan, X.Y.Le, W.Xiang, T.M.Wang, G.E.Remnev, Suf. Coat. Technol. **158/159**, 482 (2002).

[5] K. Masugata, Y. Fujioka, R. Tejima, I. Kitamura, H. Tanoue, and K. Arai Proc. of 4th Int. Symp. on Pulsed power and Plasma applications and Int, Workshop on applications of Pulsed Power to Nanosized Materials, (Nagaoka, Japan, 2003) pp.291-295.

[6] K. Masugata, H. Okuda, K. Yatsui and T. Tazima, J. Appl. Phys. **80**, 4813 (1996).

[7] K. Masugata, Nuclear Instrum. & Methods in Phys. Res. A **411**, pp.205 (1998).

[8] K. Masugata, Y. Shimizu, Y. Fujioka, I. Kitamura, H. Tanoue and K. Arai, Nucl. Instrum. & Methods in Phys. Res. A **535**, 614 (2004).

[9] K. Masugata, H. Tsuchida, H. Saitou, and K. Yatsui, IEEE Trans. on Plasma Science **25**, 97 (1997).

Development of Intense Pulsed Heavey Ion Beam Diode Using Gas Puff Plasma Gun as Ion Source

H. Ito, M. Higashiyama, S. Takata, I. Kitamura and K. Masugata
Faculty of Engineering, University of Toyama
3190 Gofuku, Toyama, 930-8555, Japan

Abstract

A magnetically insulated ion diode with an active ion source of a gas puff plasma gun has been developed in order to generate a high-intensity pulsed heavy ion beam for the implantation process of semiconductors and the surface modification of materials. The nitrogen plasma produced by the plasma gun is injected into the acceleration gap of the diode with the external magnetic field system. The ion diode is operated at diode voltage $\approx$ 200 kV, diode current $\approx$ 2 kA and pulse duration $\approx$ 150 ns. A new acceleration gap configuration for focusing ion beam has been designed in order to enhance the ion current density. The experimental results show that the ion current density is enhanced by a factor of 2 and the ion beam has the ion current density of 27 A/cm^2. In addition, the coaxial type Marx generator with voltage 200 kV and current 15 kA has been developed and installed in the focus type ion diode. The ion beam of ion current density $\approx$ 54 A/cm^2 is obtained. To produce metallic ion beams, an ion source by aluminum wire discharge has been developed and the aluminum plasma of ion current density $\sim$ 70 A/cm^2 is measured.

1. Introduction

High-intensity pulsed heavy ion beam (PHIB) technology has been developed over the last two decades primarily for nuclear fusion and high energy density physics research [1]. One of most interesting topics is the application of PHIB to develop a unique pulsed energy source as a tool for the surface modification of materials [2,3]. Compared with conventional ion implantation, the PHIB process possesses high power density and short pulse width to rapidly melt, evaporate, or ablate a thin surface layer of treated materials at high heating and cooling rate of $10^8 - 10^{11}$ K/s. Due to the characteristics of PHIB technology, its application for the surface engineering currently focuses on two aspects, i.e. PHIB irradiation to modify the surface of materials [4-6] and PHIB ablation to deposit the thin film [7]. Especially for the implantation process, PHIB technique has received extensive attention as a new type of ion implantation technology, since the ion implantation and the surface heat treatment or the surface annealing can be completed in the same time [8].

The pulsed ion beams usually are generated in conventional magnetically insulated ion diodes (MID) with transverse magnetic field in the acceleration gap to suppress the electron flow and enhance the ion flow. The conventional MID, however, has the fault that the producible ion species is limited to the material of electrode and that the beam usually contains much quantity of impurity ions [9,10], since the surface flashover ion source is used. Therefore, the conventional pulsed ion diode is not suitable for the implantaton process. We have developed a new type of By type MID with an active ion source of a gas puff plasma gun in order to produce the PHIB with acceptable purity. The nitrogen ion beam with ion current density $\sim$ 13 A/cm^2 and the purity of the beam $\sim$ 85 % has been obtained at 55 mm downstream from the anode [11]. The ion current density, however, is not intense enough to apply PHIB to the implatation process.

A new electrode of ion diode for focusing ion beams has been designed and installed in MID to enhance the ion current density. We also have developed the coaxial type Marx generator with volt-

age 200 kV and current 15 kA as the pulsed power generator of ion diode. The generator has power energy enough to generate the high-intensity PHIB for the implantation process. In this paper, we report experimental results on the generation of nitrogen ion beam. In addition, the preliminary results of the experiment on the pulsed metallic ion source by a wire discharge are described.

2. Experimental Setup

A schematic configuration of the intense pulsed heavy ion diode system is displayed in Fig.1. The system consists of a high voltage pulsed power generator, a gas puff plasma gun, a B_y type magnetically insulated ion acceleration gap (diode), and a stainless-steel vacuum chamber with a diffusion pump package. The vacuum chamber is evacuated to 5×10^{-3} Pa. The pulsed power generator used in the experiment consists of a fast capacitor bank and a multi-turn step up transformer using magnetic cores of amorphous metal. The capacitor bank of maximum charging voltage 50 kV produces a high power pulse of pulse duration about 150 ns (FWHM) and the pulse voltage is magnified by the step up transformer with winding ratio 1:9. The output parameter of the generator is voltage 200 kV, current 2 kA and pulse duration 150 ns, which is applied to the anode of the ion diode.

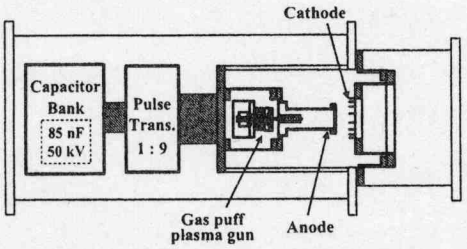

Fig.1 Schematic of the Ion Diode System.

Figure 2 shows the detail of the ion diode. The diode consists of a cylindrical anode of 115 mm length by 60 mm diameter at the top and a cathode of grid structure. The top of the anode is a copper plate, in which 37 holes of 5 mm diameter are drilled at the central area of anode in order to allow the source plasma to inject into the acceleration gap. The cathode has a grid structure to pass through the accelerated ions. The cathode also acts as a multi-turn magnetic field coil in order to generate a transverse magnetic field in the acceleration gap to insulate the electron flow and enhance the ion flow. Thus, as shown in Fig. 2, the cathode (coil) has a shape like 8-character and is made of phosphor bronze strip of 10 mm width and 1 mm thickness. The coil is powered by a capacitor bank of 250 μF and charging voltage 5 kV. By applying a pulse current of 10 kA with rise-time 50 μs, a uniform magnetic field of 0.8 T is produced in the gap.

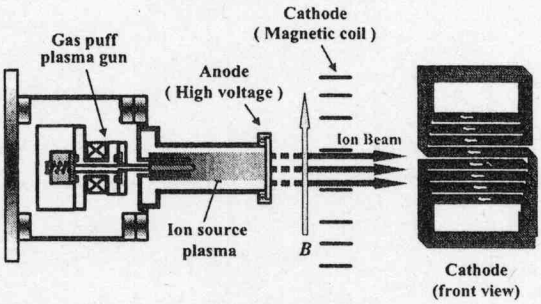

Fig.2 Cross-sctional view of B_y type MID.

The gas puff plasma gun is used as the ion source in order to produce the pulsed ion beam with high purity and is installed inside the anode. The plasma gun consists of a coaxial plasma gun and a high-speed gas puff valve. The plasma gun has a pair of coaxial electrodes, i.e. an inner electrode of 80 mm length by 6 mm outer diameter and an outer electrode of 18 mm inner diameter. The inner electrode has six gas nozzles of 1 mm diameter. The gas puff valve consists of a nylon vessel, an aluminum valve and a driver coil. The vessel is pre-filled with N_2 gas up to 1.4 atm. By discharging the capacitor bank of 20 μF and charging voltage 5.5 kV, a pulsed strong magnetic field is produced in the driver coil, which pushes the valve. As a result, the valve opens quickly in the time order of 100 μs and the gas expands with a supersonic velocity and is injected into the plasma gun via the nozzles on the inner electrode. After the injection of the gas, the ion source plasma is produced by discharging the capacitor bank of the plasma gun with the optimal delay time, since it takes $\sim$ 150 μs to open the valve and several tens μs for N_2 gas to reach the gas nozzle on the inner electrode of the plasma gun. The ion current density of the plasma produced by the plasma gun is

estimated to be 28 A/cm^2 by a biased ion collector (BIC) placed at z = 90 mm downstream from the top of the plasma gun where the anode is placed in the acceleration experiment. The capacitor bank 3.3 μF for the plasma gun is charged up to 17 kV.

Figure 3 shows a schematic drawing of the focus type diode. The ion diode is basically same as the diode shown in Fig.2 but both the anode and the cathode have a spherical configuration to achieve geometrical focusing of the PHIB. The radii of curvature of the anode and cathode are 80 mm and 70 mm, respectively. In the experiment the acceleration gap length d_{A-K} is adjusted to 10 mm. The diode voltage (V_d) and diode current (I_d) are measured by the capacitive voltage divider and Rogowski coil, respectively. The values of diode voltage and diode current is calculated by the ratio factor of the voltage divider 136000 and the coefficient of the Rogowski coil 27 kA/V. For the measurement of the ion current density BIC is used.

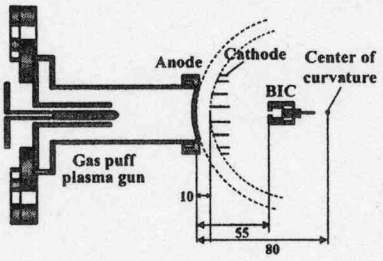

Fig.3 Schematic drawing of focus type ion diode and experimental setup.

3. Experimental Results

3.1 Focus type ion diode

In the acceleration experiment the high voltage pulsed power generator is fired at a delay time τ_d after the rise of the discharge current of the plasma gun. Figure 4(a) shows typical waveforms of the diode voltage (V_d), the diode current (I_d) and the ion current density of the accelerated beam (J_i) obtained with the focus type ion diode system. Here, the pulse power system is triggered at τ_d=9.4 μs and J_i is measured by the BIC placed on the axis at z = 55 mm downstream from the surface of the anode. As seen in the Fig.4(a), V_d rises in 100 ns and has a peak of 190 kV. On the other hand, I_d rises with V_d and have a peak of 2.2 kA at t = 120 ns and after that decreases. It is observed from Fig.4(a) that the ion beam with J_i of 27 A/cm^2 and pulse duration of 120 ns in FWHM is obtained at 160 ns after the rise of V_d. Considering the time of flight delay, the ion beam corresponding the peak of J_i seems to be accelerated around the peak of V_d. For comparison, the experimental results obtained with conventional ion diode is shown in Fig.4(b), where τ_d=12 μs. In case of conventional ion diode, the ion diode is operated at V_d=220 kV, I_d=2 kA and J_i of 13 A/cm^2 is obtained, as seen in Fig.4(b). It is evident from comparison of Fig.4(a) and (b) that by using the spherical electrode, the ion current density is enhanced by a factor of 2.

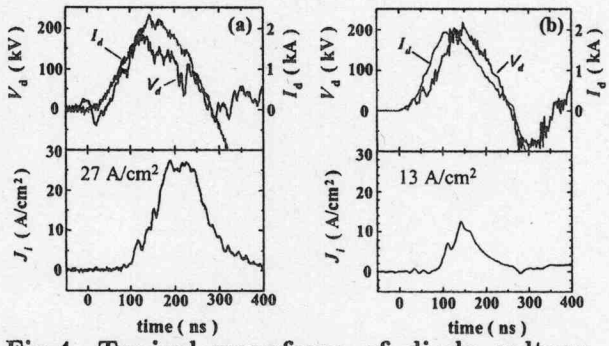

Fig.4 Typical waveform of diode voltage V_d, diode current I_d and ion current density J_i obtained with (a) Focus type MID and (b) conventional MID, respectively

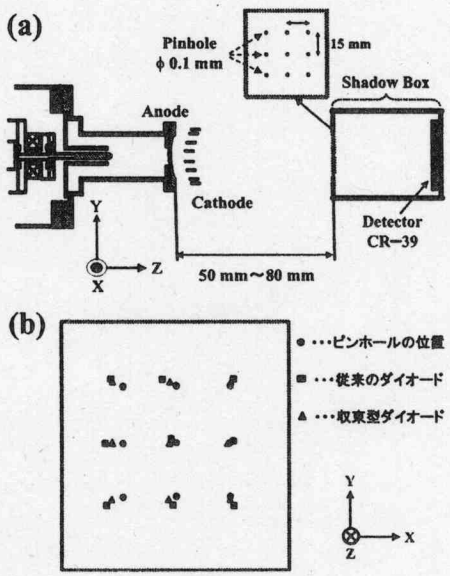

Fig.5 (a) A schematic view of shadow box setup and (b) typical pinhole image of the ion beam obtained at z = 50 mm.

Figure 5 shows an arrangement of shadow box measurement and an example of shadow box image obtained at $z = 55$ mm. As seen in Fig.5(a), the shadow box consists of a multi-pinhole plate and an ion track detecting plastic of CR-39 placed at 10 mm behind of the pinhole plate. The pinhole plate consists of 9 pinholes of diameter 0.1 mm each at the interval of 15 mm as shown in Fig.5(a) Position of each pinhole and pinhole image obtained with the conventional MID are shown in the figure as the reference. We can see from Fig.5(b) that the divergence angle of the focus type MID is small compared with that of the conventional MID. Therefore, the enhancement of the ion current density is due to the effect of geometrical focusing of the PHIB by using the spherical electrode.

3.2 Ion diode installed coaxial type Marx generator

The ion current density is enhanced by using the focus type ion diode with the spherical electrode. The ion current density, however, is not enough for the material processes. Since the step up transformer is used to magnify the pulse voltage, the diode current is limited. Thus, the coaxial type Marx generator, which can supply both high voltage and large current, has been developed and installed in the intense pulsed heavy ion diode system in order to achieve ion current density enough for the material process. Both schematic view and circuit diagram of coaxial type Marx generator are shown in Fig.6. The circuit component of the Marx generator is shown in Fig.6(b). The generator has basic characteristics of voltage 200 kV, current 15 kA and pulse duration 100 ns and is about 8 times higher output power than conventional one.

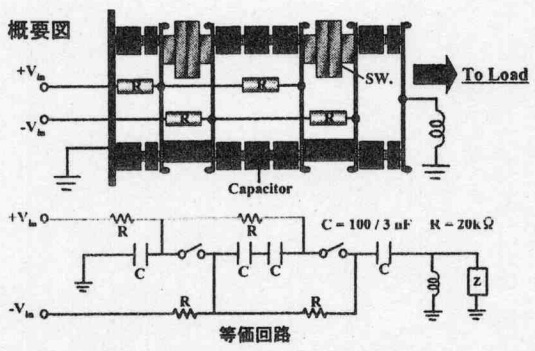

Fig.6 (a) Schematic view and (b) circuit diagram of coaxial type Marx generator.

Figure 7 shows typical waveforms of diode voltage (V_d), diode current (I_d) and the ion current density (J_i) where the delay time τ_d between the plasma gun and the pulse power system is τ_d=10 μs. Both ion diode system and measurement setup are the same as the focus type ion diode shown in Fig.3 except that the Marx generator is employed as the pulsed power generator. As seen in the Fig.7(a), V_d rises in 75 ns and has a peak of 190 kV, whereas I_d rises with V_d and have a peak of 16 kA at $t = 80$ ns and after that decreases. We can see from Fig.7(b) that the ion beam with current density of $J_i = 54$ A/cm^2 and pulse duration of 80 ns(FWHM) is obtained at 30 ns after the peak of V_d. Considering the time of flight delay, the ion beam corresponding the peak of J_i seems to be accelerated around the peak of V_d. It turns out from comparison of Fig.4 and Fig.7 that I_d increases by 8 times, whereas J_i is about 2 times as large as that of the focus type MID. Further investigations on optimal conditions are now undertaken.

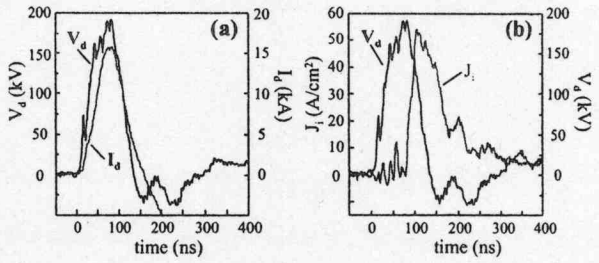

Fig.7 Typical waveforms of (a) V_d, I_d and (b) J_i.

3.3 Development of wire discharge metallic ion source

Pulsed metallic ion beams has received extensive attention for the material processes, however they cannot be obtained yet. We have developed the vacuum discharge ion source as an intense pulsed metallic ion source [11,12]. The vacuum discharge ion source, however, cannot produce the stable metallic ion beam. For the purpose of obtaining the stable ion beam we are doing experiments on the wire discharge metallic ion source.

Figure 8 shows the experimental setup to eval-

uate the characteristics of the wire discharge ion source. An aluminum wire of 30 mm length by 0.1 mm diameter is stretched between two electrodes. Electrodes are connected to a capacitor bank through a gap switch. The capacitor bank of capacitance 1 μF is charged at 30 kV. The wire is melted, evaporated and ionized by the Joule heating to produce the ion source plasma. For the measurement of the ion current density and of the spatial distribution three BIC's are placed at 150 mm apart from the wire, as shown in Fig.8. The experiment is done in the vacuum of 5×10^{-3} Pa.

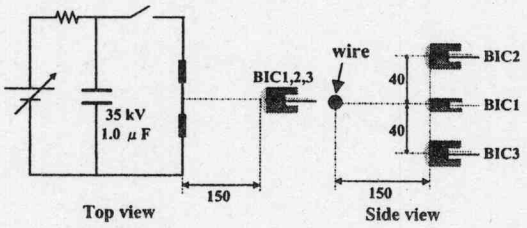

Fig.8 Experimental setup of aluminum wire discharge ion source.

Figure 9 shows the typical waveforms of discharge current (I_a) and ion current density (J_i) measured by BIC1 placed on the central axis. As seen in Fig.9, the discharge current I_a has a sinusoidal waveform of peak current 11 kA and quarter cycle 2 μs. The ion beam of the peak current density J_i=65 A/cm^2 and pulse duration of 2 μs is observed at about $\tau_p = 6.5$ μs after the rise of I_a.

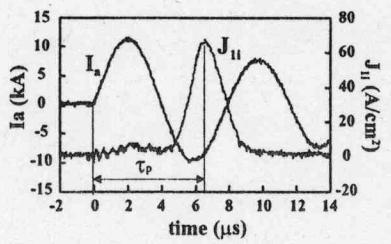

Fig.9 Typical waveforms of discharge current (I_a) and ion current density (J_i).

Figure 10 shows the dependence of the peak current density (J_{ipeak}) and the delay time (τ_p) of J_{ipeak} from the rise time of I_a. As seen in Fig.10, each J_{ipeak} measured by BIC1, 2 and 3 has a scattering. Taking the result measured by BIC1 as an example, the average value of J_{ipeak} in the 10 shots is calculated to be 67 A/cm^2, whereas the standard deviation is evaluated to be 14 A/cm^2.

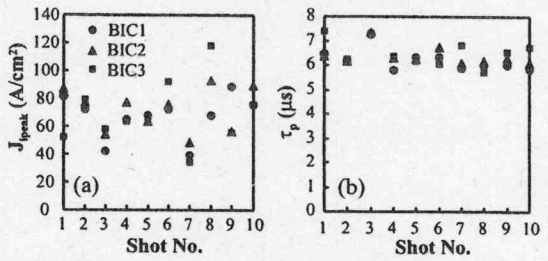

Fig.10 Dependence of (a) J_{ipeak} and (b) τ_p on shot number.

On the other hand, τ_p is relatively stable and the average value of τ_p in the 10 shots is 6.2 μs. Each average value of J_{ipeak} and τ_p and the standard deviation(SD) of J_{ipeak} are summarized in Table.1. Those values of the vacuum arc discharge ion source are also shown as the reference. We can see from Table.1 that the SD of J_i is 1 order of magnitude smaller than the vacuum arc ion source. The average current density decreases by a factor of 3 but is enough for the ion source. The experimental results also indicate that the ion beam has an almost uniform spatial distribution of the ion current density. This device is expected to be employed as the ion source for the intense pulsed metallic ion beam system.

Table 1 Experimental results

	J_i (A/cm^2)	τ_p (μs)	SD of J_i
BIC1	67	6.2	14
BIC2	72	6.4	15
BIC3	69	6.5	22
Vac. arc	181	6	161

In order to evaluate the drift velocity of the plasma by a time of flight method (TOF), two BIC's are placed at 77 and 155 mm downstream from the discharge gap, respectively. The TOF delay time between of two BIC signals is 4 μs, which gives the drift velocity of 1.96×10^4 m/s. Assuming aluminum ions it corresponds to the ion energy of 54 eV.

4. Summary

We have develop the intense pulsed heavy ion beam diode with ion current density as large as ~50 A/cm^2 in order to apply PHIB to material processes For the purpose, two approaches to the

enhancement of ion current density have been employed, i.e. the focus type ion diode and development of the coaxial Marx generator. When the plasma produced by the plasma gun is injected into the acceleration gap of the focus type ion diode, the ion diode is successfully operated at diode voltage $V_d \approx 190$ kV, diode current $I_d \approx 2.2$ kA and pulse duration ≈ 150 ns (FWHM). The ion beam of ion current density $J_i = 27$ A/cm^2 is obtained at 55 mm downstream from the anode. By using the spherical electrode for focusing ion beam, the ion current density is enhanced by a factor of 2. When the coaxial Marx generator is employed as the power supply for the ion diode, the ion diode is operated at diode voltage $V_d \approx 200$ kV, diode current $I_d \approx 16$ kA, pulse duration ≈ 100 ns and the ion beam of $J_i = 54$ A/cm^2 is obtained. We find that I_d and J_i increases by about 8 and 2 times compared to those of the focus type MID, respectively. We are currently investigating the optimal conditions to generate the ion beam with the expected ion current density.

We are developing the wire discharge metallic ion source in order to produce the intense pulsed metallic ion beam. The characteristics of the ion source are evaluated and the source plasma of current density ~ 70 A/cm^2 with the plasma drift velocity 1.96×10^4 m/s is obtained. The ion source is expected to be applied to the intense pulsed metallic ion beam system. There seems to be some room for making improvements including the electrode structure.

Acknowledgement

This work is supported in part by the Grant-in-Aid for Scientific Research from the Ministry of Education, Science, Sports and Culture, Japan.

参考文献

[1] J.P. VanDevender and D.L. Cook, Science **232**, 831 (1986).

[2] K. Yatsui, X. D. Kang, T. Sonegawa, T. Matsuoka, K. Masugata, Y. Shimotori, T. Satoh *et al.*, Phy. Plasma **1**, 1730 (1994).

[3] H.A. Davis, G.E. Remnev, R.W. Stinnett and K. Yatsui, Mater. Res. Bull. **21**, 58 (1996).

[4] V.A. Shulov, N.A. Nochovnaya, Mater. Sci. Eng. **A243**, 290 (1998).

[5] H. Akamatsu, Y. Tanihara, T. Ikeda, K. Azuma, E. Fujiwara and M. Yatsuzuka, Jpn. J. Appl. Phys. **40**, 1083 (2001).

[6] K. Masugata, Y. Shimizu, Y. Fujioka, I. Kitamura, H. Tanoue and K. Arai, Nucl. Instrum. & Methods in Phys. Res. A **535**, 614 (2004).

[7] C.A. Meli, K.S. Grabowski, D.D. Hinshelwood, S.J. Stephanakis, D.J. Rej and W.J. Waganaar, J. Vac. Sci. Technol. **A13**, 1182 (1995).

[8] K. Masugata, *et al.*, Proc. 25th Int. Power Modulator Sympsoium, 2002 (Hollywood, CA, USA, 2002) pp.552-555.

[9] E. Chishiro, A. Matsuyama, K. Masugata and K. Yatsui, Jpn. J. Appl. Phys. **35**, 2350 (1996).

[10] K. Masugata, H. Okuda, K. Yatsui and T. Tazima, J. Appl. Phys. **80**, 4813 (1996).

[11] K. Masugata, R. Tejima, M. Higashiyama, J. Kawai, I. Kitamura, H. Tanoue and K. Arai, Plasma Device and Operations **13**, 57 (2005).

[12] I. Brown, Rev. Sci. Instrum. **65**, 3061 (1994).

INVESTIGATION OF THE PLASMA DYNAMICSAND EMISSION OF ION BEAMS AND NEUTRON WITHIN THE PLASMA FOCUS DEVICE

H.R.Yousefi, Y.Ejiri, H.Ito and K.Masugata

Department of Electric and Electronic System Engineering, University of Toyama, 3190 Gofuku, Toyama 930-8555, Japan

Abstract

This paper reports some of the results that are aimed to investigate the neutron emission from the middle energy Mather-type plasma focus. Multiple compression were investigated and it seems that multiple compression regimes is occurred at low pressure and single compression is appeared at higher pressure where is the favorable to neutron production, and also accompany with these multiple compression, more than two neutron pulse and ions were detected, this implies to different kind of acceleration mechanisms. Multiple compression is proposed has a correlation with m=0 instability.

Key word: Plasma focus; Neutron; x-ray; Ion beams; m=0 instability.

Introduction

In spite of many efforts in the plasma focus devices with different energy there are some unclear mechanisms yet that they might be good response to unresolved question. For example the multiple compression mechanism is still remained unclear. Different kind of acceleration mechanisms for charge particle were identified[1, 2].During the compression phase the rapid local changes in the magnetic flux is the main case to produce the high electric field.[3].also this phenomena can be occurred during the m=0 instability developments. Two plasma focus regimes were identified operating in deuterium; one is the single- compression regime corresponding to a single-compression of the pinch, the other one is the multiple compression regimes associated with two or more compressions of the focused column [4]. Multiple compression peaks on the voltage probe signal were reported by R.S.Rawat [5].Also they reported that there is no direct relationship between the soft x-ray yield and compression peaks. In this paper [5] not found any explanation for multiple compression mechanism. Observation of Multiple peak spectra of ions and electrons reported just by two groups respectively [6] and [7].Two neutron pulses were observed and reported on the POSEIDON and PF1000 Devices by

Jager and M.Scholz in Germany and Poland respectively. The first pulse occurs in the quiet phase with 0 -150 ns life time. The second neutron pulse in the both case is more intense than the first and lasts for 150 -300 ns. Rossel and choi studied the neutron emission in the medium energy (28 kJ) plasma focus with admixture gas of neon and krypton, two neutron emission periods were reported, the first period occurs when the tight plasma column is being formed, well before the disruption of the plasma column, and lasts for less than 50 ns [8].The first aim of this work was to investigate of the multiple pinch mechanism and relation with the neutron production and the other main was to investigate of the ion acceleration mechanism and neutron production.

Experiments

Our Mather-type plasma focus is energized by a capacitor bank of 44.8 μF/30 kV [9]. In this experiment are used 242mm anode length and 230mm cathode length. The outer electrode (cathode) was composed of 24 copper rods. The plasma focus chamber was evacuated up to 4 $x10^{-5}$ mbar, using a rotary and diffusion pump. To reduce impurity effects, after five shots the previous gas was purged and the chamber filled with fresh deuterium. A scintillator – photomultiplier system was used to measurement the time- resolved hard X-ray, neutron. This diagnostic was placed 10 m away from the anode head. Ion beams signals detected by baise ion collector (BIC) to synchronization and determination of a relation between the hard x-ray and neutron production.

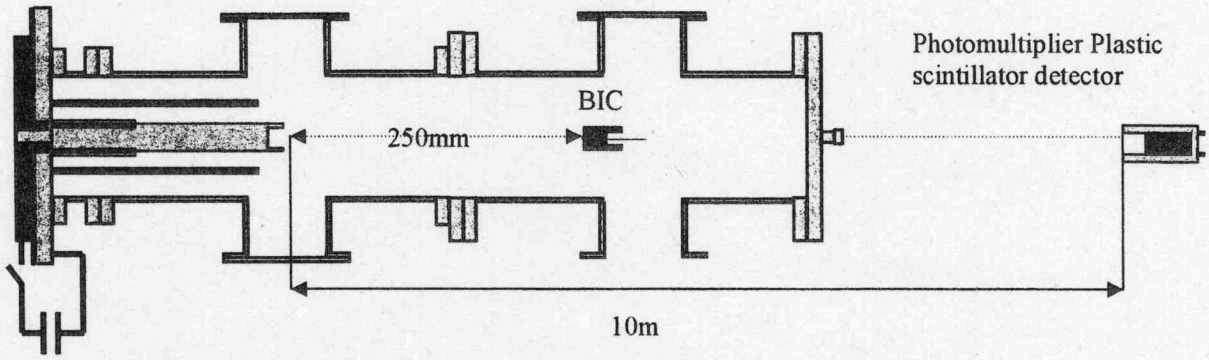

Schematic Diagram of Plasma Focus Device

Results and Discussion

The current signals show that for low pressure there are multiple compressions or pinch. From the fig. 1 the multiple compressions are found within the pressure range of 2-8.0 mbar, beyond this range single compression is observed. From 2 mbar the numbers of current oscillations where we are calling multiple compressions, and also height of current drop is increase till 5 mbar. After 8 mbar these numbers will be decreased and toward the 13 mbar a single compression is observed.

Figure 1 and 2 present, from 2 mbar to 5mbar multiple compression regimes associated with more than two compressions peak and from 6 to 9 mbar two peaks but from 10 till 13 mbar just single compressions can be observed. Another important point to note that through the comparison of fig. 3a and 3b is that during the multiple compression regimes in spite of many compression peaks, neutron intensity is lower than single compression regime and there is no direct relation between the neutron and the compression peaks as the number of peaks is maximum at 2mbar pressure, whereas the neutron intensity is rather low among all the pressures. It seems that at low pressure where the pressure is optimum for soft x-ray, multiple compression can be appears and this regime is favorable for soft x-ray emission. As the pressure increase multiple compressions is decreased and greatest neutron peak is appeared. It has been noticed that during the multiple compression peaks, hard x-ray emission is increased. Multiple pinches are might be due to the multiple instability.

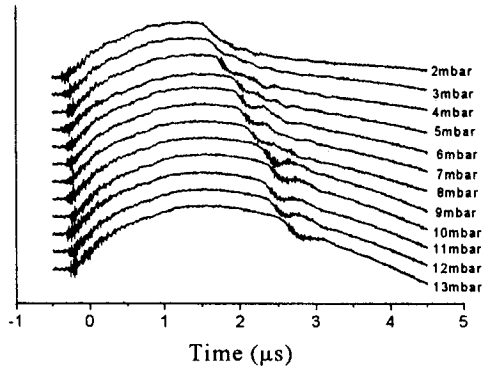

Figure 1.Current signals at different pressure

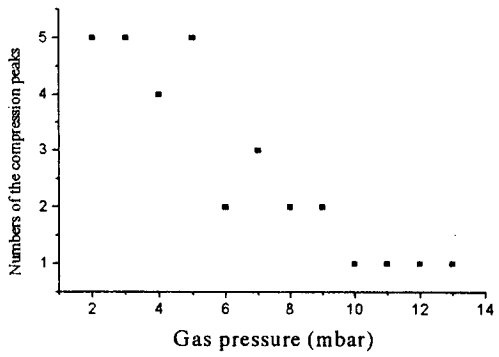

Figure2. Average number of compression peaks at different pressure

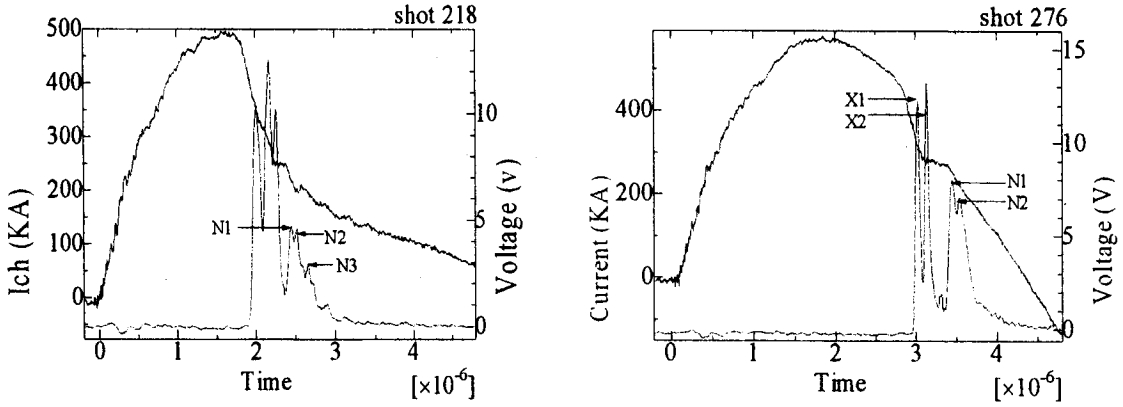

a b

Figure (3a, b) show current signal, hard x-rays and neutron pulses at 2mbar and 13 mbar respectively

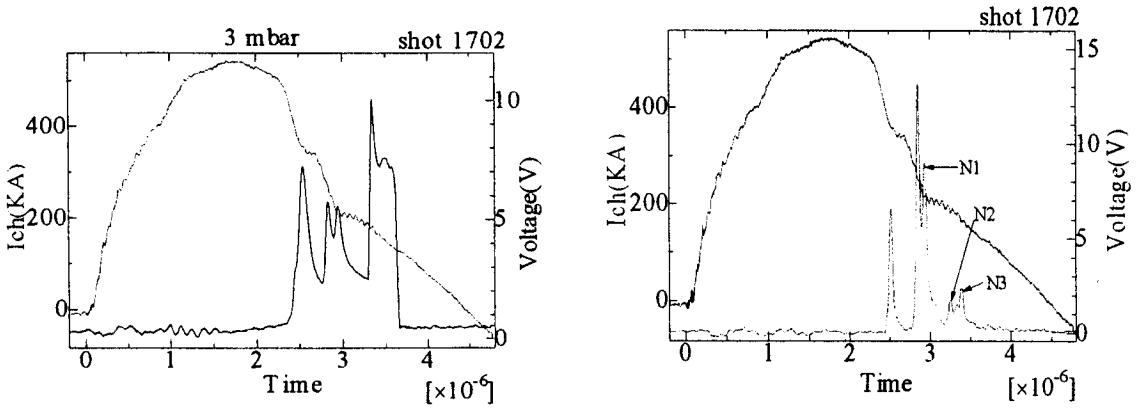

a b

Figure (4a) show, current signal, ion beams .Figure (4 b) show, current signal, hard x-rays and neutron pulses

In the figure 3a, at low pressure multiple, pinches can be observed also during these pinches three neutron pulses are detected, but at high pressure just one pinch and two neutron pulses detected. With compare, fig.3a and b, single compression or stable mode is occurred at high pressure where is the neutron intensity is grater. Figure 4a presents the ion beams pulses which were detected by BIC (Baise Ion Collector) and Figure 4b presents the hard x-ray and neutron pulses which were recorded by the scintillation probe. From the fig. 4a and b with the compare the ion emission and hard x-ray emission time it is almost same with some ns error. It is indicated that ion and electron beams are accelerated by the same electric field. For the first ion, till third ion there is this synchronization but the forth ion is

not coincide with any pinch or hard x-ray. We can assume that there is another acceleration mechanism regardless of the m=0 instability. First hard x-ray is coinciding with first pinch. Time Difference between the first hard x-ray and first neutron pulses is about 430 ns therefore from the neutron time of flight for 10 meter it is evaluated that the neutron energy about 2.45 Mev. For the second hard x-ray and second neutron this is 410ns it means that second neutron energy is more. For the second pinch event, just neutron pulse appeared. Last ion pulse appeared with different time as pinch time, it seems, ion emission time is connected to another acceleration mechanism. The observation m=0 instability, without neutron emission [10] in spite of author suggestion indicated that electric fields which were occurred by m=0 instability, have not suffusion energy to accelerate the ion or produce the neutron. The proposed mechanism for the multiple neutrons or multiple compressions is m=0 instability. This instability can appear at low pressure whereas toward the high pressure a stable phase is occurred in which there are single compression and highest intensity of neutron.

Acknowledgments

First author would like to thank of the University of Toyama and gratefully acknowledges financial support from the Ministry of Education, Culture, Sports, Science and technology.

References

[1] Mather J W 1971 Methodes of Experiments Physics ed H Griem and R Loverberg vol **9B**,p 187

[2] Trubnikov B A 1986 Sov.J.Plasma Phys.**12** 490

[3] Peacock N J, Hobby M G and Morgan P D 1971 Proc. 4th Int.Conf. on Plasma Physics and Controlled Nuclear Fusion Research (Madison) vol **1**, p 537

[4] M.S.Rafique and et al., 26th EPS Conf.on Contr.Fusion and Plasma Physics

[5] R.S.Rawat and et al Plasma Sources Sci.Technol.**13**(2004)569-575

[6] Belyaeva I F 1980 Nucl. Fusion **8** 1037

[7] A.patran ,Plasma source Sci.Technol.**14**(2005)549-560

[8] A. Rossel R and P. Choi 1994 AIP Conf.Proc.**299** 261

[9] K Takao, T Honda, I. Kitamura and K. Masugata, Plasma Sources Sci.Technol.**12** (2003)407-411

[10] Toshikazu Yamamoto, Japanese journal of applied physics, vol.**24**, No.3, March, 1985 PP.324-327

SIMULATION OF MULTICHANNEL ARC GAP

Seizo Furuya, Shintaro Suzuki, Ryo Ogata, Saburo Takano and Juichi Irisawa

Nagaoka University of Technology, 1603-1 Kamitomioka, Nagaoka, 940-2188, Japan

ABSTRACT

A multichannel arc gap is a switch which produces a large number of arc channels in parallel. We have been investigating the characteristics of the self-breakdown-type multichannel arc gap experimentally. In this report, we examine the relation between the breakdown time and the number of arc channels by means of experiment and simulation. Using the experimental data of single gap, we ran the simulation of multichannel gap and compared them with the experimental results of multichannel gap. The experiments and simulations show similar tendency, however, the number of arc channels in the simulations is larger than that in the experiments.

1. Introduction

A multichannel arc gap is a switch which produces a large number of arc channels in parallel. Compared to a single gap, a multichannel arc gap has a lower switching inductance and electrode erosion rate, which is superior due to its fast rise time and long lifetime. Therefore, a multichannel arc gap is frequently used as a switch for the pulsed power technology. We have been investigating the characteristics of the self-breakdown-type multichannel arc gap experimentally[1]. In this report, we examine the relation between the breakdown time and the number of arc channels by means of experiment and simulation.

2. Experimental Setup

Figure 1 shows the geometry of the multichannel arc gap. The gap comprises 12 steel needle electrodes and a brass rod electrode of 18 mm in diameter. The rod electrode is grounded, and positive or negative voltage pulses are applied to the needle electrodes. The rectangular voltage pulses applied to the gap are generated by a 140-cm-long coaxial-type ferrite sharpener[2,3]. The ferrite sharpener can produce a voltage pulse which has a fast rise time due to its nonlinear effect. The experiments are carried out in air at 1 atm. The number of arc channels is detected by a Hitachi DVD video camera (DZ-MV380). Fifty shots under each experimental condition are performed and the data of the number of arc channels is handled by taking the mean. Voltages are measured by a Tektronix high-voltage probe (P6015A) and a Hewlett-Packard digital oscilloscope (HP54510A).

UV light is irradiated to the gap to generate the initial electrons. UV light source (Hamamatsu Photonics L937-02) is set parallel to the gap. The

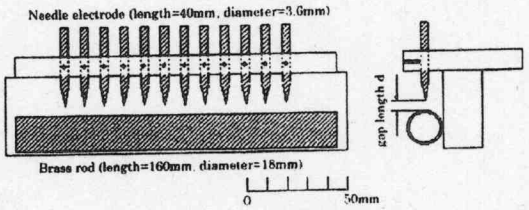

Fig.1 Geometry of the multichannel arc gap

distance between the source and the gap is 100 mm. To confirm the effectiveness of UV irradiation, the preliminary experiments are carried out. Figure 2 shows the discharge voltage waveforms (a) without UV irradiation and (b) with UV. Fifty shots are superimposed in each figure. The geometry of gap is sphere-sphere and the gap length is 3 mm. The charging voltage of an energy storage capacitor is +15 kV. As shown in the figures, the jitter of breakdown time decreases as UV light is irradiated.

3. Method of simulation

Figure 3 shows the equivalent circuit of experimental system. It is composed of an energy storage capacitor, a transmission line and the multichannel arc gap. In the experiments there is a ferrite sharpener between the transmission line and gap, but it is neglected in the simulations.

It is well-known that a breakdown time comprises a statistical time lag and formative time lag, as shown in Fig. 4. Irradiating sufficient UV light makes a statistical time lag zero. First, the breakdown times of single gap are measured and their jitter are simulated using normal-distribution random numbers

by Box-Muller method. Then the simulation of multichannel gap is performed and we compare them with the experimental results of multichannel gap. We assume that each gap can be bridged until the voltage between the gap decreases to V_{dc}.

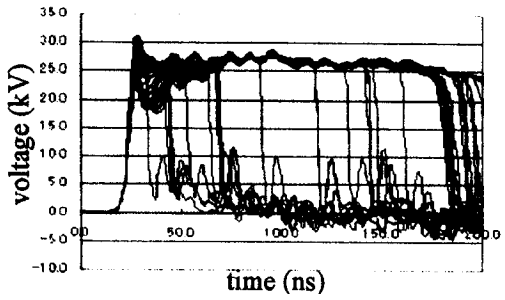

(a) without UV irradiation

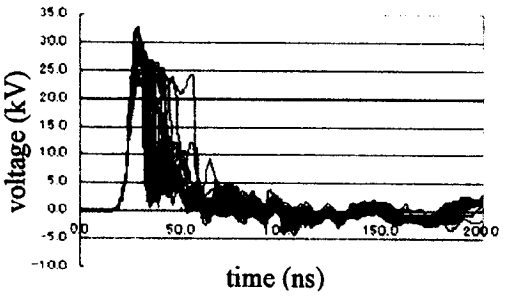

(b) with UV irradiation

Fig.2 Discharge voltage waveforms with and without UV irradiation

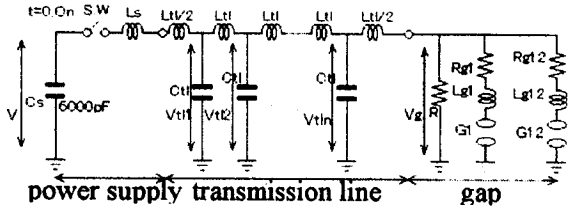

Fig.3 Equivalent circuit

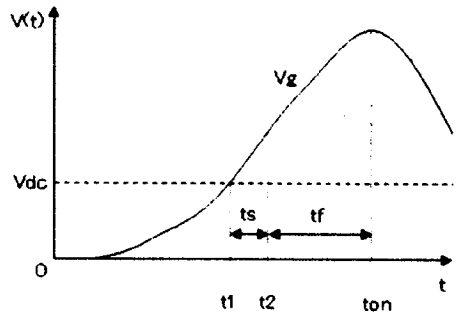

Fig.4 Explanation of statistical and formative time lags

4. Results and Discussion

4.1 Experimental results of single gap

The energy storage capacitor is charged to ±10, 15 and 20 kV and the gap length is 1, 3 and 5 mm. Fifty shots under each experimental condition are performed and the average and jitter of breakdown time are measured. Figure 5 shows the example of discharge voltage waveform (a) without UV irradiation and (b) with UV. The charging voltage is +15 kV and the gap length is 1 mm. It is obvious that the jitter of breakdown time with UV irradiation is shorter than that without UV because UV irradiation makes statistical time lag zero. Also, in the case of gap length of 1 mm, the breakdown voltage with UV is smaller than that without UV. It is not seen in the cases of 3 mm and 5 mm.

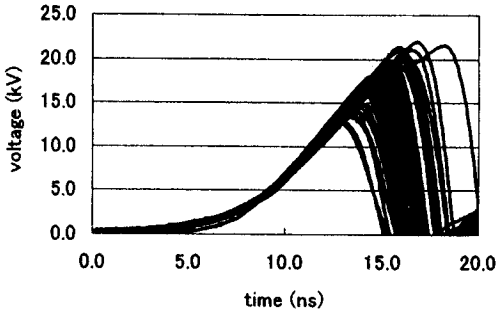

(a) without UV irradiation

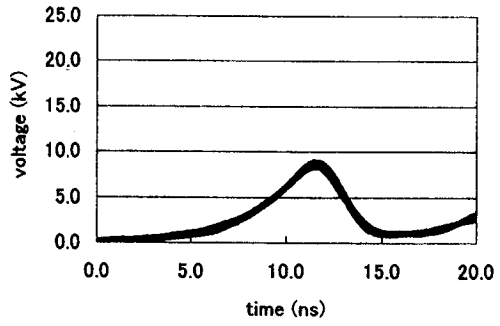

(b) with UV irradiation

Fig.5 Example of discharge voltage waveform

Figure 6 shows the frequency distribution of breakdown time under different experimental conditions. The charging voltage of both (a) and (b) is +10 kV. The gap length of (a) is 1 mm and that of (b) 5 mm. As shown in the figures, the effect of UV irradiation is significant when the gap length is short.

4.2 Experimental and simulation results of multichannel gap

The experimental and simulation results of multichannel gap are summarized in Fig.7. The

energy storage capacitor is charged to +10, 15 and 20 kV and the gap length is 1, 3 and 5 mm. The polarity of voltage pulses is positive. In both experiments and simulations 50 shots under each condition are performed and the data of the number of arc channels is handled by taking the mean. The experiments and simulations show similar tendency as follows: The number of channels increases with the charging voltage and decreases with increasing gap length. However, the number of arc channels in the simulations is larger than that in the experiments. The tendencies of these characteristics are also observed for negative polarity.

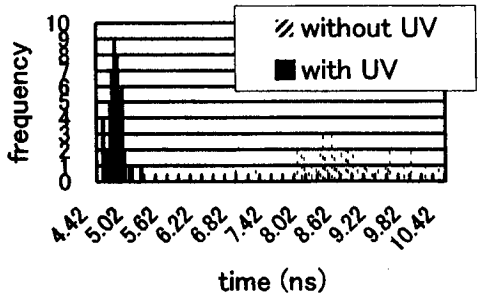

(a) +10 kV, 1 mm

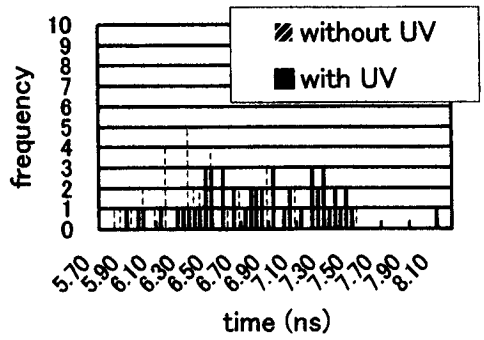

(b) +10 kV, 5 mm

Fig.6 Frequency distribution of breakdown time

5. Conclusions

Using the experimental data of single gap, we ran the simulation of multichannel arc gap and compared them with the experimental results of multichannel gap. The experiments and simulations show similar tendency, however, the number of arc channels in the simulations is larger than that in the experiments. We plan to run the simulation using the experimental data of breakdown time of multichannel gap.

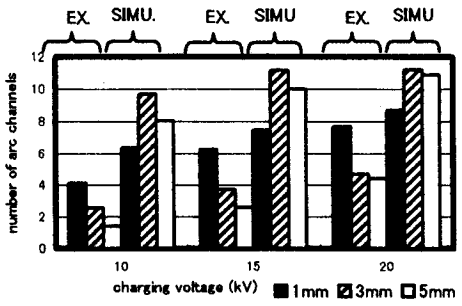

(a) without UV irradiation

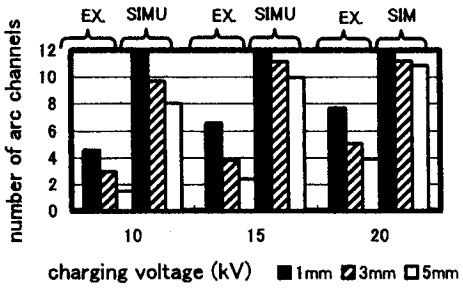

(b) with UV irradiation

Fig.7 Number of channels in experiments and simulations

References

1) Seizo FURUYA, Yoshiya WATANABE, Takeshi YOSHIKAWA, Saburo TAKANO and Juichi IRISAWA: Characteristics of Multichannel Arc Gap, JJAP 40 (2001) 987
2) Seizo FURUYA, Haruo MATSUMOTO, Hitoshi FUKUDA, Takao OHBOSHI, Saburo TAKANO and Juichi IRISAWA: Simulation of Nonlinear Coaxial Line Using Ferrite Beads, JJAP 41 (2002) 6536
3) Seizo FURUYA, Katsuaki TACHI, Saburo TAKANO and Juichi IRISAWA: Surge Impedance of Nonlinear Coaxial Line Using Ferrite Beads, JJAP 43 (2004) 1131

Generation of Microplasmas with a Liquid materials And Their Characteristics

N.Shirai*, Y.Onaka, N.Nakagawara, S.Ibuka, K.Yasuoka, and S.Ishii

Department of Electrical and Electronic Engineering
Tokyo Institute of Technology
2-12-1-S3-9 O-okayama, Meguro-ku, Tokyo, Japan

Abstract

An ethanol droplet of 300μm in diameter is used to create a dense microplasma by pulsed discharge. When the droplet came into the space between miniature electrodes to which a dc high voltage was applied, the pulsed discharge took place simultaneously. Vaporization and dissociation of ethanol were confirmed in the discharge because the atomic line of hydrogen was observed in optical emission spectroscopy. Taylor cone is formed on the anode surface where the remaining ethanol is dragged to the cathode by electrostatic force after the discharge. We utilize the filament formed at the tip of the Taylor cone as an initial state of liquid for generating microplasmas.

I. Introduction

Microplasmas are small-scale plasmas with the size of hundreds microns. The plasmas will be formed in the required position and with the amount of only necessary volume. By making use of the feature of microplasmas as a miniaturized plasma source, there are a variety of applications such as plasma display panels (PDPs), microelectromechanical systems (MEMS), short wavelength light sources and micro-reactors in chemistry. Many methods to form microplasmas have been proposed and examined experimentally. The discharges are usually operated in atmospheric pressure to obtain high-density plasma.

The methods of creating the microplasmas are classified roughly into three modes as follows. Microplasma is generated at a sharp tip of thin electrode due to high electric fields. We call it as an energy-concentrated mode. The plasmas are formed also in micro-cells or capillaries to limit the plasma volume. The PDP discharge is an example of a space-limited mode. Dielectric barrier discharges are commonly used to make such plasmas. Since the ratio of the surface area for the plasma volume is extensively larger in comparison with that of the conventional plasmas, the discharge characteristics are affected by the surface of the micro-cells and the capillaries. Electron emission from the electrodes and the dielectric surface plays an important role for the discharge development in the small space. Electrons and ions easily recombine at the surface of walls, which causes the particle loss. Fast electrical energy input is required to form the microplasma in the space-limited mode because energy and particle losses develop in a very short time. To overcome these drawbacks, we eliminate the wall to limit plasma volume and use a microdrop or a powder particle to create dense microplasmas by pulsed electrical discharges. We name the method a mass-limited mode[1][2].

In this paper we propose to use a single droplet or a liquid filament as an initial matter to form the microplasma. Because mass densities of liquids are higher than those of gases and the liquids change their volume-shape more freely than solids, it is expected that dense microplasmas with a variety of shapes are generated easily. However, most liquids

are in molecular state, processes developing from their initial state to plasma are more complicated than those for gases. Chemical reactions often develop in the liquid phase with heat. In microplasmas with liquids, additional energy can be supplied to the reactions through electrical discharges. Non-thermal reactions by high energy electrons are also expected. We discuss discharge characteristics of liquid microplasmas and how to make the initial micro-structure of liquids.

II. Experimental

Fig.1 is the experimental set up for the discharge using ethanol droplets which is supplied by a micro dispenser (MJ-020 by MECT, Ltd.) between the electrodes. The spherical droplet with a diameter of 300μm and a volume of 10nl was dropped into the discharge space from the dispenser head. The electrical discharge develops simultaneously when the droplet passes between the miniature electrodes in which DC voltage is applied. The electrode system used is either a needle-to-needle one or a sphere-to-sphere one. The needle electrodes are made of stainless steel with a curvature radius of 40μm and the spherical electrodes are made of tungsten-carbide of 2mm in diameter. The pulsed discharge current is supplied by a capacitor connected to the electrodes in parallel. The light emitted from the discharge was observed with a PIN photodiode (DET200 by Thorlab Ltd.) and was analyzed by a multi-channel optical spectrometer (EPP2000C by Stellar Net Ltd.). The temporal and spatial behavior of the droplet discharge was observed with a high-speed video camera (FASTCOM -512PCI by Photoron Ltd.). Early stage of the discharge was recorded with a fast ICCD camera (DH734-18U-03 by Andor technology Ltd.)

Fig.2 is the experimental set up for the discharge of ethanol filament which is created by electrostatic force between electrodes. A dc power supply was used for the electrostatic force creating liquid filament. A sphere-to-plate electrode system was employed. The spherical electrode is made of tungsten-carbide of 1-3mm in diameter. Electrode diameters and applied voltages affected the created shape of ethanol filament. When the liquid filament was created, a capacitor discharge circuit was switched on. The typical chargeing voltage is 5kV.

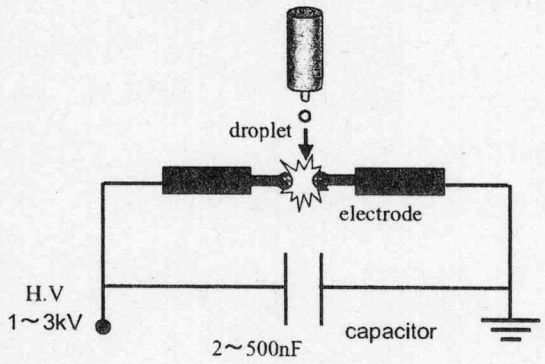

Fig.1 experimental set up for the discharge of ethanol droplet

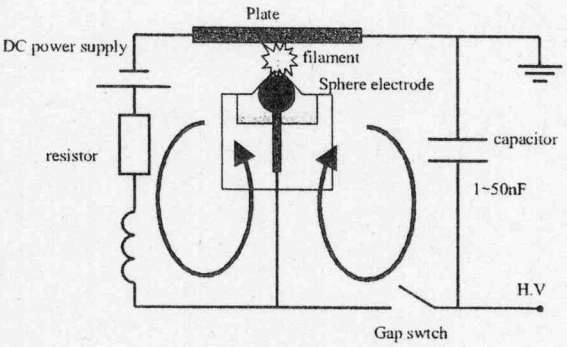

Fig.2 experimental set up for the discharge of ethanol filament

III. Results and Discussion

The ethanol-droplet discharges are basically pulsed ones. The electrodes for the discharge work also as a closing switch in the capacitor discharge circuit. Fast pulsed discharges are possible because no switching device is necessary. One does not have to use expensive pulsed generators with an extremely low residual inductance. The discharge energy wad varied from 10mJ to 1J by changing capacitance and charging voltage. The binding energy of the ethanol droplet is approximately 100mJ. Therefore ionization and heating energy are not enough to generate ethanol plasma. Fig.3 shows the voltage and current waveforms recorded in the discharge with a capacitor of 500nF charged to 2kV and temporal evolution of the microplasma taken with the fast ICCD camera.

The stored energy in the capacitor is 1J. In the first frame, intense light appears at the surface of the ethanol droplet. Bright areas between the electrodes expand during the discharge.

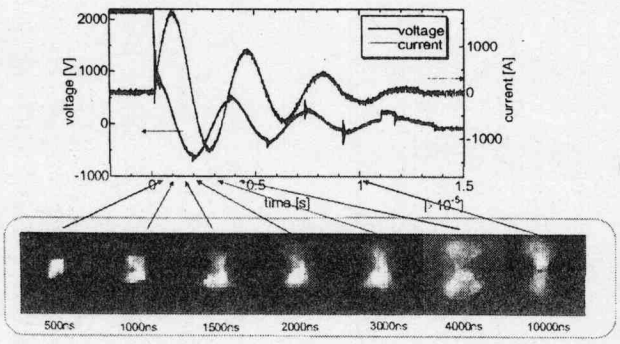

Fig.3. Current and voltage waveforms of the ethanol discharges and temporal evolution of the microplasmas.

Fig.4 is time-integrated optical emission spectra of the discharges. Vaporization and dissociation of the ethanol droplet took place in the discharge because the hydrogen atomic lines were observed as shown in fig.4. When the capacitor energy is increased the intensity of H_α:656.28nm line increases. The ratio of the intensity of H_α line to that of nitrogen atomic line:500.1nm also increases, because dissociation of ethanol is enhanced.

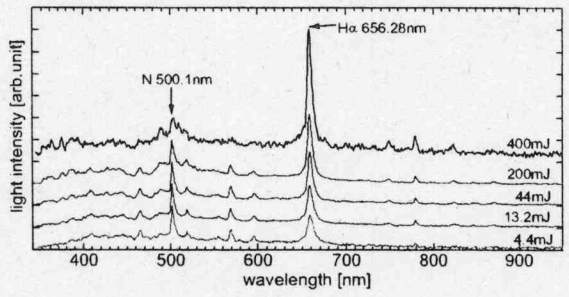

Fig.4 Time integrated optical emission spectra of ethanol droplet discharge

Fig.5 shows snapshots of the discharge taken by the ICCD camera with a narrow band interference filter that transmits the light of wavelength near H_α line: 650 nm. The exposure time is 5ns. Intense light appears at the surface of the ethanol droplet. Photographs in fig.6 are taken with the interference filter of the center wavelength near nitrogen line: 500 nm. The distribution of light emission for nitrogen differs from that of hydrogen shown in Fig.5.

Fig.7 shows the temporal behavior of the discharge including current and spectral lines. The peak of nitrogen line appears immediately after the current start to rise. The maximum of H_α line intensity delays by 1 μs from that of the nitrogen line. The results mean that the discharge appears initially near the surface of the droplet, and then discharge develops into the interior of the droplet.

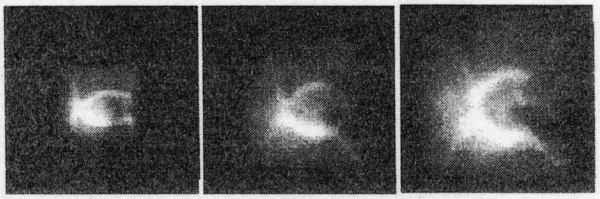

500ns 1000ns 1500ns

Fig.5.Snap-shot of droplet discharge using interference filter (650nm).

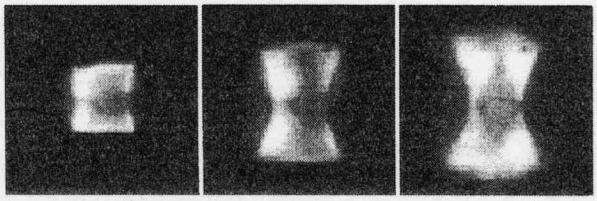

500ns 1000ns 1500ns

Fig.6.Snap-shot of droplet discharge using interference filter (500nm).

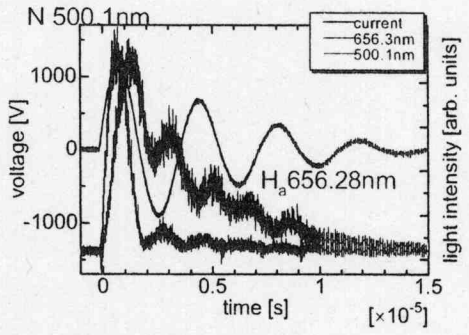

Fig.7. Temporal change in nitrogen and hydrogen lines.

To examine materials produced after the micro discharge of ethanol droplet, detecting tubes of hydrogen were used. After ten to twenty discharges in a closed camber, the detecting tube indicates the

existence of hydrogen as shown in fig.8. Fig. 9 shows that Hydrogen generation increases with increasing the number of discharges. Because chemical bonds of ethanol molecules are easily cut during the discharges, hydrogen gas and various hydrocarbons will be created. Chemical reactions taking place in the discharge are useful for various applications. However, these results are rather qualitative. We are going to analyze the materials using a mass spectrometer.

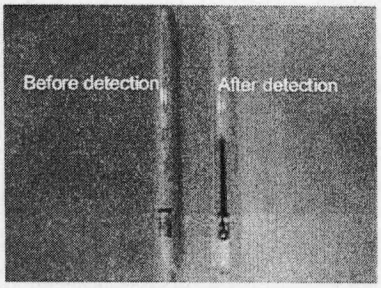

Fig.8. Reaction of hydrogen detecting tube by discharge of ethanol droplet.

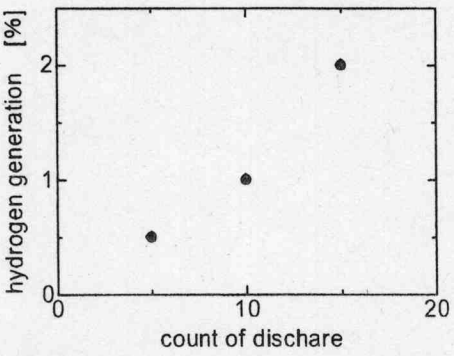

Fig.9. Ratio of hydrogen generation to count of discharge.

A small amount of ethanol was left on the surface of the electrode after the discharge. The ethanol on the anode was dragged to the cathode by electrostatic force, which transformed the shape of ethanol into conical one, that is called Taylor cone. At the tip of the cone, ethanol filament is grows toward the anode. The structure is affected by electrode separation, electrode configuration, and applied voltage [3][4] We propose a new scheme to generate dense microplasma by pulsed discharge with the liquid filament that is created by electrostatic force between electrodes in air [5].

The height of Taylor corn and the length of filament are controlled by changing the applied voltage, if the voltage is lower than that for dielectric breakdown of ethanol and is higher than that for the filament generation. Fig.10 shows the change in the formation of Taylor corn according to the applied voltage. The sphere electrode is 2mm in diameter. When the electrode diameter is smaller, the filament is generated with a lower voltage because the electric field is concentrated at the tip of the electrode. The length of filament becomes longer if the applied voltage is increased as shown in Fig.11. On the other hand, the height of Taylor corn becomes lower.

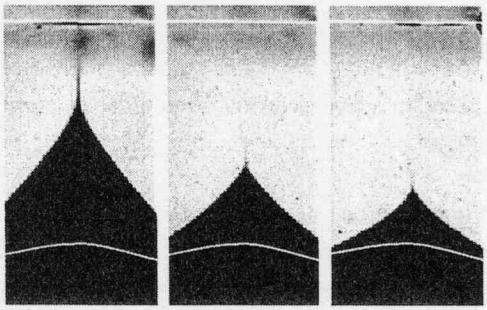

Fig.10. Generation of Taylor cone and filament.

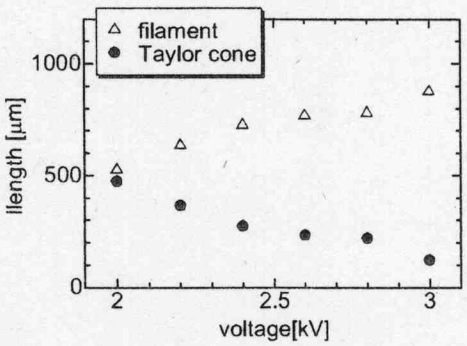

Fig.11. Difference of length of Taylor cone and filament according to applied voltage.

Time resolved behavior of the liquid filament discharges in air powered by capacitor discharges of 3nF and 50nF is shown in Fig.12 and Fig.13. Photographs were taken using the ICCD camera with the exposure time of 5ns. The discharges initiated at the surface of the ethanol filament. Current density is high because the discharge current has to flow in the thin filament. By changing the length of filament, we

can control the size of plasma. When the discharge current is increased to hundreds kA, fiber pinches with liquid filament of tens μm in diameter will be possible. The microplasmas with liquid filament have a variety of applications, because the plasma size and density can be changed in a wide range.

0ns 30ns 70ns 110ns

Fig12. Snap-shots of the liquid filament discharges with a 3nF capacitor taken by an ICCD camera.

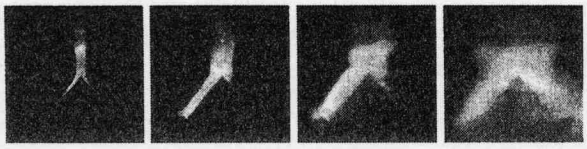

30ns 80ns 200ns 500ns

Fig13. Snap-shots of the liquid filament discharges with a 50nF capacitor taken by an ICCD camera.

IV. Conclusion

Microplasmas with the ethanol droplet and filament are generated by electrical discharge in air. The generation of liquid-microplasma has a number of features that are specific to the microplasma. In the droplet discharge, pulsed discharges are obtained without high-voltage pulse generators, because the discharge starts as soon as the droplet comes into between the electrodes. Hydrogen molecules were detected after the discharge in the closed chamber using the detecting tube.

The formation of Taylor cone is useful as a viewpoint of microplasma generation. We utilized the filament observed at the tip of the Taylor cone as an initial state of liquid microplasma. The height of Taylor corn and the length of filament are controlled by changing the applied voltage. In the previous researches on fiber pinch, solid fibers were commonly used. However, one can conduct liquid filament pinch experiments using our scheme.

Acknowledgements

This work was supported by a Grant-in-Aid for Scientific Research from the Ministry of Education, Culture, Sports, Science and Technology: Scientific Research on Priority Areas.

References

[1] N. Shirai, Y. Onaka, S. Ibuka, K yasuoka, S Ishii: The paper of Technical Meeting on Plasma Science and Technology, IEEE Japan (2004) PST-04-29

[2] S. Hamada, M. Kanemaru, S. Ibuka, K yasuoka, S Ishii: The paper of Technical Meeting on Plasma Science and Technology, IEEE Japan (2005) PST-05-98

[3] R. Juraschek, F.W. Rollgen: International Journal of Mass Spectrometry 177, (1998) p.1-15

[4] A. L. Yarin, S. Koombhongse, D. H. Renekera: Journal Of applied Physics v.90, n9, (2001) p4836-4846.

[5] Y. Onaka, N Shirai, N Nakagawara, S. Ibuka, K Yasuoka, S Ihsii: The paper of Technical Meeting on Plasma Science and Technology, IEEE Japan (2005) PST-05-99

Plasma spraying by electromagnetic acceleration using a copper particle

S.Hamada*, M.Kanemaru, S.Ibuka, K.Yasuoka, and S.Ishii

Department of Electrical and Electronic Engineering
Tokyo Institute of Technology
2-12-1 O-okayama, Meguro-ku, Tokyo, Japan

ABSTRACT

Microplasma was generated with a copper powder particle of 100μm in diameter. We propose a novel spraying method using the copper microplasma accelerated along miniature rail-electrodes electromagnetically by Lorentz force. We used a crowbar diode in the discharge circuit to obtain the discharge current without ringing for establishing efficient acceleration process. The velocity of microplasma is related to the discharge current, the pulse width and the inductance of the rail electrode per unit length. The electromagnetic acceleration of copper plasma was observed with a high-speed video camera, a streak camera, and an ICCD camera. The average velocity along the rail-electrodes was approximately 900m/s during 3μs after the initiation of the discharge. When the copper microplasma sprayed on a substrate, copper thin film was formed on the surface.

Keyword: copper, particle, plasma spraying, microplasma, electromagnetic acceleration

I .Introduction

Microplasma is utilized in a variety of applications such as microelectromechanical systems (MEMS), plasma display panels (PDPs), short wavelength light sources, and micro-reactors in chemistry. We have studied the dense microplasma generated with a metal powder particle with a diameter of 100-200μm, which is heated and vaporized by Joule heating.[1] Fiber pinches and exploding wires by pulsed high currents are well known as the plasma generated from solid materials.[2-3] They are powered in the range of 10-100kV and 1kJ-1MJ. However, the required energy to power the powder particle discharges is only tens of joules.

Plasma spraying is widely used as the coating technique to form electrical insulation, heat resistance, and other functional layers on the material surfaces.[4] Recently, new spraying techniques, such as electro-thermally exploded powder spraying and electromagnetic acceleration plasma powder spraying are proposed and studied. We propose a novel spraying method that is microplasma spraying using electromagnetic acceleration of the copper powder microplasmas. In this paper, we discuss the electromagnetic acceleration of microplasmas and characterize the formation of copper thin film on substrates.

II .Experimental apparatus

Spraying material is an 8.18μg spherical copper particle of 120μm in diameter. Fig.1 is a photograph of the copper particles. A spherical material is suitable for the experiment because the handling is easy and the reproducibility of the pulsed discharge is high. It is advantageous for operation and application that the discharge experiment is carried out in air. The ratio of the electrostatic force to gravitational force on the particle increases with decreasing of the radius of particle. This enables us to control the particle with electrostatic force which makes the particle to be placed on the surface of electrodes. Manipulation and setting of the copper powder particle are performed observing a CCD camera image using an optical magnifying lens system.

Copper has often been used in the experiments of exploding wires and fiber pinches. Therefore, there are many data on the properties of copper, which is appropriate to be used in the microplasma spraying experiment.

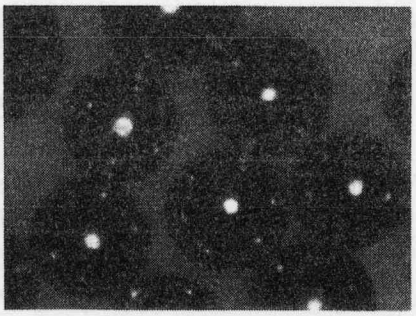

Fig.1. Spherical copper powder particles of 120μm in diameter

Fig.2 is a schematic of the discharge circuit. A capacitor bank of 6μF is charged to 2kV with a stored energy of 12J and is discharged with a spark-gap switch triggered by a pulsed voltage. When the pulsed current flows through the copper particle, its temperature will increase by Joule heating in a very short time. The particle develops into plasma from solid state through the phase transition process. It is accelerated by electromagnetic force simultaneously. We used a crowbar diode in the discharge circuit to obtain the discharge current without ringing for establishing efficient acceleration process. The rail electrodes are made of tungsten, of which both melting point and boiling point are higher than those of copper. Consequently, the plasma is not contaminated with tungsten. The length of the electrodes is 20mm and the cross section is 1mm x 1mm.

The discharge and electromagnetic acceleration are characterized using optical emission spectroscopy and current-voltage measurements. The spectroscopic measurements are conducted with an optical mulch-channel analyzer to examine excitation and ionization of copper atoms. Temporal and spatial evolution of the electromagnetic acceleration is observed with a streak camera, an ICCD camera, and a high-speed video camera.

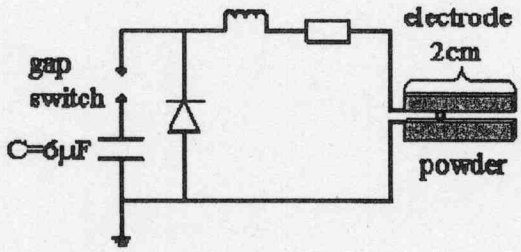

Fig.2. Schematic of the discharge circuit.

Ⅲ.Theoretical analysis

When current flows through the particle between rail electrodes, the particle gets electromagnetic force $F_{particle}$ of equation (1)

$$F = \frac{\partial}{\partial x}\left(\frac{1}{2}L'xi^2\right) = \frac{1}{2}L'i^2 \qquad (1)$$

Where L' is the rail inductance per unit length, x is the distance of particle along the rail electrode and i is current. The velocity of copper plasma v is expressed as equation (2)

$$v = \left(\frac{L'i^2}{2M} + f\right)t \qquad (2)$$

Where M is the mass and f is the external force except the electromagnetic force. The external force f includes frictional drag force and pressure drag force. However, these components are neglected, because they are much smaller than the electromagnetic force. Therefore, the electromagnetic acceleration depends on the discharge current and the rail inductance per unit length,.

The rail inductance per unit length L' is expressed as

$$L' = \frac{2\mu_0}{\pi h}\left[d\tan^{-1}\left(\frac{h}{2d}\right) + \frac{h}{4}\ln\left(1+\frac{4d^2}{h^2}\right)\right]. \qquad (3)$$

Where d is the separation between the rail electrodes.[5] It is equal to diameter of the particle. Therefore, the rail inductance per unit length L' is determined by the width of the rail electrode h. Fig.3 shows that the rail inductance per unit length decreases with increasing the width of the rail electrode. We took the width of the rail electrode as 1mm. Therefore, the rail inductance per unit length is 130nH/m.

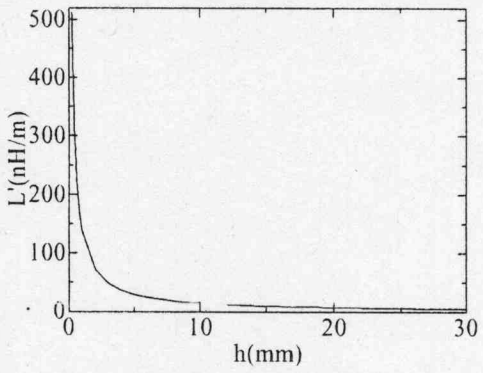

Fig.3. Relation between the rail inductance per unit length and the width of the rail electrode.

Resistance and inductance in the discharge circuit was determined as follows. In order to make the pulse width of the discharge current T long, the resistance has to be as small as possible. When the inductance is changed, temporal change of the discharge current is obtained with circuit analysis. The velocity v is calculated using the equation (2) taking the inductance as a parameter. Fig.4 shows the relation between the inductance and the plasma velocity. The inductance has to be chosen as 0.1μH ~1.5μH to obtain efficient acceleration.

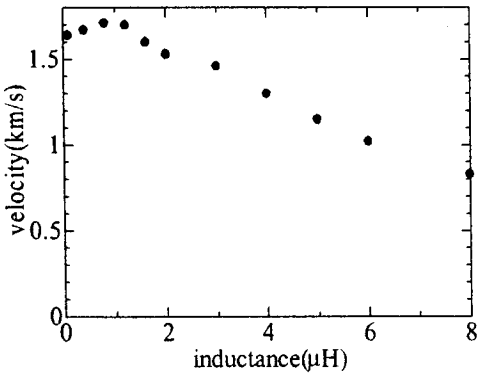

Fig.4. The plasma velocity dependence on the circuit inductance.

IV.Results and discussion

Fig.5 is the discharge current with the copper particle at charged voltage of 2kV. The current peak is 5kA at 3.3μs. The discharge current oscillates until 30μs because of the residual inductance in the circuit. The resistance 53m Ω and the inductance 800nH are obtained using the circuit analysis. The discharge current density is 1.1×10^{7}A/cm^{2}, which is almost similar level of that in high energy fiber pinches.

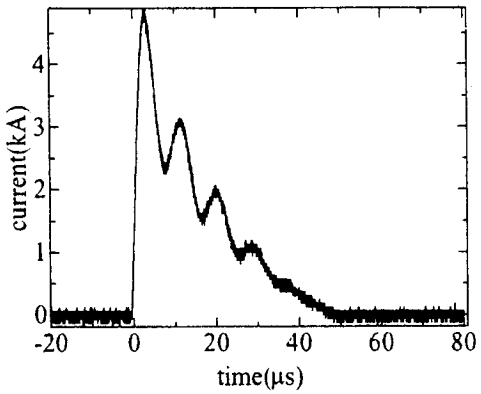

Fig.5. Discharge current with the copper particle at charged voltage of 2kV.

Fig.6 shows the temporal change in voltage, discharge current, and the resistance between the rail electrodes. The resistance is calculated from the relation between voltage and discharge current. The effective resistance between the rail electrodes is obtained as approximately 10mΩ, which stays constant during 20μs. The constant resistance means that both the copper vapor and the copper plasma exist for a long time between the rail electrodes.

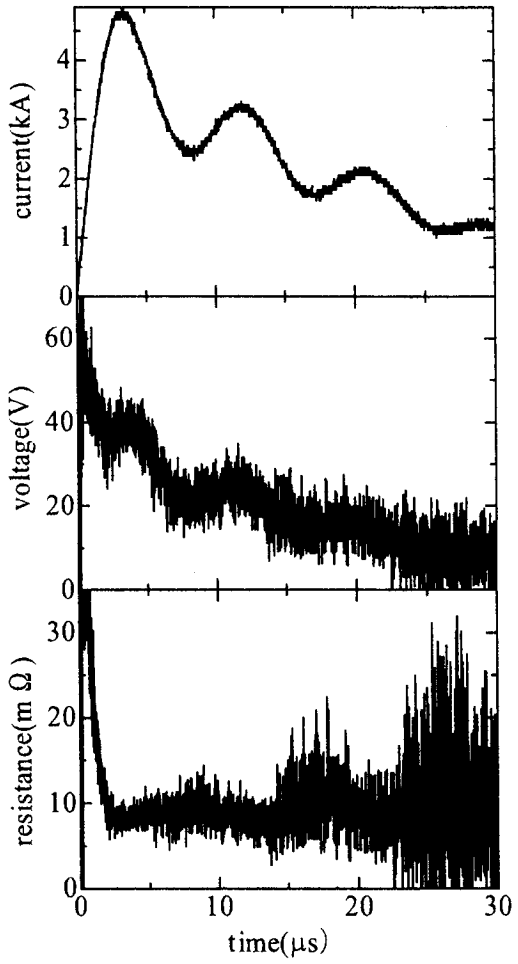

Fig.6. Temporal change in voltage, current, resistance of the discharge.

The incorporation of contaminated materials is a critical issue of the spraying technologies. Fig.7 shows time-integrated optical emission spectral profiles of copper atoms in the discharges. The copper atom lines, Cu I of 510.55nm, 515.32nm, 521.82nm, and 529.25nm are observed. Any other spectral lines of tungsten, oxygen, and nitrogen are not observed. Consequently, melting of the tungsten electrodes and ionization of molecules in air did not develop, because the electric field is lower than

1MV/m. Therefore, the formation of thin film with low contamination becomes possible.[6)]

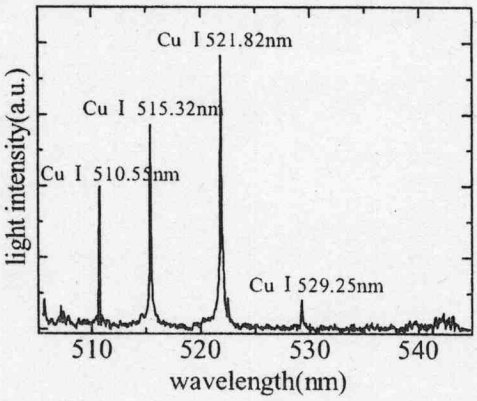

Fig.7. Time-integrated spectral profiles of the copper atomic lines.

Although the discharge is a phenomenon in tens micro-seconds, the high-speed video camera is useful for observing the macroscopic behaviors. Fig.8 shows a set of continuous frames of the discharge taken with the high-speed video camera operated with an exposure time of 32μs. The capacitor is charged to 2kV. The optical images of the plasma move toward the direction of the electromagnetic force. Therefore, it is confirmed that the electromagnetic acceleration takes place. When the current path was changed in such a way that electromagnetic force did not act to the copper plasma, no acceleration was observed.

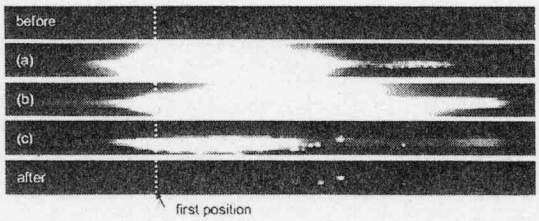

Fig.8. A set of continuous frames of the discharge taken with the high-speed video camera.

The temporal evolution of plasma acceleration was observed with the streak camera. Fig.9. shows the plasma acceleration along the rail electrodes. Time resolution of the streak camera is 400ns/mm. The charging voltage is 2kV. In the figure, the direction of electromagnetic force works upward. Axis of ordinates is 1.8mm and abscissa is 30μs. Because the copper vapor and plasma expands in orthogonal direction to the rail-electrodes, electromagnetic force decreases along the electrodes.

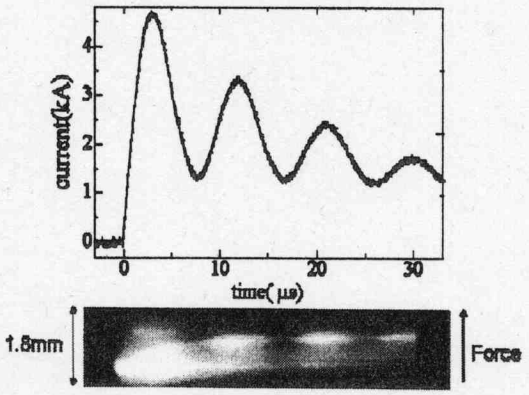

Fig.9. Streak photograph of copper plasma acceleration.

Time resolved structure of the discharge was recorded using the ICCD camera with the exposure time of 4ns. Fig.10 shows the temporal change in visible light emission of the copper plasma generated with the capacitor discharge. The capacitor is charged to 2kV. Strong light emission appears at the contact region between the particle and the rail electrodes, where Joule heating is remarkable because the current density is extremely high. The bright region moves along the electrodes. However, a portion of the particle stays at the initial position.

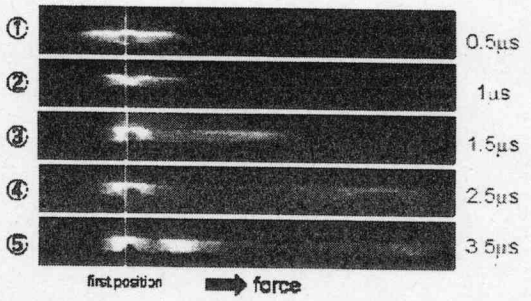

Fig.10. Time resolved structure of the discharge was recorded using the ICCD camera.

The plasma velocity reaches its maximum at 3μs. The velocities are obtained using the ICCD photographs at 3μs. Fig.11 shows the maximum velocity dependence on charging voltage. It increases with increasing charging voltage. When the charging voltage is 2kV, the plasma velocity is approximately 900m/s at the maximum.

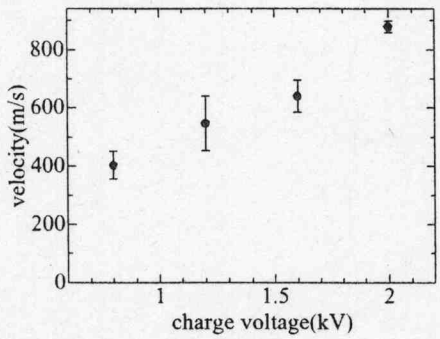

Fig.11. The maximum velocity dependence on charging voltage.

V. Formation of thin film

In order to verify whether it is possible to form thin film with the copper microplasma acceleration, substrates such as silicon or flat glass is placed near the end of rail-electrodes. The separation between the electrodes and the substrate was 2mm. Fig.12. is copper thin film formed on the glass observed with a microscope. We name the method micorplasma spraying. This is one of the fine processing technologies with microplasmas. The feature is that the process can be operated in atmospheric condition and the whole system is assembled compactly.

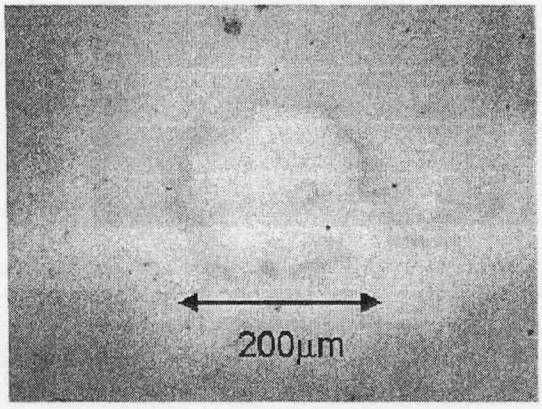

Fig.12. Copper thin film formed on the glass substrate.

VI. Conclusion

The copper micorplasma is accelerated by electromagnetic force in the narrow channel between the miniature electrodes. We used a crowbar diode in the discharge circuit to obtain the discharge current without ringing for establishing efficient acceleration process. In addition, the inductance had to be chosen as 0.1μH～1.5μH to obtain efficient acceleration. When the charging voltage is 2kV, the current peak is 5.5kA at 3.3μs. Time-integrated spectral profiles showed that melting of the tungsten electrodes and ionization of molecules in air did not develop. The electromagnetic acceleration of copper plasma was observed with the high-speed video camera, the streak camera, and the ICCD camera. It was confirmed that the electromagnetic acceleration took place. Moreover, the plasma velocity was approximately 900m/s at the maximum. Finally, copper thin film was formed on the glass substrate with the accelerated copper microplasma.

Acknowledgments

This work was supported by a Grant-in-Aid for Scientific Research from the Ministry of Education, Culture, Sports, Science and Technology: Scientific Research on Priority Areas.

References

1)S.Hamada,M.Kanemaru,S,Ibuka,K.Yasuoka,S,Ishii, "Electromagnetic Acceleration in a Copper Particle Microplasma and its Applications ", The paper of Technical Meeting on Plasma Science and Technology, IEEE Japan(2005), PST-05-98

2)M.G.Haines et al, "The past, present, and future of Z pinches", Physics of Plasmas, Vol.7, (2000), No.5, pp.1672-1680.

3)K.M.Chandler et al, "The Relationship Between Exploding Wire Expansion Rate and Wire Material Properties Near the Boiling Temperature", IEEE Transaction On Plasma Science, Vol.30, No.2, (2002), pp577-587.

4)Hirokazu Tahara et al, "Material Spraying Using Electromagnetically Accelerated Plasma", Japan Journal of Applied Physics, Vol.42 (2003), pp.3648-3655.

5)Victor Kowalenko, "Revisiting the performance of a plasma armature railgun", Journal of Physics D:Applied Physics , Vol.29, No.12, Dec 14, (1996), p3050-3062.

6)Takao Namihira et al, "Production of Nitric Monoxide Using Pulsed Discharge for a Medical Application", IEEE Transaction on Plasma Science, Vol.28, No.1, February, (2000), p109-114.

Lasing of recombination pumped soft X-ray laser

Yusuke Sakai, Takanori Komatsu, Yifan Xiao, Inho Song,
Masato Watanabe, Akitoshi Okino and Eiki Hotta

Department of Energy Sciences, Tokyo Institute of Technology,
4259-J2-35, Nagatsuta, Midori-ku, Yokohama 226-8502, Japan

Abstract

Characteristics of soft X-ray radiation from nitrogen Z-pinch plasma column energized by a capillary discharge is reported as a fundamental study for H-like N recombination pumped soft X-ray laser, wavelength of which is 13.4 nm emitted by quantum transition from $n = 3$ to $n = 2$. A current pulse of about 15 kA with half-cycle duration of about 110 ns was utilized to excite nitrogen plasma in a 3.0 mm diameter channel. From spectroscopic measurement using a transmission grating spectrometer, ionization degree of nitrogen ion in the plasma was analyzed to estimate plasma parameters and the discharge current required for a H-like N recombination soft X-ray laser.

Keywords: soft X-ray laser, recombination pumping, Z-pinch, capillary discharge.

I. Introduction

Wavelength of a laser has been shortened to soft X-ray region with technological advancement. A soft X-ray laser shows strong interaction with matter, by which are motivated application of photophysics, photochemistry, holography and lithography. Much effort has been made to realize soft X-ray lasers with shorter wavelengths. However, pumping devices should be extremely large in size such as synchrotrons used for free electron laser and high power lasers used for production of high-density high-temperature plasma, because exciting power is inversely proportional to 4th power of its wavelength. In 1994, J.J. Rocca et al. demonstrated the lasing of 46.9-nm Ne-like Ar soft X-ray laser utilizing fast capillary discharge to efficiently generate a plasma column in which amplification of radiation is obtained by collisional excitation[1]. In 2001, we also successfully lased a 46.9 nm Ne-like Ar soft X-ray laser utilizing this scheme by suppression of instability growth with effective use of predischarge[2]. The pumping scheme of capillary discharge Ne-like Ar soft X-ray laser is as follows. Once discharge current pulse of ~30 kA is applied to the capillary filled with preionized argon gas, a plasma column with an electron temperature of 60-80 eV and an electron density of 0.2 - 2×10^{19} cm^{-3} is formed due to the Z-pinch compression, which results in the generation of the population inversion for the 3p-3s transition. To shorten the wavelength of laser by capillary discharge, we investigate the possibility of H-like N recombination pumped soft X-ray laser, wavelength of which is 13.4 nm emitted by quantum transition from $n = 3$ to $n = 2$. This range of wavelength is so attractive because of existence of a Mo/Si multilayer mirror. And the possibility of H-like N recombination laser by capillary discharge has been reported by Vrba et al[3]. In this paper, ionization degree of nitrogen ion in a pinched plasma will be analyzed to estimate plasma parameters and discharge current required for recombination laser.

II. Principle of recombination pumping

The elementary process of three-body collisional recombination is expressed by

$$N^{7+} + e + e \rightarrow (N^{6+})^* + e.$$

The required excited state $(N^{6+})^*$ corresponds to the upper level of the Balmer α transition $n = 3$ to $n = 2$, and the lasing wavelength is 13.4 nm. In capillary discharge, as a current increases, a current sheet begins to implode toward the axis with increase of mass of plasma shell. A shock wave also propagates ahead of the current sheet, and converges on the axis. The current sheet subsequently reaches the axis and highly compresses the plasma column. This leads to production of a hot dense plasma, which is capable of generating highly ionized nitrogen N^{7+}. In the pinch time, plasma temperature required to generate fully stripped nitrogen ions should be higher than about 150 - 200 eV according to the Saha equation. After the maximum pinch the plasma column then starts to expand and the plasma temperature becomes cooler. To obtain the gain $G > 1$ cm^{-1}, in this expansion phase, required electron density is of the order of 1×10^{20} cm^{3} and plasma temperature should be lower than about 100 eV to initiate the recombination process in the plasma according to three-body collisional scheme, where G is given bellow[4, 5],

$$G = \frac{\lambda^3 n_u A_{ul} F}{8\pi c(\Delta\lambda/\lambda)}$$

Here, λ is the wavelength of laser, A_{ul} is the Einstein's coefficient, F is the inversion function, n_u is the ion number density in upper level,

$$n_u = \sum_k C_{n=3,n'=k}^{z=6} N_{n=k}^{z=6}.$$

The collisional transition rate $C_{n'n}$ is expressed as a function of an electron density and an electron temperature of the plasma in the expansion phase,

$$C_{n'n}^{z-1} = \langle \sigma_{n'n}^{z} v_e \rangle N_e$$
$$\approx \frac{m_e \pi}{2\Delta E_{n'n}} \left[\frac{e^2}{4\varepsilon_0 \hbar} \langle \psi_n | r | \psi_{n'} \rangle \right]^2 \left(\frac{2m_e}{\pi kT} \right)^{1/2} e^{-\frac{\Delta E_{n'n}}{kT}} N_e$$

where, v_e is the velocity of electron, $\sigma_{n'n}$ is the average collisional transition cross section by coulomb potential, N is the ion number density, z is the ionic charge number, $E_{n'n}$ is the gap energy of two-level system and ψ is the wave function of H-like nitrogen.

III. Experimental

The discharge system used in this experiment consists of a 3-stage Marx generator, a 2:28 step-up transformer, a 3-nF water capacitor and a discharge section including a capillary with diameter of 3 mm as shown in Fig. 1. Using this apparatus, Ne-like Ar 46.9 nm laser was observed as a spike of X-ray diode (XRD) signal as shown in Fig. 2 on the following condition, discharge current with moderately low peak amplitude of 13 kA and half cycle duration of 110 ns, and initial filling Ar gas pressure of 300 mTorr.

Spectroscopic measurement of radiation from the nitrogen plasma was carried out using a transmission grating spectrometer with a lattice constant of 1/1000 mm^{-1} in combination with an X-ray CCD camera which has a 1024 × 1024 pixel area. Each pixel is a 13-μm square. The transmission grating was placed at a distance of 60 mm from the end of capillary. The distance between the grating and the CCD camera was 40 mm. A resolution of the spectrometer in this configuration is about 1 nm. Discharge condition was similar to that of Fig. 2, with current peak value of about 15 kA, initial gas pressure of 300 mTorr.

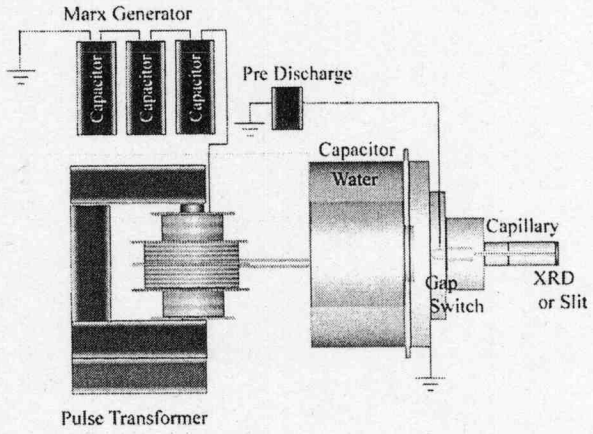

Fig. 1. Schematic diagram of the discharge system.

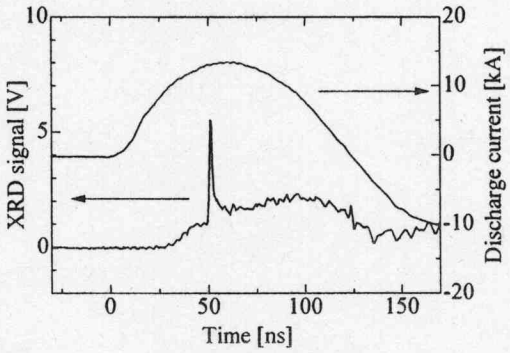

Fig. 2. Discharge current waveform and XRD signal of Ne-like Ar laser.

IV. Results and discussion

Obtained emission spectrum is shown in Fig. 3. Strong line emissions at wavelengths corresponding to N VI-III are observed in 10 - 40 nm range which is maximum abundant at a temperature of ~10 - 30 eV. On the other hand, weak line emissions in the range of 5-10 nm reveal the existence of N VII which is necessary for recombination pumping. It suggests that a plasma temperature at the pinch time is higher than about 150 eV. Assuming that Bennet's relation can be applied to the pinch plasma and nitrogen atom is fully ionized to N VI, plasma temperature T_e in the pinch column is evaluated to be

$$T_e = \frac{\mu_0}{8\pi^2 a^2 N_e k} I^2 \approx 100\,[\mathrm{eV}],$$

where N_e is the electron number density, k is the Boltzmann constant and a is the diameter of pinch plasma ≈ 100 μm. In this evaluation, electron density at the pinch time can be approximated by the following equation,

$$N_e \approx \sum_{z=1\to5} zN^{z+} \approx 5\times2\times\rho\times N_0 \approx 2\times10^{19}\ [cm^{-1}],$$

where ρ is the compression ratio of the pinch, N_0 is the initial nitrogen gas density. Thus, dynamic pinch plasma temperature in this experiment is higher than that estimated by Bennet's relation. It is due to the shock wave heating, joule heating of plasma and conversion of kinetic energy of current sheet into thermal energy.

For realizing a H-like N recombination soft X-ray laser, required electron density may be higher than the order of 1×10^{20} cm^{-3}, which is about 5 times higher than that used in this experiment. Besides, recombination occurs in the expansion phase after the pinch. In the expansion phase, plasma density becomes a few times lower than that at the maximum pinch. In the maximum pinch phase, plasma temperature required to generate fully stripped nitrogen ions should be higher than about 150 - 200 eV, and in the expansion phase, plasma temperature should be lower than about 100 eV to initiate the recombination process in the plasma. Actually, in the expansion phase, plasma starts to cool down due to expansion, radiation losses and current decay. As a simple estimation, assuming that the plasma expands adiabatically, adiabatic condition gives the relation between the electron number density of the pinched plasma of about 200 eV and the expanding plasma of about 100 eV,

$$N_{e,expansion} = N_{e,pich}\left(T_{expansion}/T_{pinch}\right)^{\frac{1}{\gamma-1}} \approx N_{e,pich}/3,$$

where γ is adiabatic constant γ = 5/3. So, the electron density at the lasing time is about 3 times lower than that at the pinch time.

Thus, to obtain required electron density for recombination laser N_e > 1×10^{20} cm^{-3} at the pinch time, initial filling gas density should be 5×3 ≈ 10 - 20 times higher than that used in this experiment.

Since a current amplitude is proportional to the square root of an electron density from Bennet's relation to obtain such high density plasma, discharge current should be increased to over 3 – 5 times higher than that used in this experiment, which is about 15 kA. Thus, required discharge current for H-like N recombination laser will be over 50 - 70 kA. Therefore, to obtain enough population inversion for lasing a 13.4 nm soft X-ray laser, it is necessary to make substantial improvement of discharge system.

V. Conclusion

As a fundamental study for lasing a H-like N recombination soft X-ray laser, spectroscopic measurement was carried out using a transmission grating spectrometer. Strong line emissions at wavelengths corresponding to N VI-III were observed in the 10 - 40 nm range. On the other hand, weak line emissions in the range of 5 - 10 nm reveal the existence of N VII which is necessary for recombination pumping. It suggests that a plasma temperature at the pinch time is higher than about 150 - 200 eV. However, to realize the H-like N recombination laser, an electron density must be 10 - 20 times higher than that used in this discharge experiment, which suggests that required discharge current for H-like N recombination laser will be over 50 - 70 kA.

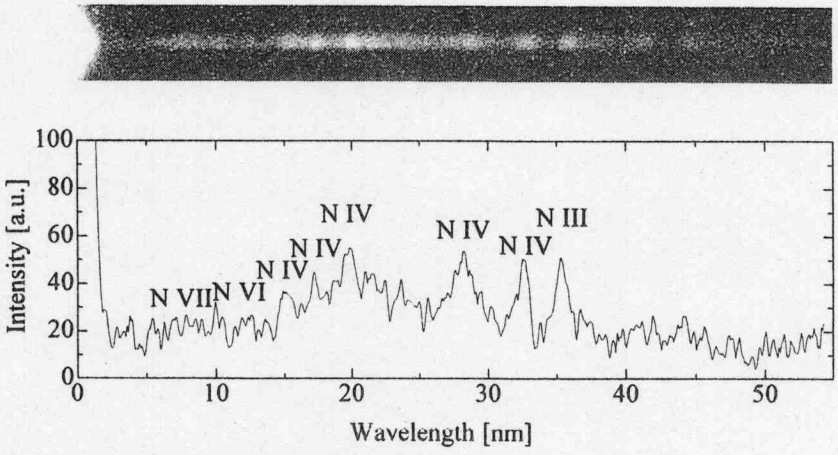

Fig.3. Emission spectrum of the radiation from the capillary discharge in nitrogen. Initial filling pressure is 300 mTorr, capillary diameter is 3 mm, peak discharge current is 15 kA.

1. J. J. Rocca, V. Shlyaptsev, F. G. Tomasel, O. D. Cortazar, D. Hartshorn and J. L. A. Chilla " Demonstration of a Discharge Pumped Table-Top Soft X-ray Laser" , Phys. Rev. Lett., **73**, 2192-2195 (1994).
2. G. Niimi, Y. Hayashi, N. Sakamoto, M. Nakajima, A. Okino, M. Watanabe, K. Horioka, and E. Hotta " Development and Characterization of a Low Current Capillary Discharge for X-ray Laser Studies" , IEEE Trans. Plasma Sci., **30**, 616-621 (2001).
3. Pavel Vrba, Miroslava Vrbova, Nadezhda A. Bobrova, Pavel V. Sasorov, "Modelling of a nitrogen x-ray laser pumped by capillary discharge", Central European Journal of Physics, **3**, 564-580 (2005).
4. Hans R. Griem, "Plasma spectroscopy", McGraw-Hill (1964).
5. David Attwood, "Soft X-rays and extreme ultraviolet radiation", CambridgeUniversity Press (1999).

EFFECT OF FOCUSING FIELD ERROR DURING FINAL BEAM BUNCHING IN HEAVY-ION-BEAM DRIVEN INERTIAL CONFINEMENT FUSION

T. Kikuchi, S. Kawata*, M. Nakajima**, and K. Horioka**

Department of Electrical and Electronic Engineering, Utsunomiya University, Utsunomiya 321-8585, Japan
*Department of Energy and Environmental Science, Utsunomiya University, Utsunomiya 321-8585, Japan
**Department of Energy Sciences, Tokyo Institute of Technology, Yokohama, 226-8502, Japan

ABSTRACT

Emittance growth due to the transverse focusing field error is investigated during the final beam bunching in the energy driver system of heavy ion inertial fusion. The beam bunch is longitudinally compressed during the transport with the field error in the continuous focusing (CF) or the alternating gradient (AG) field lattices. Numerical calculation results show the only 2% difference of the emittance growth between the cases with and without field error in the CF lattice. In the case of the AG lattice model with the field error of 10%, the emittance growth of 2.4 times is estimated, and the major difference between the CF and AG models is indicated from the numerical simulations.

1 Introduction

In heavy ion inertial fusion (HIF) [1] , energy of several MJ should be injected as a short time pulse to a fuel pellet. The target pellet illuminated by the energy driver is rapidly imploded. The implosion can cause a high energy density state at the center of the pellet, and thermonuclear reactions can produce the high-temperature dense plasma. The intense heavy-ion beam (HIB) is one influential candidate as the energy driver, and the physics of space-charge-dominated beams is crucial in the HIF study [1].

Required parameter values of HIB are several GeV particle energy, ~100 kA total current, and ~10 ns short pulse duration [2], and the beam parameters are far from those of conventional particle accelerator system. Therefore the beam dynamics and control are important research issues in HIF. At the final stage, the beam pulse must be longitudinally compressed from ~100 to ~10 ns.

Induction voltage modulators, which have a precise waveform controllability, are useful devices for this purpose [3]. For an effective pellet implosion, we should transport and compress the bunch of HIB with a low emittance growth. A final focus and beam illumination are crucial, but a large emittance interferes the focusing to the small fuel pellet [4, 5]. For this reason, the final beam bunching and the final focusing are a key technology in the HIF driver system. In these regions, the intense HIB is in the space-charge-dominated state, and beam instabilities occur during the beam transport. Dilution of particle distribution can also cause the emittance growth, because nonequilibrium particle distribution will approach to a thermal equilibrium state [6].

In our previous studies [7, 8, 9, 10], the beam instability excited by the strong space charge effect was observed using multiparticle numerical simulations during the final beam bunching. The final beam bunching was carried out by the beam transport using the continuous and alternating focusing lattice system. In this study, we also investigate the beam dynamics during the bunch compression with the focusing error field. The particle-in-cell (PIC) [11] simulation with a longitudinal bunch compression model [12] is carried out to investigate transverse particle behaviors. The emittance growth due to the field error is shown by

using the numerical simulations.

2 Simulation model and beam parameters

The high-energy particle beam is transported by using a magnetic quadrupole focusing channel as a unit of focus-drift-defocus-drift (FODO) lattice [13]. Generally, the beam transport by the FODO lattice causes a non-axisymmetric behavior in the beam cross-section. We are interested in such beam dynamics with a longitudinal bunch compression. For the above reasons, the fully three-dimensional numerical scheme is essentially required by the beam dynamics simulation. From the viewpoint of the computational cost, the full calculations are difficult. While the longitudinal bunch length is of the order of meter, the scale of the transverse cross section is only a few cm in the stage of final beam bunching [14]. Consequently, the small-scale phenomena by the space charge structure will be dominated by the transverse beam dynamics.

We deal with the particle dynamics in the transverse cross section of the beam by multi-particle simulations, and the effect of longitudinal compression is introduced as the beam current increases. The linear current increase model causes the most serious influence in the particle dilution in the phase space. From the viewpoint of the beam physics study, the history of linear current increase is assumed as model of the longitudinal bunch compression.

We use the PIC method for descriptions of the transverse behavior with the longitudinal compression, the effect of which was evaluated by assuming linear increase in the beam current. In this study, we simply assume the effect of the self-magnetic field as factor of $1/\gamma^2$ [15]. The charge and mass of the super particles are re-weighted with the beam transport [12]. The quadrupole occupancy is fixed at 0.5, and the one lattice period is 3 m.

The beam parameters are assumed as Table 1 [2]. The initial generalized perveance is assumed to 3.58×10^{-6}. The initial undepressed and depressed phase advances are $\sigma_0 = 72$ deg and $\sigma = 65.2$ deg. The transverse calculation region is fixed at the square of 10 cm × 10 cm, and the outer boundary condition is given as a conductor wall. The

Table 1: Beam parameters for final beam bunching in HIF.

Ion species	Pb^{1+}
Number of ions	6.25×10^{14}
Particle energy [GeV]	10
Initial beam current [A]	400
Final beam current [kA]	10
Initial pulse duration [ns]	250
Final pulse duration [ns]	10

rms matched Gaussian [16] beam is chosen as the initial particle (non-stationary) distribution.

Since the behavior likes a quasi-neutral plasma, the Debye shielding is important issue in this region. The grid size of $0.23\lambda_D$ is used to satisfy the Debye shielding effect and the calculation cost [11]. For the validation of the numerical convergence, we also tried to check the calculation results using the different numbers of grids and super particles. The mesh number is varied from 64×64 to 1024×1024, and the super particle number is changed from 1×10^5 to 3×10^6. As mentioned earlier, we tried to check the many test calculations to change the numbers of particles and cells used.

We study the emittance growth mechanism with two types of the transverse focusing lattice system, i.e. an alternating gradient (AG) focusing and a continuous focusing (CF) configurations. Figure 1 shows the focusing models during the beam transport. The transverse focusing coefficients k_x and k_y are constant for the continuous focusing model, and are given as the alternate values for the AG focusing model as shown in Fig. 1. Studying the effect of the focusing field error, we introduce the error δk, which has the normal distribution. As a result, the focusing forces including the field error are given by $k_x + \delta k$ and $k_y + \delta k$.

3 Numerical Simulation Results

We simulate numerically the beam dynamics with the focusing field error during the final beam bunching with the CF and AG focusing models. The emittance value can be used to evaluate the beam quality. We define the average of unnormalized rms transverse emittance ϵ as

$$\epsilon = \frac{\epsilon_{x,rms} + \epsilon_{y,rms}}{2}, \qquad (1)$$

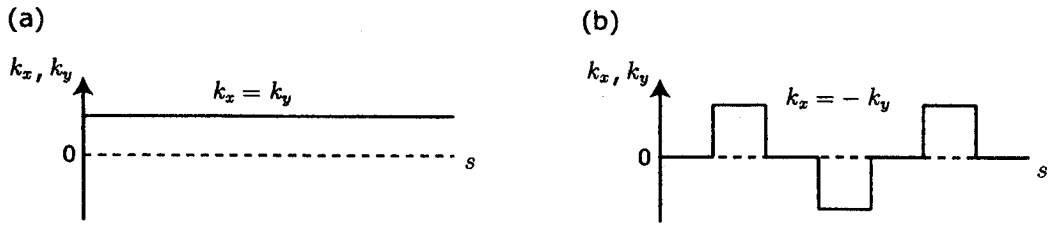

Figure 1: Calculation model of transverse focusing lattice system, (a) for continuous focusing (CF) lattice case, (b) for alternating gradient (AG) focusing case (FODO).

where $\epsilon_{x,rms}$ and $\epsilon_{y,rms}$ are the unnormalized rms emittances for horizontal and vertical directions given by

$$\epsilon_{x,rms} = \left[\langle x^2\rangle\langle x'^2\rangle - \langle xx'\rangle\right]^{1/2}, \qquad (2)$$

and

$$\epsilon_{y,rms} = \left[\langle y^2\rangle\langle y'^2\rangle - \langle yy'\rangle\right]^{1/2}, \qquad (3)$$

respectively. The initial emittance is assumed at $\epsilon_i = \epsilon_{x,rms} = \epsilon_{y,rms}$ =10 mm mrad.

The evolutions of the emittance growth ϵ/ϵ_i, which indicates the ratio of the average emittance to the initial one at each lattice period, are shown in Figs. 2 and 3. Figure 2 shows the calculation result with the field error in the case of the beam transport with the CF lattice. The relative rms value $(\delta k/k)_{rms}$ of the field errors applied by the pseudo random numbers of the normal distribution is 0.1. As shown in Fig. 2, the additional emittance growth after the longitudinal bunch compression is observed by only 2 %. Figure 3 shows emittance growth history during the final beam bunching with the focusing field error in the AG field lattice. To change the focusing field error ratio $(\delta k/k)_{rms} = 0 \sim 0.1$, we can compare the emittance growth due to the longitudinal compression with the field error. In the case of $(\delta k/k)_{rms} = 0.01$, the emittance growth is almost same value in the comparison with the result in no-field error case. However, the emittance growth of 2.4 times is indicated in the longitudinal bunch compression with the 10% focusing field error. The results show the difference between the beam transport in the CF and AG field lattices with the focusing field error.

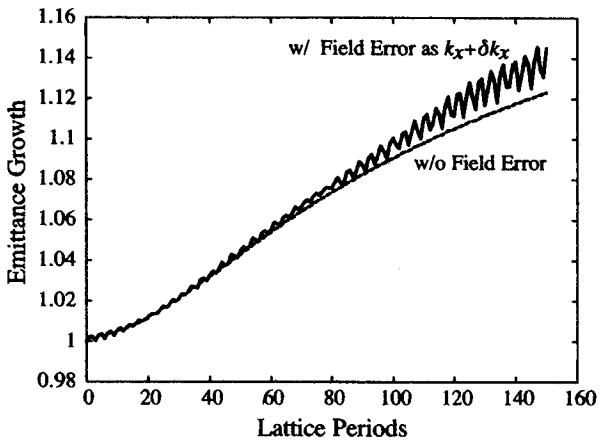

Figure 2: Evolution of the rms emittance during the final beam bunching with CF lattice.

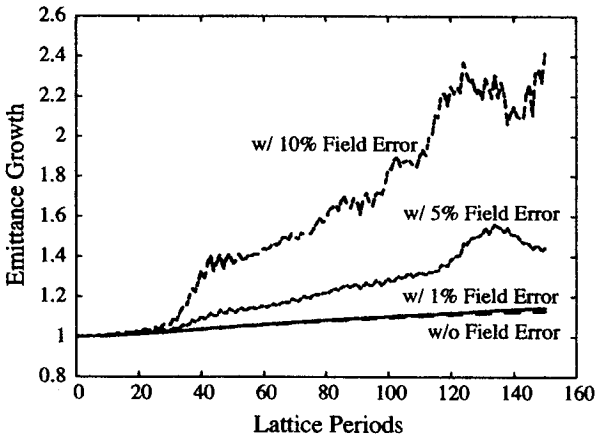

Figure 3: Evolution of the rms emittance during the final beam bunching with AG focusing lattice.

4 Conclusions

The emittance growth during the final beam bunching with the transverse focusing field error was numerically investigated for the HIF driver system design. The longitudinal bunch compression with the focusing field error caused the additional emittance growth due to the field error. In the case of the CF lattice transport, the emittance growth due

to the field error was only 2% lager than the normal case, but the emittance growth of 2.4 times is estimated in the case of the AG focusing lattice with the field error of $(\delta k/k)_{rms} = 0.1$. It is found that the beam behaviors in the axisymmetric assumption differ substantially from the non-axisymmetric model in the final beam bunching with the focusing field error.

Acknowledgments

This work was carried out under the collaborating research program at National Institute for Fusion Science. This work was supported by JSPS (Japan Society for the Promotion of Science) No. 17740361 and MEXT (Ministry of Education, Culture, Sports, Science and Technology). We would like to thank Drs. J. Hasegawa and Y. Oguri for useful advices.

References

[1] J.J. Barnard, J. Fusion Energy **17**, 223 (1998).

[2] J.J. Barnard, R.O. Bangerter, A. Faltens, T.J. Fessenden, A. Friedman, E.P. Lee, B.G. Logan, S.M. Lund, W. Meier, W.M. Sharp, and S.S. Yu, Nucl. Instrum. Methods in Phys. Res. **A415**, 218 (1998).

[3] K. Horioka, M. Nakajima, M. Watanabe, M. Honda, E. Hotta, M. Shiho, M. Ogawa, J. Hasegawa, J. Kishiro, and K. Takayama, Laser Part. Beams **20**, 609 (2002).

[4] T. Someya, A.I. Ogoyski, S. Kawata, and T. Sasaki, Phys. Rev. ST Accel. Beams **7**, 044701 (2004).

[5] A.I. Ogoyski, S. Kawata, T. Someya, A.B. Blagoev, and P.H. Popov, J. Physics D **37**, 2392 (2004).

[6] S.M. Lund, J.J. Barnard, and J.M. Miller, Proceedings of the 1995 Particle Accelerator Conference, Dallas, May 1995, p.3278.

[7] T. Kikuchi, M. Nakajima, and K. Horioka, J. Plasma Fusion Res. **79**, 105 (2003).

[8] T. Kikuchi, M. Nakajima, K. Horioka, and T. Katayama, Phys. Rev. ST Accel. Beams **7**, 034201 (2004).

[9] T. Kikuchi, T. Someya, S. Kawata, M. Nakajima, K. Horioka, and T. Katayama, Nucl. Instrum. Methods in Phys. Res. **A 544**, 262 (2005).

[10] T. Kikuchi, T. Someya, S. Kawata, M. Nakajima, and K. Horioka, NIFS-PROC-61, 143 (2005).

[11] R.W. Hockney and J.W. Eastwood, *Computer Simulation Using Particles*, McGraw-Hill, New York, (1981).

[12] S.M. Lund, O. Boine-Frankenheim, G. Franchetti, I. Hofmann, and P. Spiller, Proceedings of the 1999 Particle Accelerator Conference, New York, March 1999, p.1785.

[13] M. Reiser, *Theory and Design of Charged Particle Beams*, Wiley, New York, (1994).

[14] T. Kikuchi, M. Nakajima, and K. Horioka, Laser Part. Beams **20**, 589 (2002).

[15] S. Machida and M. Ikegami, Proceedings of the Workshop on Space Charge Physics in High Intensity Hadron Rings, AIP Conf. Proc. No.448 (AIP, New York, 1998), p.73.

[16] Y.K. Batygin, Proceedings of the Computational Accelerator Physics Conference, Los Alamos, 1993, AIP Conf. Proc. No. 297, (1994) p.419.

Development of High Repetition-Rate Pulse Generator Using SI-Thyristor

K. Nakahiro[1)], W. Jiang[1)], K. Yatsui[1)], M. Wake[2)], K. Takayama[2)], and N. Shimizu[3)]

[1)] Extreme Energy-Density Research Institute, Nagaoka University of Technology

[2)] High Energy Accelerator Research Organization (KEK)

[3)] Corporate Technical Center, NGK Insulators Ltd

Abstract

This paper reports the development and evaluation of a pulsed high-voltage generator that used static induction thyristor (SIThy) for achieving high repetition rate. The surface temperature rise of SIThy had been measured by using thermo-couple. For switching loss of ~ 2 kW, the temperature rise of the switching unit is estimated to be ~ 62 °C while using a cooling system.

I. INTRODUCTION

Pulsed power generators are being developed for potential applications to induction synchrotrons. These generators are expected with the following capabilities. Maximum repetition frequency ≥ 1 MHz, voltage ≥ 2kV, and current ≥ 20 A. So far, MOSFETs are used as the switching devices for the pulsed power generators.[1)] However, the withstand voltage of MOSFET is relatively low compared with other semiconductor switches. Therefore, they are used in series connection. The generator uses many MOSFETs at the same time that are synchronized with each other.

By replacing MOSFET with static induction thyristor (SIThy), generators may expect characteristics such as low failure probability and small size. We have developed pulse generator using SIThy of high repetitive rate and succeeded in operation at 2 kV and 1 MHz. However, the switching loss increased significantly when compared with that of MOSFETs. In order to operate the generator in continuous mode, it is necessary to develop a stronger cooling system. This paper developed and evaluated different cooling systems for operating pulse generator that used SIThy of high repetition rate.

Figure 1 shows the photograph of a SIThy. The specifications of this SIThy is as follows: withstand voltage 4 kV, peak current 400A. It is a normally-on element and is possible to operate at high speed switching.

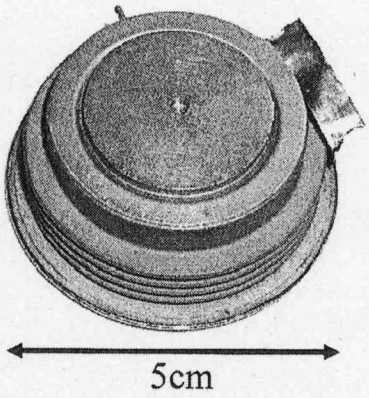

Fig.1 Photograph of SIThy.

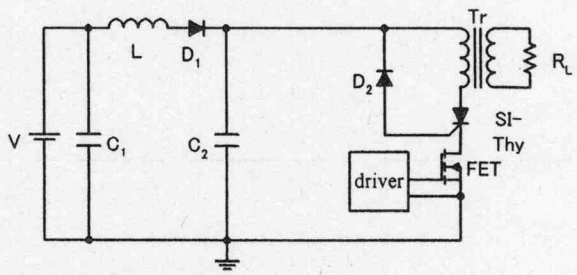

Fig.2 Experimental circuit.

Table 1 Experimental conditions

Input voltage	200V
Load	1.3kW
Operating frequency	1~50kHz
Cooling nethod	Air , Oil
Oil amount	40l
Oil flow	10l/min
Water flow	15l/min
Operating time	10 minute
Cooling system	No.0 , No.1 , No.2

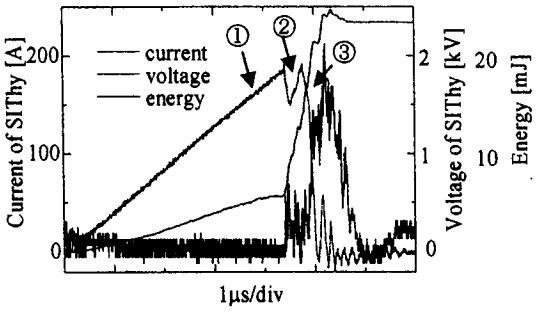

Fig.3 Voltage and current waveforms of SIThy and switching-loss energy of 1 shot.

II. Experimental Setup

Figure 2 shows the experimental circuit. Capacitors C_1 and C_2 are charged to 200V by DC power supply. When MOSFET is closed, C_2 discharging current flows through SIThy via primary winding of transformer and inductive energy accumulates to the transformer. When the MOSFET is switched off during the C_2 discharging, current flowing through SIThy switches to anode-gate from anode-cathode and the carriers of SIThy are extracted from gate electrode. The current is interrupted at high speed. Then, the voltage, which is given by Ldi/dt, appears in the primary winding of the transformer.

The voltage V=Ldi/dt appear across the voltage amplifying transformer appears across load resistance R_{load}. This kind of circuit, where the output voltage is generated by using inductive energy, is called induction energy storage (IES) generator.[2] Table 1 shows experimental condition.

Figure 3 shows typical voltage and current waves of IES generator. The voltage and current waveform was measured by using high-voltage probe, Pulse Electronic Engineering EP-50K, and current monitor of Pearson 110A. Current waveform is composed of the following 3 parts. The first part, current increases linearly, MOSFET is in conduction state. The second part, it is the time period when the current switches from MOSFET of off-state to SIThy.

The third part, it is time to produce depletion layer. Switching loss energy of 1 shot was calculated by the following equation.

$$\text{Energy} = \int V_{SI} I_{SI} dt$$

where V_{SI} and I_{SI} are voltage across SIThy and current flowing through SIThy, respectively.

The switching loss of SIThy is about 23 mJ. To obtain the switching loss of 2kW with IES circuit, it needs repetitive rate of 100 kHz. Table 1 shows experimental conditions of cooling system. No.0 cooling system operate generator in the air without cooling. No.1 cooling system operate generator in the oil tank. The oil was circulated by cooling unit, SL-307W1. No.2 cooling system combines no.1 cooling system with two cooling heat sinks. Figure 4 shows photograph of circuit that is mounting water cooled heat sinks. The generator use these system is operated at frequency of 1 ~ 50 kHz for 10 minutes. Surface temperature of SIThy is measured every 1 minute by thermo-couple. Since maximum allowable operation temperature of SIThy is ~100°C, maximum

operation temperature of this experimental is set at 80°C. ΔT is obtained by subtracting initial temperature from surface temperature of SIThy.

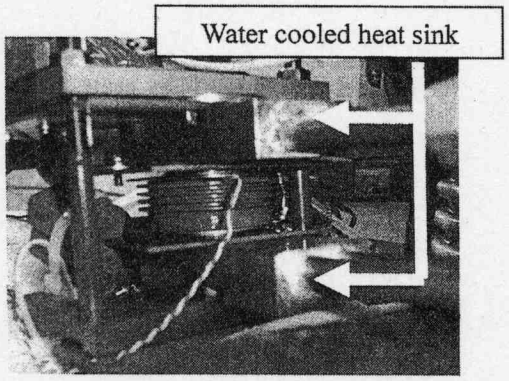

Fig. 4 Photograph of circuit that is mounting water cooled heat sinks

III. EXPERIMENTAL RESULTS

Figure 5 shows experimental result obtained in the air. The repetition rate of 3 kHz and 5 kHz, surface temperature reached 80°C in 6 and 3 minute, respectively. Figure 6 shows experimental result obtained with no.1 cooling system.

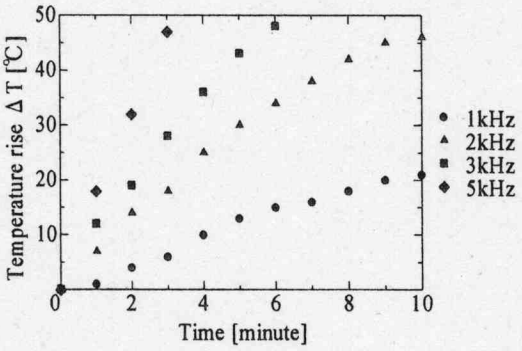

Fig. 5 Relation of operation time and temperature rise in the air when repetition rate was changed.

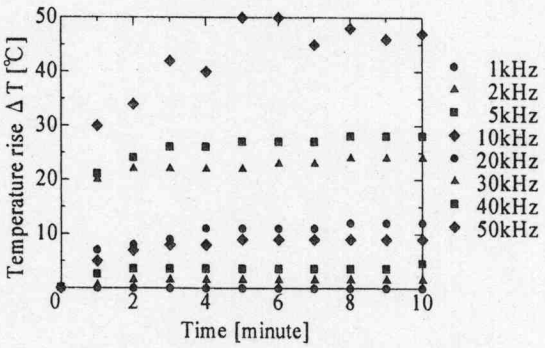

Fig. 6 When repetition rate was changed by using no.1 cooling system, it is relation of operation time and temperature rise.

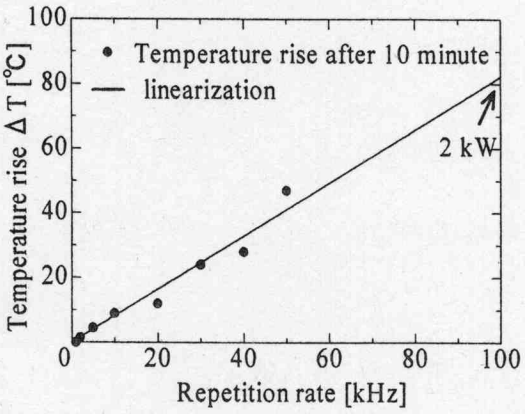

Fig. 7 By using no.1 system, it is relation of repetition rate and temperature rise after 10minute

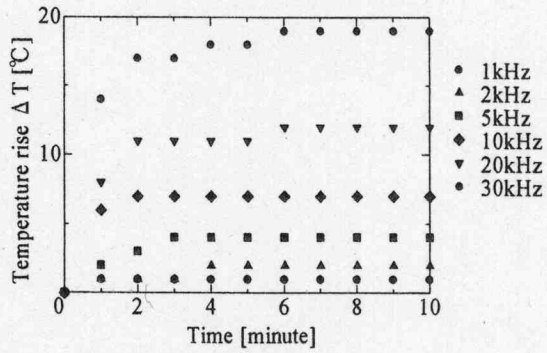

Fig. 8 When repetition rate was changed by using no.2 cooling system, it is relation of operation time and temperature rise.

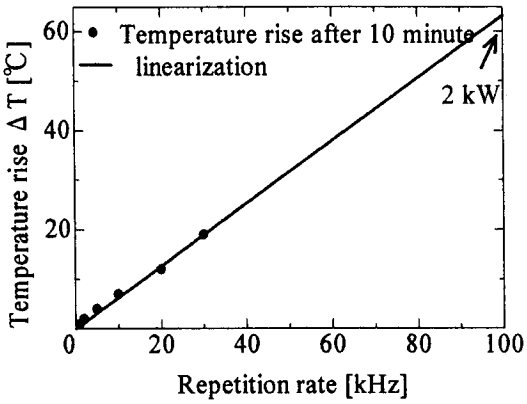

Fig.9 By using no.2 system, it is relation of repetition rate and temperature rise after 10minute

Temperature after 10 minutes is saturated repetition rate of 1~50 kHz. From this result, Fig. 7 shows relation of repetition rate and temperature rise after 10 minutes. Where solid line is collinear approximation of plot. For this graph, repetition rate and saturate temperature is direct proportionality relation. If repetition rate assured 100 kHz (switching loss is 2 kW) from line and plot, temperature rise is about 84, 94 ˚C, respectively. Therefore, cooling capacity is lacking only no.1 cooling system. Figure 8 shows experimental result of no.2 system. Temperature after 10 minutes is saturated repetition rate of 1~50 kHz. From this result, Fig.9 shows relation of repetition rate and temperature rise after 10minute. Where solid line is collinear approximation of plot. For this graph, repetition rate and saturate temperature is direct proportionality relation. If repetition rate assured 100 kHz (switching loss is 2 kW) from line, temperature rise is about 62 ˚C. Therefore, cooling system needs modification.

IV. CONCLUSION

- When the generator operated with repetition rate of 5 kHz (switching loss is 60 W) in the air, temperature rise reaches 50 ˚C in 3 minutes.
- When switching loss is 2 kW, temperature rise of element is expected 94 ˚C by using no.1 cooling system.
- When switching loss is 2 kW, temperature rise of element is expected 62 ˚C by using no.2 cooling system.

REFERENCES

1) Ken Takayama*, Junichi Kishiro "Induction synchrotron", Nuclear Instruments and Methods in Physics Research A 451 (200) 304-317

2) K.Iida and T.Sakuma, "The ultra short pulse generating circuit utilizing Static Induction Thyristor." The 15th Symposium of Atatic Induction Devices, SSID-02-9,pages 45-50,July2002

5 GHz superradiance using intense electron beams with modified energy waveforms

Reiji Nakajima, Akihiro Osawa, Tomoaki Kurihara, Ritoku Ando,
Keiichi Kamada and Naum S. Ginzburg*

Graduate School of Science and Technology, Kanazawa University, Kanazawa, Japan
**Institute of Applied Physics, Russian Academy of Sciences, Nizhny Novgorod, Russia*

Pulsed intense electromagnetic wave with frequency of 5 GHz, power of 300 MW and duration of 4 ns was observed, when an intense relativistic electron beam with energy of 500 keV, current of 5 kA and duration of 12 ns was injected into a corrugated waveguide. Particle-in-cell code KARAT indicated that the mechanism of radiation was identified to be superradiance. The time evolution of the energy of the electron beam was modified by a coaxial cavity. The experimental results showed that that the energy waveform of the electron beam affected the output power of the radiation.

1. Introduction

Intense electromagnetic radiation sources are developed for applications in nuclear fusion, particle accelerators, radars, etc. Radiation sources with output power of $\sim$1 MW and frequency of up to 200 GHz are achieved by Gyrotron etc, however, those with output power over 1GW are still in an experimental stage. An intense relativistic electron beam (IREB) is used as a convenient energy source for the radiation sources with power over 1 GW, though its low beam quality caused by expansion of diode plasma and small repetition rate for operation are remained to be developed technically. Usually, the high power devices employ the conventional mechanisms for microwave radiation, which are applied to the low power devices. However, the strong electric field of the radiation causes the breakdown in the device within 100 ns. To develop new mechanisms of short-pulsed electromagnetic radiation with high efficiency is important for high power devices. Stimulated emission from electron bunches, superradiance (SR), is an attractive method of generating ultra short electromagnetic pulses. Different types of SR emission (Cherenkov, cyclotron, etc.) were studied theoretically and generations of SR pulses have been observed experimentally at millimeter waveband through the frequencies 35-150 GHz [1-5]. As the peak output power proportional to N^2 is emitted in SR, where N is the number of electrons, the SR can be considered as effective method of generation of ultra short intense electromagnetic pulses with output power over 1 GW using an IREB. As the increase of operating wavelength leads to the increase of the electron pulse total duration, an IREB with pulse duration of 10 ns can be employed for the long wavelength in S band. Cherenkov mechanism with short electron beam moving in corrugated waveguide is expected to be the most effective scheme for generation of SR pulses at S bands. We report here the experimental results of S-band SR using a corrugated waveguide. Moreover, it was proposed that the output power of SR could be increased by using an electron beam with a time-increasing energy waveform [6]. A coaxial cavity was used to modify the time evolution of the energy waveform of an electron beam. We observed the possibility of the output power increase of SR with the modified electron beam.

2. Particle-in-cell simulation

An IREB with energy of 550 keV , current of 5 kA and duration of 12 ns was utilized as an energy source. A cylindrical corrugated waveguide structure for microwave radiation with frequency of 5 GHz was designed for the IREB. The mean radius and periodic length were decided to be 25 mm and 30 mm, respectively, by approximate dispersion relation for 5 GHz microwave radiation with the IREB. Optimum precise parameters were obtained by particle-in-cell simulation code KARAT. The depth of the slot, 6 mm, was simulated to obtain maximum output. The final structure is shown in Fig.1. We set the distance between the beam and inner wall, 2 mm, as small as possible, so that the beam radius was decided to be 20 mm. As the backward wave of TM_{01} mode was expected, the inner radius of the waveguide was decreased to be 22 mm (cut off frequency of 5.2 GHz) to reflect the wave at the entrance of the corrugated part (indicated by A in Fig.1). Gradually increasing radius regions (AB and CD in Fig.1.) were located at both sides of the interaction region to prevent beam electrons and radiated microwave from being reflected by the edges.

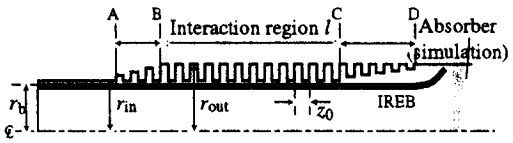

Figure 1: Cross section of the cylindrical corrugated waveguide, $r_b = 20$ mm, $r_{in} = 22$ mm, $r_{out} = 28$ mm, $z_0 = 30$ mm and $l = 300$ mm. At the parts indicated by A-B and C-D, the radius are gradually increased. In the simulation, an absorber was set at the end of the tube.

By the PIC simulation code KARAT, the radiated microwave with frequency of 5 GHz, output power of 600 MW and duration of 4 ns was expected when the electron beam with energy of 550 keV, current of 4.5 kA and duration of 12 ns was injected into the corrugated

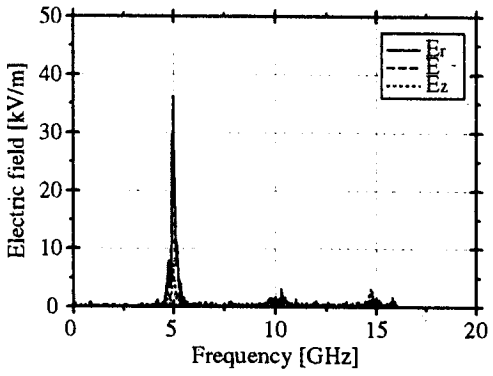

Figure 2: Simulated frequency spectrum of the radiated microwave

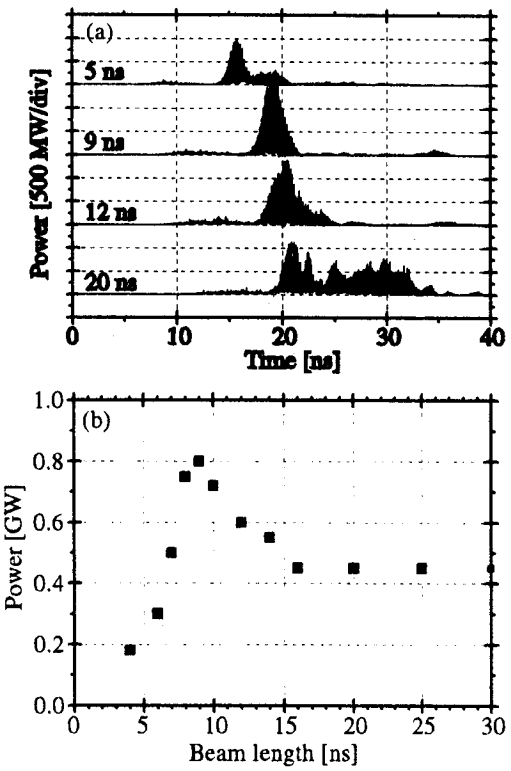

Figure 3: Simulated microwave outputs for different beam lengths. (a)Time dependence of microwave output. (b)The peak output values are plotted against the beam lengths

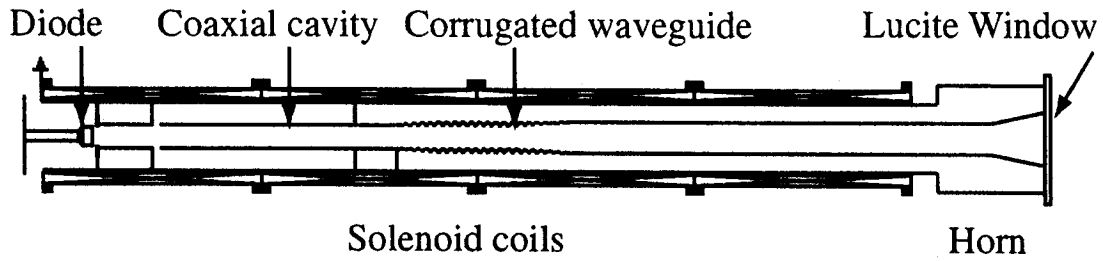

Figure 4: Experimental setup. The coaxial cavity was used only when the experiments with the modified energy waveforms.

waveguide described above. Monochromatic frequency spectrum (Fig.2) and short duration of 4 ns suggested the radiation was caused by SR.

To examine the dependence of the number of electrons to the output power, microwave outputs with different beam lengths were simulated. The plasma frequency of the beam is the important parameter of the radiation, so that the beam current cannot be changed. The beam length instead of the beam current was changed to keep the same plasma frequency. In Fig. 4, it is shown that the simulated peak output power of radiation is proportional to the square of the number of electrons (beam length) as expected in SR. Therefore, the 5 GHz SR was expected in the experiment.

3. Experiments

3.1 Experimental setup

The system was composed of three sections, the diode, the coaxial cavity and the corrugated waveguide as shown in Fig. 4. An annular electron beam of 600 keV, 4.5 kA, 12 ns with diameter of 38 mm and thickness of 2 mm was injected from the diode into a conducting drift tube with inner diameter of 44 mm.

At first, experiments on 5 GHz superradiance were carried out. The coaxial cavity was removed. The corrugated waveguide was connected at 100 mm downstream of the diode.

For the second experiment with modified energy waveforms, the coaxial cavity was inserted at 200 mm from the diode. The principle of the modification of the energy waveform is the same as the autoacceleration scheme [7]. Though the cavity length was changed, the entrance of the corrugated waveguide was located at 1100 mm from the diode for any cavity length. The schematic of the experiment with the modified waveforms is shown in Fig. 4.

In both cases, the microwave was radiated into the air through a Lucite window. The system was immersed in axial magnetic field of 1 T applied by solenoid coils. The base pressure was maintained below 1×10^{-5} Torr.

The radiated microwave was detected by a horn located more than 1 m far from the Lucite window. The microwave received by the horn was attenuated by two variable attenuators. Five low pass filters with frequencies from DC - 4 GHz to DC - 8 GHz were utilized. Tunnel detectors detected microwaves passing through the low pass filters. The variable attenuators, low pass filters and tunnel detectors were calibrated by low power devices. Two band bass filters, 5 ± 0.15 GHz and 5.5 ± 0.15 GHz, were also used.

Fluorescent tubes were utilized to observe the radiation pattern.

3.2 Experimental results and discussions without the coaxial cavity

At first, the coaxial cavity was removed for the experiments of 5 GHz SR. The distance from the diode to the corrugated waveg-

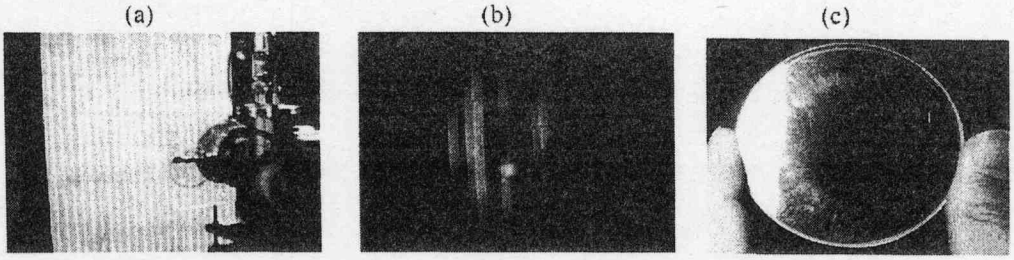

Figure 7: Fluorescent tubes were located 550 mm far from the Lucite window (a). The donut like pattern was observed (b). The damage on the Lucite plate located at the 200 mm downstream side of the corrugated waveguide.

uide was 100 mm. The signals detected by tunnel detectors through low pass filters are shown in Fig. 5. No signal was detected without the corrugated waveguide. With corrugated waveguide, similar signals were detected through DC-5 to DC-8 GHz low pass filters, though no signal was observed through the DC-4 GHz. The signals with and without band pass filters of 5 ± 0.15 GHz and 5.5 ± 0.15 GHz are shown in Fig. 6. The same signals were detected with and without the 5 ± 0.15 GHz band pass filter. The signal was not detected with 5.5 ± 0.15 GHz . Therefore, the frequency of the radiated microwave was around 5 GHz. The detected pulse duration was 5 ns. The microwave signals and the frequency characteristics were not changed by the axial magnetic field from 0.7 T to 1.0 T.

Fluorescent tubes were located 550 mm far from the Lucite window to observe the radiation pattern(Fig. 7(a)). The observed donut like pattern is shown in Fig. 7(b). It agrees with the pattern emitted by the TM_{01} mode. A Lucite plate was set at 200 mm downstream side of the corrugated waveguide. After several shots, the damage pattern as shown in Fig. 7(c) was obtained. The radius of the damage showed a good agreement with that of the maximum electric field of TM_{01} mode in the drift tube.

The horn moved along the circumference

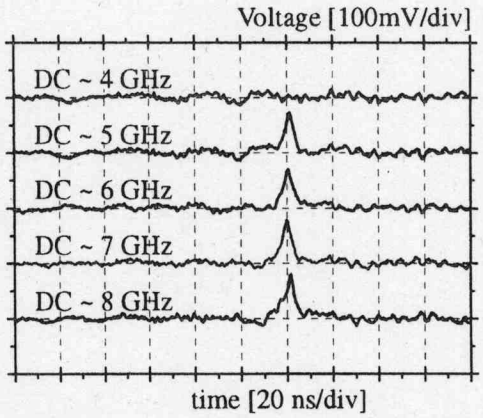

Figure 5: Signals through low pass filters with cylindrical corrugated waveguide

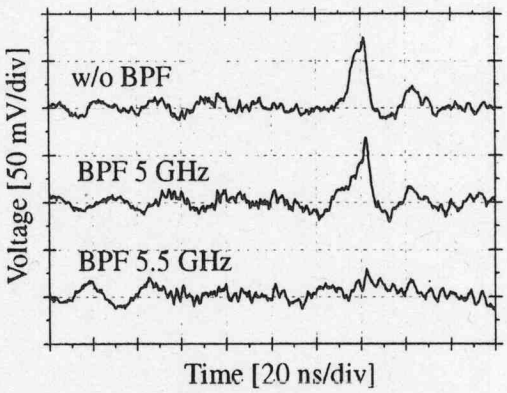

Figure 6: Signals with and without band pass filters

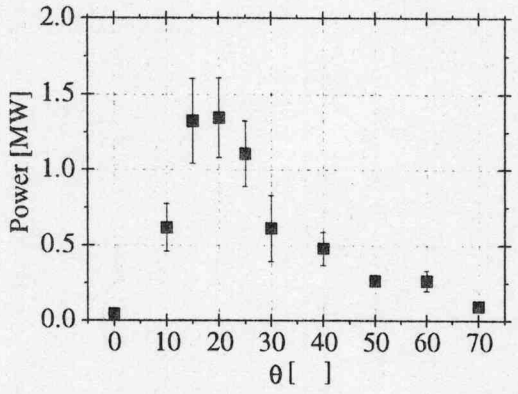

Figure 8: The peak output power was plotted against the angle from the beam axis.

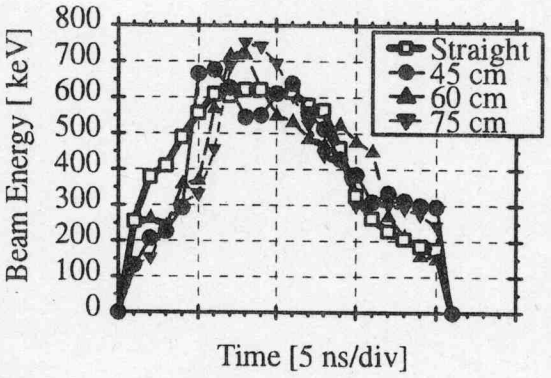

Figure 9: Energy waveforms for different cavity length.

with radius of 1500 mm from the center of the Lucite window to observe the angular distribution of the radiated microwave. In agreement with the observed radiation pattern the microwave output has one peak around 20 degrees from the beam axis as shown in Fig. 8. Total output power of the radiated microwave estimated by the angular distribution was 300 MW.

Table 1: Results

	Experiment	Simulation
Frequency	around 5 GHz	4.98 GHz
Power	300 MW	600 MW
Duration	5 ns	4 ns
Mode	TM_{01}	TM_{01}

The experimental and simulated results are shown in Table 1. The frequency, the duration, the mode and the total power of the radiated microwave were in good agreements with the simulated results of SR. Therefore, we concluded that the 5 GHz SR was observed.

3.3 Experimental results and discussions with the coaxial cavity

For the second experimental stage with the modified electron beam, the coaxial cavity was inserted between the diode and the corrugated waveguide. The distance from the diode to the corrugated waveguide was elongated to be 1100 mm. The gap of the coaxial cavity was covered by a thin pipe when the data without cavity were necessary. Therefore the distance between the diode and the corrugated waveguide always kept to be 1100 mm in the second stage experiment. The energy waveform was modified by the length of the coaxial cavity as shown in Fig. 9. The former part of the beam was decelerated and the latter was accelerated. The duration of each part corresponded to the cavity length. The beam current waveform was little changed by the length of the coaxial cavity. The frequency, the duration and the radiation mode of the radiated microwave were not changed by the length of the cavity.

The angular distribution of the peak output power of the microwave for different cavity length is shown in Fig. 10. The estimated peak output power is plotted against the length of the coaxial cavity in Fig. 11. The lower total power than in the first stage experiment should come from the difficulty of the beam alignment with increase of the distance between diode and slow wave structure to insert the additional cavity. The difference of the total energy in the beam pulse was estimated by the waveforms of the beam energy

transparent cathode. The transparent cathode consists of independent and parallel cathode strips shown in Fig.1. Each live strip caused azimuthal electric field. The enhanced azimuthal electric field at center of vane can cause faster startup and operate longer pulse lengths [5]. The electrons near the cathode strip are accelerated by Lorentz force of this azimuthal magnetic field and the motion of impressed electromotive force. Because the radial drift velocity of electrons is accelerated more than that of electron emitted from general cathode, the new magnetron with transparent cathode should short start up. Additionally, azimuthal electric field penetrates the cathode strips, so the new magnetron should improve operation efficiency.

In this work, preliminary step toward the experimental, we compare new magnetron with transparent cathode to the traditional magnetron with solid cathode by numerical analysis.

2. The model for analysis

Figure 2 shows the conventional magnetron

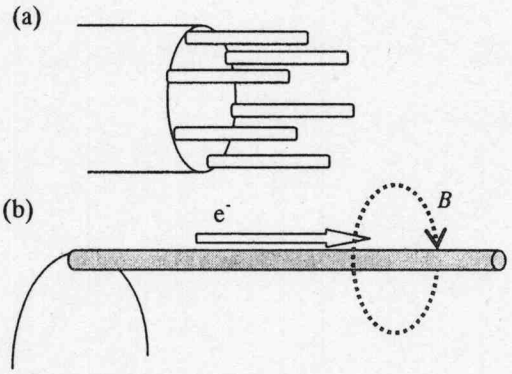

Fig.1. The model of transparent cathode (a)The transparent cathode consists of independent cathode strips. (b)The magnetic effect of transparent cathode near the strip.

consists of a cylindrical anode and an interiorly coaxial cylindrical cathode, and resonator cavities are cut in the anode block. The input power to this device is applied to the center cathode. The emissive electrons would tend to move radially outward to the ring anode surrounds cathode. The figure.1 shows the transparent cathode formed from narrow, parallel longitudinal strips. The number and shape of the resonator cavities and the dimensions of the cathode and anode determine the frequency and operation characteristics of the device. We choose the parameter of well-known A6 magnetron [3]. The parameter of A6 magnetron is the radius of cathode r_c=1.58 cm, radius of anode r_a=2.11 cm, the gap of resonator vanes on the side of anode $\psi = 20°$, and the depth of resonator vans r_v=4.11 cm, shown in Fig.2. The number of resonator vans is M=6. The axial length of body is 7.2 cm, which is decided by the wave length of the operation electromagnetic wave. We assume the operation mode is π -mode (3rd mode) by using anode strap. The fundamental operation mode is shown in Fig.3.

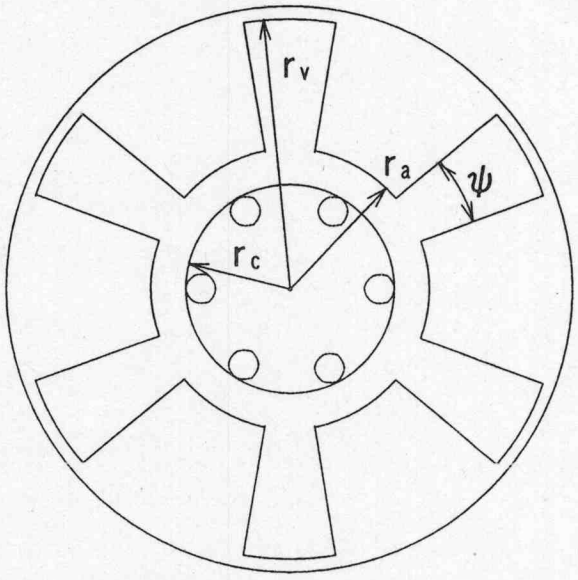

Fig.2. The schematic of magnetron

The external radius of transparent cathode is same to the radius of conventional magnetron cathode r_c. And the number of strips is same to that of resonator vans M.

We will use repetitive pulsed-power generator called ETIGO Ⅳ, which is capable of delivering, to a matched load, an output pulse of 400 kV in voltage, 13 kA in current, and 130 ns in pulse width, at the repetition rate of 1 Hz. The magnetron can oscillate within the certain region of magnetic field prescribed by the Hull and Buneman-Hartree conditions [6]. The parameter space of operation is shown in Figure 4. In general, the Hartree voltage is less than the Hall cutoff voltage magnetic insulation. The magnetic field ranges from Hull cutoff, at about 0.5 T, where oscillations could not be established. The Hartree voltage is corresponds to the breakdown voltage of magnetron in the presence of a rotating perturbation field. The Hartree voltage, at about 0.9 T, causes the perturbation facilitates the motion of electrons across the cathode-anode gap. The potential energy of the electron efficiently interacts with and provides the electromagnetic wave. On this device, A6 magnetron operates in the range 0.5 T to 0.9 T.

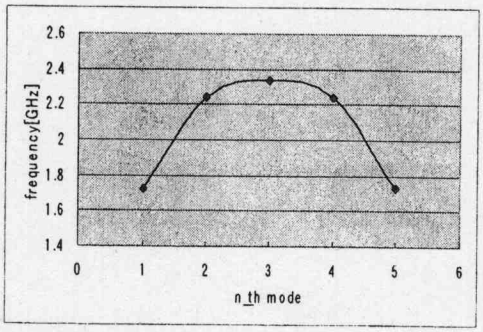

Fig.3. The fundamental mode

3. Discussion

A detailed study was undertaken using the 3D electromagnetic particle-in-cell code MAGIC to investigate the effects by the transparent cathode. In this study, The magnetron with transparent cathode was compared with the general magnetron by cold test, witch was calculated by MAGIC. Figure 5 and Figure 6 shows the distribution of azimuthal electric field caused by the electromagnetic field of operation mode. This figure is a cross section of the part where the resonance vane is included. In the case, the external diameter of transparent cathode and conventional column cathode is the same number, the operation frequency of the magnetron with transparent cathode is different to that of conventional magnetron. The operation frequency of general magnetron is 2.54 GHz, and that of new magnetron with transparent cathode is 2.27 GHz. It is preferable that those operation frequencies are same for more accurate comparing. When we consider the equivalent circuit, it is necessary to expand the interval between the radius of cathode r_c and that of anode r_a. The similar numerical result is obtained

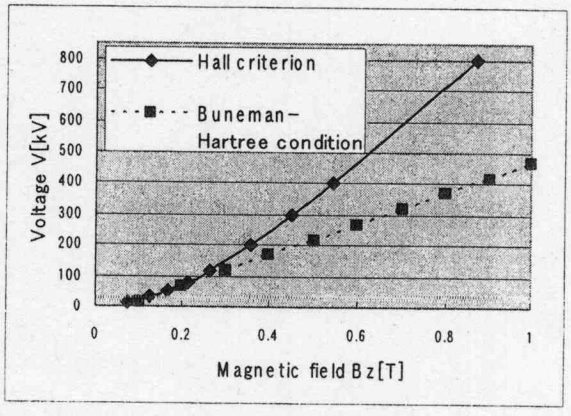

Fig.4. The region of operation of the A6 magnetron

by 3D simulation [4]. The RF electric fields penetrate through the cathode strips, shown in Fig.6. In the region between anode and cathode, the electric field of new magnetron is stronger than that of general magnetron. In the result with transparent cathodes, the larger electric field amplitude in the electron hub region which enhances electron capture into spokes will cause short start-up and more efficiency operation. And this effect may influence the Buneman-Hartree condition as change in condition by this priming of magnetron operation.

The transparent cathode can enhance magnetron efficiency with minimum change from conventional magnetron. In the future, the characteristics of magnetron with transparent cathode are observed, and they will contribute to increasing efficiency of relativistic magnetron.

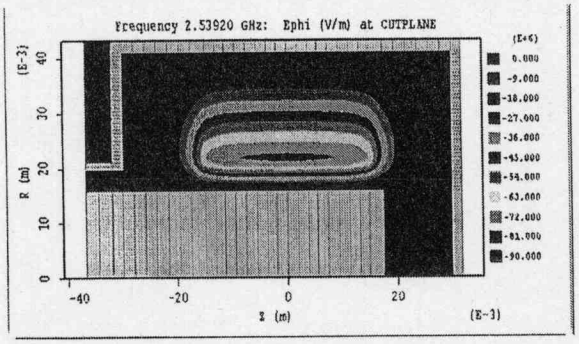

Fig.5. The distribution of azimuthal electric field with old cathode.

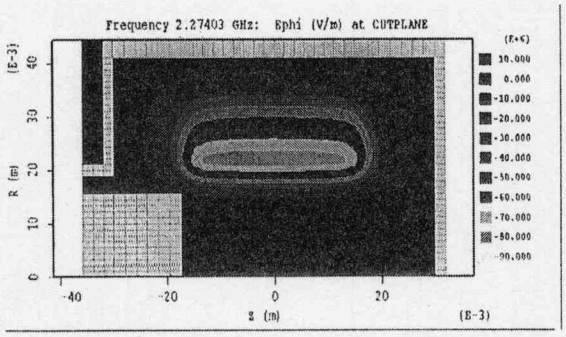

Fig.6. The distribution of azimuthal electric field with transparent cathode.

Reference

1) J. Benford and J. Swegle, "High-Power Microwaves", Artech House, Norwood, MA, 1992

2) S.H. Gold and G.S. Nusinovich, "Review of high power microwave source research", Rev. Sci. Instrum., Vol. 68, No. 11, pp.3945-3974, 1997

3) A. Palevsky and G. Bekefi, "Microwave emission from pulsed, relativistic *e*-beam diodes. II. The multiresonator magnetron", Phys. Fluids, Vol. 22, No. 5, pp.986-996, 1979

4) R.W. Lemke, T.C. Genoni and T.A. Spencer, "Three-dimensional particle-in-cell simulation study of a relativistic magnetron", Phys. Plasmas, Vol. 6, No. 2, pp.603-613, 1999

5) Michael C. Jones, V. Bogdom Neculaes, William M. White, Y.Y. Lau, Ronald M. Gilgenbach, John W. Luginsland, P. Pengvanich, N. M. Jordan, Y. Hidaka and Herman L. Bosman, "Simulations of Magnetic Priming in a Relativistic Magnetron", IEEE transactions on electron devices **52**, pp.858-863, 2005

6) R.V. Lovelace, T.F.T. Young, "Relativistic Hartree condition for magnetrons: Theory and comparison with experiments", Phys. Fluids **28**, pp.2450-2452, 1985

DEVELOPMENT OF HIGH POWER, SHORT PULSE LARGE ORBIT GYROTRON

M. Kamada, T. Hayashi, La Agusu, I. Ogawa, V. N. Manuilov[A], T. Idehara, K. Naito[B], T. Yuyama[B], K. Hashimoto[B], Weihua Jiang[B] and K. Yatsui[B]

Research Center for Development of Far Infrared Region, University of Fukui, 3-9-1 Bunkyo, Fukui 910-8507, Japan
[A]*Radiophysical Department of Nizhny Novgorod State University, 690005, Gagarin av., 23, Nizhny Novgorod, Russia*
[B]*Extremely High-Energy Density Research Institute, Nagaoka University of Technology, 1603-1 Kamitomioka, Nagaoka 940-2188, Japan*

ABSTRACT

A high power large orbit gyrotron is being developed as a millimeter wave and submillimeter wave radiation source. We have designed and constructed a large orbit gyrotron using an intense relativistic electron beam. The output characteristic of the gyrotron is expected frequency of 143.6 GHz, power of 9 MW and cavity mode of TE_{14} by the numerical simulation. Corresponding electron beam has energy of 400 kV and current of 200 A. Preliminary operation of the gyrotron is being examined at fundamental operation. In this paper, results of preliminary tests of the gyrotron are described.

I. Introduction

One of the most important tasks in terahertz technology is development of high power radiation source. A gyrotron is capable of high power radiation in millimeter wave and submillimeter wave region.

The development of gyrotron is being advanced in two ways. One way is the development of high power, millimeter wave gyrotrons for the electron cyclotron heating of fusion plasmas. A gyrotron with a diamond window has achieved output power of 1 MW at 170 GHz by pulsed operation of several second. [1)]

The other way is development of high frequency gyrotrons as millimeter wave and submillimeter wave radiation sources for broad applications. In university of fukui, the gyrotron series has achieved frequency from 38 to 899 GHz. [2)] Output power of the gyrotron series has been from several tens of watts to several tens of kilowatts.

In order develop such high frequency conventional gyrotrons, we usually require high magnetic fields generated by superconducting magnets and operation at second of electron cyclotron frequency. In the case of the conventional gyrotron, higher harmonic operation is difficult to realize, because the efficiency decreases with harmonic number. The third harmonic operation was very rare.

Recently, we have developed a high harmonic gyrotron with an axis-encircling, high power electron beam. [3)] A gyrotron with an axis-encircling electron beam (a so called large orbit gyrotron "LOG" [4)]) is capable of n th harmonic operation (n = 3, 4 ...), because the high efficiency is kept even at high harmonic of electron cyclotron frequency.

Moreover, A gyrotron is capable of high power radiation by using a high power electron beam. A high power LOG is being developed. We use a pulsed power generator "ETIGO-IV" for generation of a high power electron beam. [5)] ETIGO-IV is capable of delivering to matched load an output pulse 400 kV in peak voltage, 13 kA in peak current and 120 ns in pulse length at the repetition rate of 1 Hz.

In this paper, the design of LOG with a high power electron beam, construction and results of preliminary tests are described.

II. Operation mechanism and Advantage of LOG

The LOG is characterized by the trajectory of the electron beam in the cavity it is shown in Fig. 1. A beam electron gyrates around the center axis of the cavity [4)], while in a conventional gyrotron, a beam electron rotates around a gyration center located on a concentric cylinder of cavity. When we use an axis-encircling electron beam and TE_{nm} cavity mode, the interaction the electron beam and the high frequency electromagnetic wave takes place at the n th harmonic. Therefore, we can expect good mode selection, because mode competition with lower harmonics does not occur. This is an importantly advantage, because mode competition is the most severe problem in conventional high harmonic gyrotrons.

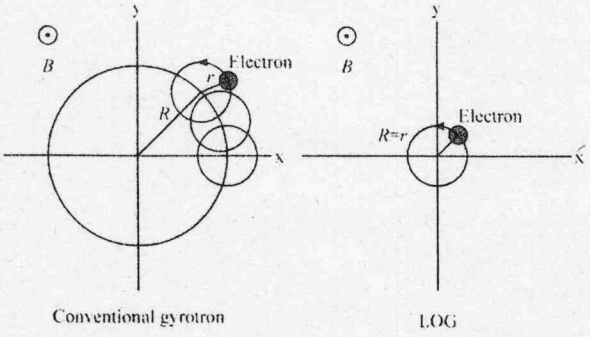

Fig. 1 Trajectory of electron beam in the cavity. Conventional gyrotron (left) and LOG (right). "*R*" means beam radius. "*r*" means lamor radius.

III. Experimental setup

Fig. 2 shows a schematic drawing of the LOG device. Numerical simulation was carried out for optimization of the electron gun, the magnet system and the cavity. [6), 7)]

The electron gun is diode type. An electron beam is generated from a solid cathode by explosive emission. The maximum accelerating voltage is 400 kV. An axis-encircling electron beam is formed passing through thin slit in anode plate and cusp magnetic field. Beam current is controlled by shape of the slit. The cusp magnetic field is produced by combination of five cw coils and a pulse coil. The electron beam is injected into the cavity following to the magnetic field.

Some parameters of the LOG were obtained for fundamental, second harmonic and fourth harmonic operations. Table 1 shows some parameters for three type operations. For fundamental operation, the frequency is 143.6 GHz. Corresponding cavity mode is TE_{14}. The output power is 9 MW. For second harmonic operation, the frequency is 256.7 GHz. Corresponding cavity mode is TE_{24}. The output power is 1.5 MW. For fourth harmonic operation, the frequency is 312.0 GHz. Corresponding cavity mode is TE_{44}. The output power is 0.2 MW.

Table 1 Parameters of cavities.

Harmonic number	1	2	4
Operation mode	TE_{14}	TE_{24}	TE_{44}
Q value	143.6	256.7	312.0
Frequency [GHz]	678	2317	7398
Power [MW]	9.0	1.5	0.2
Efficiency [%]	11.3	6.5	1.7
Cavity radius [mm]	3.90	2.45	2.44
Cavity length [mm]	10.0	10.0	15.0
Magnetic field [T]	8.0	7.6	4.57
Electron energy [kV]	400	381	381
Beam current [A]	200	60	30
Pitch factor	1.51	1.6	1.6

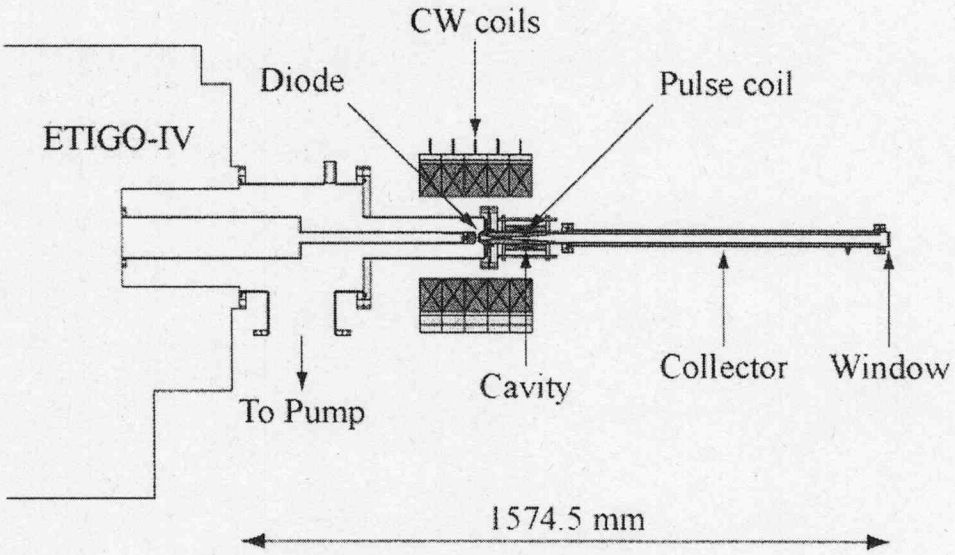

Fig. 2 Schematic drawing of the LOG device.

The inside of the LOG tube is pumped out by an cryogenic pump. The pressure is kept at 10^{-6} torr. A collector is used to monitor the beam current, and the electromagnetic wave generated in the cavity is transmitted along a collector as a circular wave guide. A pyroelectric detector is used to monitor the gyrotron output emitted from a vacuum window.

IV. Experimental results

The preliminary tests of the gyrotron sube have being carried out at fundamental operation. The test results are as follows.

Fig. 3 shows typical diode waveforms. The diode valtage was 400 kV in peak. The diode current was 7 kA in peak. The pulse width was 120 ns. The flattop was not obtained, because evolution of cathode plasmas was effective.

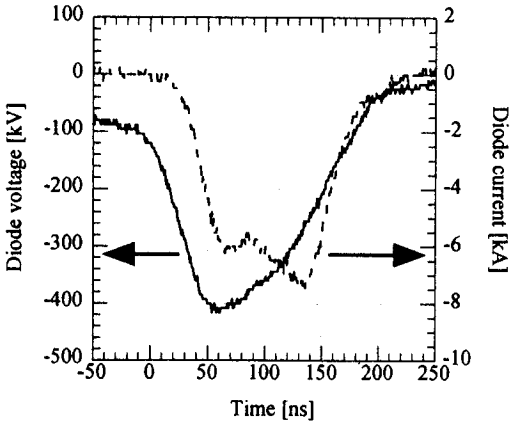

Fig. 3 Diode waveforms (voltage and current).

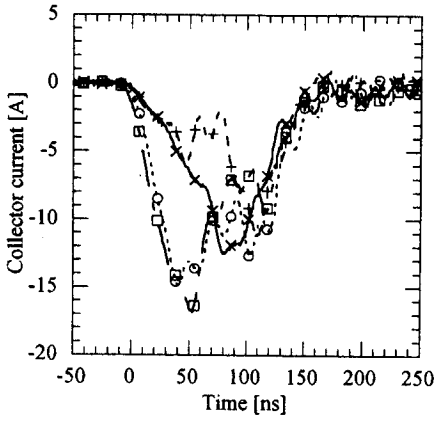

Fig. 4 Collector current.
Without cusp magnetic field.

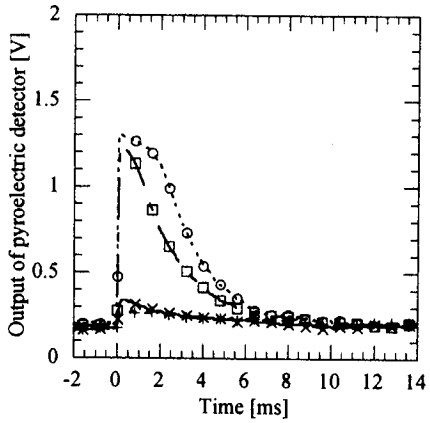

Fig. 5 Output of pyroelectric detector.
Without cusp magnetic field.

The operation test of the gyrotron was carried out in two ways. One way is conventional gyrotron operation without cusp magnetic field. Additional cw coils was not used. Main pulse magnetic field was adjusted to 8 T. Fig. 4 shows collector currents. Four shots were monitored at the same condition, but waveforms had two types of variation with current of several A. Fig. 5 shows output voltage of pyroelectric detector at the same shots in Fig. 4. If peak of beam current was around diode voltage of 400 kv, output voltage of the pyroelectric detector was higher. But, pyroelectric detector does not have fast time response. Therefore, we could not fine the detail of information of gyrotron output.

The other way is large orbit gyrotron operation with cusp magnetic field. Current of the additional cw coils was 240 A. Main pulse magnetic field was adjusted to 8 T. The cusp point was between the cathode and the anode. Fig. 6 shows collector currents. Two shots ware monitored at the same condition. Fig. 7 shows output voltage of pyroelectric detector at the same shots in Fig. 6. output of the pyroelectric detector was not obtained, because beam current was only 0.5 A.

In the experiments, the electron trajectory was not optimized, because the electrooptic system of electron gun was changed by space charge effect.

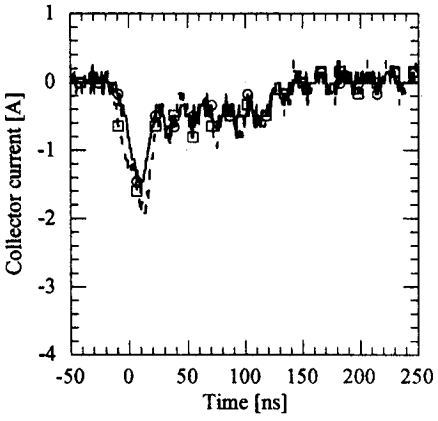

Fig. 6 Collector current. With cusp magnetic field.

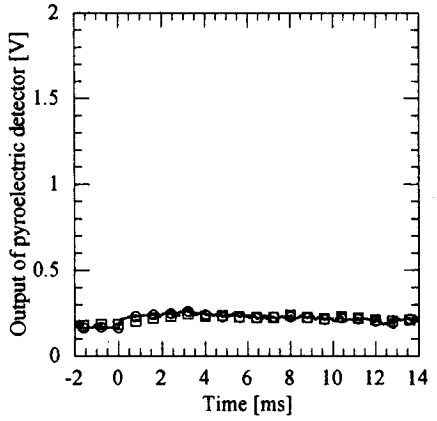

Fig. 7 Output of pyroelectric detector. With cusp magnetic field.

V. Conclusion

We have constructed a large orbit gyrotron (LOG) with a pulsed power electron beam. The electron gun and the profile of the magnetic field ware designed for generation of a high quality axis-encircling electron beam with a small ripple and large pitch factor. Experimental test was carried out for fundamental operation. A cavity was optimized for TE_{14} cavity mode.

Expected beam current was 200 A, but obtained beam current was 0.5 A in LOG operation. Therefore, radiation power was very low. The optimization of electrooptic system of electron gun is need in experiments.

Acknowledgment

This work was partly supported by Grant in Aid from JSPS (Japan Society for the Promotion of Science).

Reference

1) K. Sakamoto, A. Kasugai, M. Tsuneoka, K. Takahashi and T. Imai, "High power 170 GHz gyrotron with syinthetic diamond window", Rev. Sci. Instrum., Vol. 70, No. 1, Pt. 1-2, 208-212 (1999).

2) T. Idehara, I. Ogawa, S. Mitsudo, M. Pereyaslavets, N. Nishida and K. Yoshida, "Development of frequency tunable, medium power gyrotrons (Gyrotron FU Series) as submillimeter wave radiation sources", IEEE Trans. Plasma Sci., Vol. 27, No. 2, 340-354 (1999).

3) T. Idehara, I. Ogawa, S. Mitsudo, Y. Iwata, S. Watanabe, Y. Itakura, K. Ohnishi, H. Kabayashi, T. Yokoyama, V. F. Zapevalov, M. Y. Glyavin, A. N. Kuftin, O. V. Malygin and S. P. Sabchevski, "A High Harmonic Gyrotron With an Axis-Encircling Electron Beam and Permanent Magnet, IEEE Trans. Plasma Sci., Vol. 32, No. 3, 903-909 (2002).

4) D. B. McDermott, N. C. Luhmann, A. Kupiszewski and H. J. Jory, "Small-signal theory of a large-orbit-electron-cyclotron harmonic maser", Phys. Fluids, Vol. 26, No. 7, 1936-1941 (1983).

5) A. Tokuchi, N. Ninomiya, W. Jiang and K. Yatsui, "Repetitive Pulsed-Power Generator ETIGO-IV", IEEE Trans. Plasma Sci., Vol. 30, No. 5, 1637-1641 (2002).

6) V. N. Manuilov, T. Idehara, M. Y. Glyavin, La Agusu, M. Kamada, T. Kanemaki, W. Jiang and K. Yatsui, "Electron optic system of powerful large orbit gyrotron with pulse magnetic field", Int. J. Infrared Millim. Waves, Vol. 26, No. 1, 15-28 (2005).

7) La Agusu, T. Idehara, M. Kamada, T. Hayashi, V. N. Manuilov, O. Dumbrajs, W. Jiang and K. Yatsui, "Design of Cavities for a Short Pulse Powerful Large Orbit Gyrotron", Int. J. Infrared Millim. Waves, Vol. 26, No. 5, 637-655 (2005).

Three-Dimensional Particle-in-Cell Simulation of Large Orbit Gyrotron

Keisuke Naito, Weihua Jiang, and Kiyoshi Yatsui
Extreme-Energy Density Research Institute, Nagaoka University of Technology, Japan
Masaki Kamada and Toshitaka Idehara
Research Center for Development of Far-Infrared Region, University of Fukui, Japan

Abstract

We are studying large orbit gyrotron (LOG) as an oscillator for far-infrared radiation. LOG is a gyrotron that uses axis-encircling electron beam whose guiding center situates on the center axis. Numerical simulations were performed using the particle-in-cell simulation code "MAGIC". The simulations were carried out by dividing LOG into two portions, the electron beam diode and the interaction cavity. The electron beam parameters obtained by two-dimensional simulations of the electron beam diode are used as the boundary conditions for the three-dimensional simulations of the interaction cavity. The simulation was performed in the range of intensity of magnetic field of 6-8 T. As the results, output power can expect about 1 MW at about 100 GHz. The simulation results were used to perform experimental device design and to understand the general behaviors of LOG.

Keywords- far-infrared radiation, electron beam, Large Orbit Gyrotron , terahertz radiation

I. INTRODUCTION

High power microwave (HPM) sources have various applications in thermal nuclear fusion, pulsed radar, particle acceleration, wireless power transmission, and other industrial and military fields. Among many kinds of HPM generators, gyrotron has advantages in high efficiency and high frequency[1].

Gyrotron is a microwave oscillator that makes use of the electron cyclotron motion in a magnetic field. The oscillation happens when the electron-beam bunching occurs at the resonant frequency. For this reason, the oscillation frequency depends on the strength of the applied magnetic fields.

Gyrotron is considered to be a potential source for powerful radiation in far-infrared region.[2] Electromagnetic waves in this frequency range are expected to have many applications in new-material development, advanced analysis, and plasma diagnostics. The challenge of using gyrotron for generation of far-infrared radiation is achieving high frequency and mode control.

For example, the electron cyclotron frequency in THz range corresponds to a magnetic field on the order of tens of Teslas, which is very difficult to obtain experimentally. A practical method to multiply the oscillation frequency without increasing the magnetic field is making use of the higher harmonic modes. However, due to strong mode competition, the experimentally obtained efficiency for higher harmonics is usually very low for conventional gyrotrons.

Large Orbit Gyrotron (LOG) is a special type of gyrotron, where the electron cyclotron radius equals the beam radius. Due to this unique property, it is theoretically expected that the mode competition can be effectively controlled so that the higher harmonic wave efficiency can be significantly increased.

In this paper, a LOG is studied by simulation code "MAGIC",[3] which is a fully electromagnetic, relativistic, particle-in-cell simulation code widely used for plasma and particle beam studies. The simulations are carried out for electron-beam parameters of pulsed power generator "ETIGO-IV",[4] i.e., diode voltage of 400 KV, diode current of 13 kA, and pulse width of 120 nsec.

In the simulation, the LOG is divided into two portions, an electron-beam diode and an interaction cavity. The diode is studied by using two-deimensional simulations and the interaction cavity is studied by using three-dimensional simulations. This paper reports our recent simulation results of the electron-beam diode and the interaction cavity.

II. NUMERICAL SIMULATIONS

A. *Structure of large orbit gyrotron (LOG)*[5][6][7]

The general view of LOG under present development is shown in Fig. 1. A CW coil generates magnetic field for forming the helical electron beam and a pulsed coil provides strong magnetic field for the interaction cavity. When a high voltage is applied between the anode-cathode gap, an electron beam is extracted from the cathode and accelerated toward the anode. Since the cathode is in a cusped magnetic field, the electrons have large component of momentum perpendicular to the magnetic field when they reach the anode. The gradient of the axial magnetic field between the anode and the cavity further increases the perpendicular component of the electron momentum and compresses the electron beam diameter. The ideal

situation at the cavity entrance is a thin electron beam having a cyclotron radius that equals to the beam radius and a cyclotron frequency that resonates with the cavity.

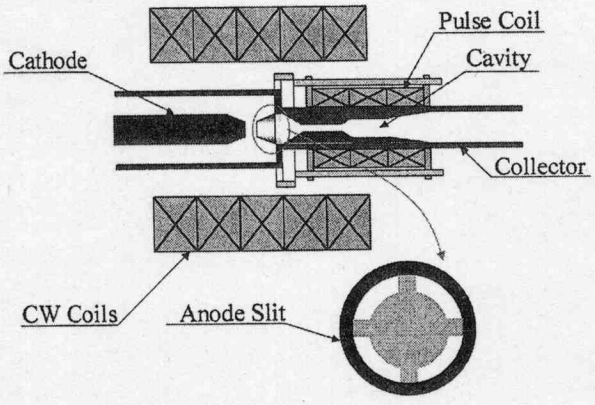

Fig.1 The general view of LOG

B. Particle-in-cell simulation[8][9]

The simulation model of the electron diode and its distribution of the intensity of the magnetic field are shown in Fig. 2. It is axially symmetric and the simulation is carried out in 2.5-dimensional cylindrical coordinate. Across the anode slit, an aluminum foil of 1.0 nm in thickness is used in order to define the electrical potential of the inner part of the anode. Electrons are emitted from the cathode surface facing the anode. Both electrodes are considered as perfect conductors.

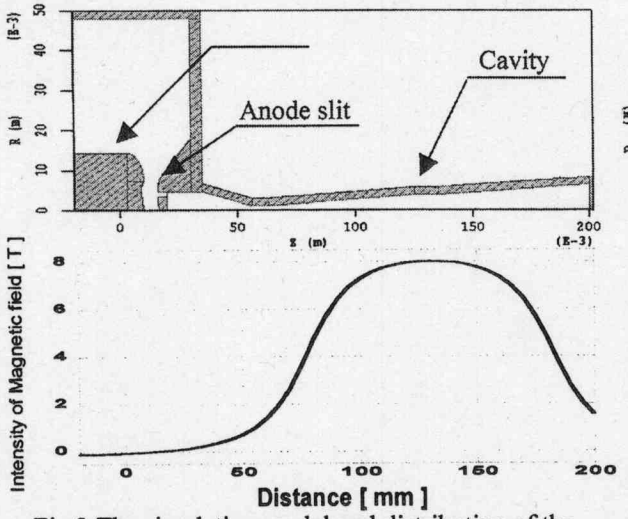

Fig.2 The simulation model and distribution of the magnetic field of the electron beam diode.

The applied voltage is 320 kV, which is the output voltage range of "ETIGO- IV ". However, for simplicity, a constant voltage is used instead of the real waveform. The cell size is 0.1 × 0.1 mm and the simulation time is 4 ns. The applied magnetic field is varied in the rang of 6-8 T, which is the output magnetic field range of our coils, typical distribution on the center axis is also that shown in Fig. 2 (z = 5 is the emission surface).

The current of the CW coils and pulse coil changes this magnetic field distribution. The CW coils changes the position of the cusp region. The pulse coil changes the peak intensity of the magnetic field and distribution of magnetic field.

The electron map obtained from the simulation is shown in Fig. 3. From Fig. 3, it is seen that the electrons are emitted from the cathode and only a small portion of them can pass through the anode slit. From Fig. 3(a), the electrons reached the right boundary of the simulation model are only a small portion, because the electrons passed through the anode slit impact the tube. In contrast, from Fig. 3 (b), the rate of electrons impacted the tube is decreased.

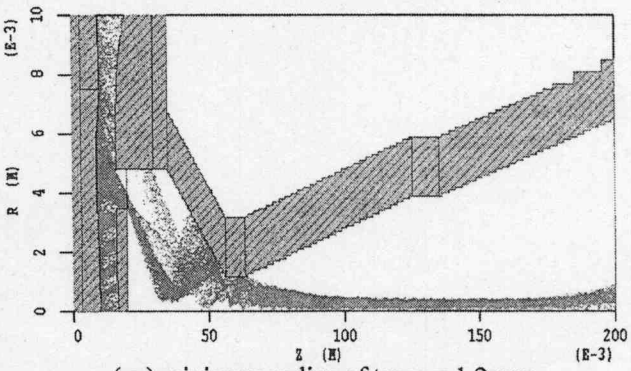

(a) minimum radius of taper = 1.2 mm

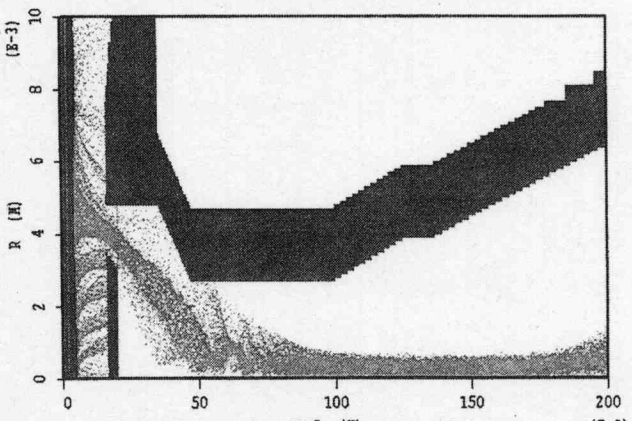

(b) minimum radius of taper = 2.7 mm

Fig. 3 The electron map obtained by the simulation.

The electron beam parameters, electron momentum parallel to the magnetic field (P_z), perpendicular to the magnetic field (P_ϕ) and beam current are shown in Fig. 4. And the dependence of the electron beam momentums on the distance is shown in Fig. 5. From Fig. 4, the annular beam that incidence of the interaction cavity is a very little current, and P_z tend to increase and P_ϕ tend to decrease. And from Fig. 5, the electron beam exhibits large energy spread which is considered to be caused by the space charge effect and mirror effect. Therefore, it is necessary to improve the diode configuration.

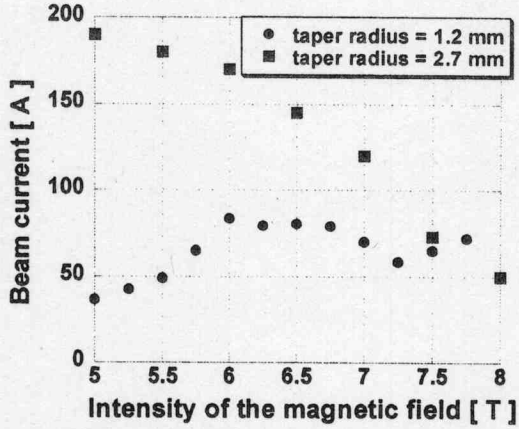

(a) Dependence of beam current on magnetic field

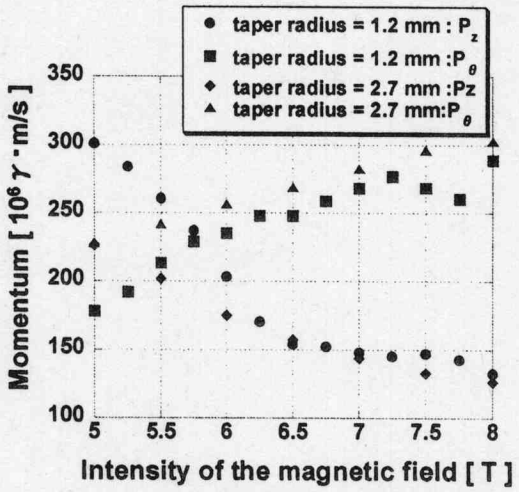

(b) Dependence of electron momentum on magnetic field

Fig. 4 The electron beam parameters

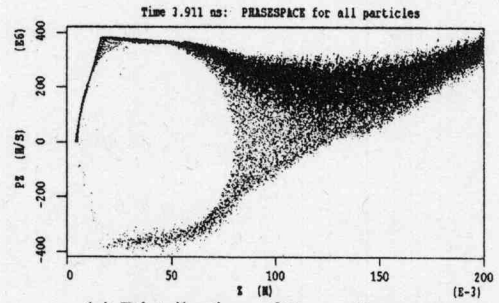

(a) Distribution of P_z on distance.

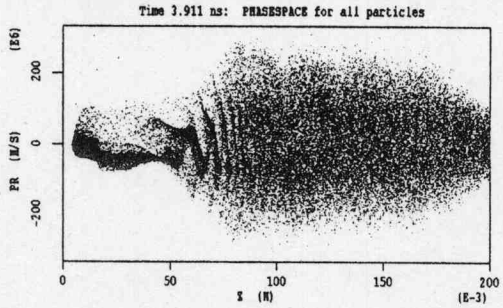

(b) Distribution of P_r on distance.

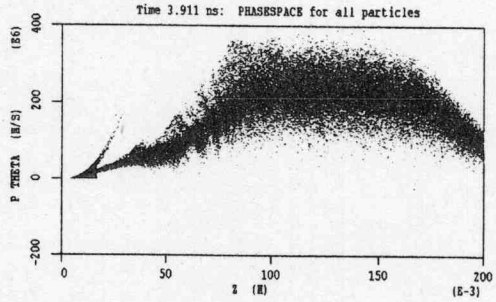

(c) Distribution of P_ϕ on distance.

Fig. 5 Distribution of electron momentum on distance

The simulation model for interaction cavity is shown in Fig. 6. It is axially symmetric and the simulation is carried out in three-dimensional cylindrical coordinate. The objects are considered as perfect conductors. An electron beam which had beam current equals to 25 A and pitch-factor of 1.5 is injected from the left boundary. The cell size is $0.1\text{mm} \times 0.1\text{mm} \times 0.0625\,\pi$ and simulation time is 4 ns. The applied magnetic field is the same as that of the diode model.

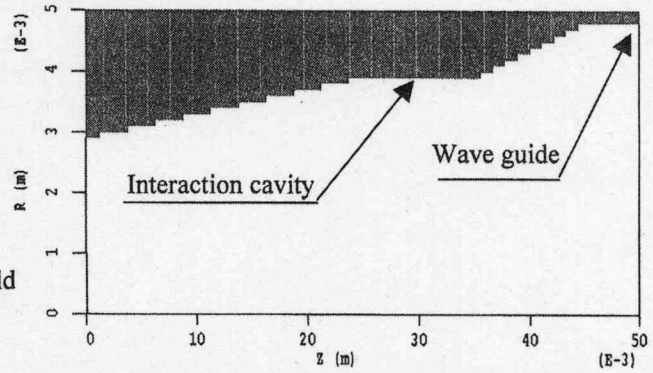

Fig. 6 The simulation model of interaction cavity

The electron map obtained from the simulation is shown in Fig. 7. From Fig. 7, the electron beam breaks down its form a little and has a certain thickness.

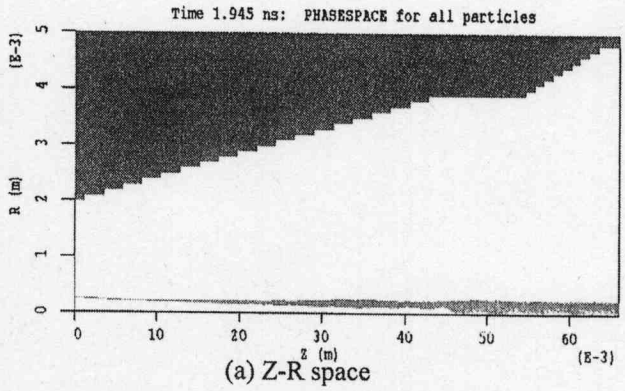

(a) Z-R space

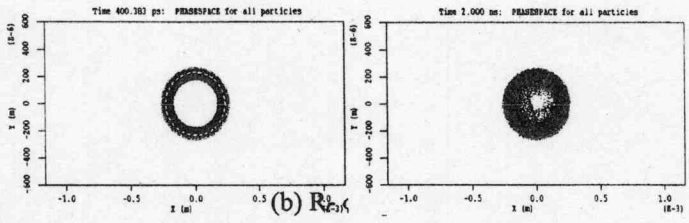

(b) Ri

Fig. 7 The electron map obtained by simulation

Figure 8 shows the time history of the electric field E_ϕ. Electromagnetic wave generation is verified by the strong oscillatory behavior of the electric field as seen in Fig. 8 (a). Fig. 8 (b) shows the frequency spectrum of the electromagnetic wave by the FFT of the Fig. 8 (a).

The dependence of oscillation frequency on intensity of magnetic field is shown in Fig. 9. As a result, in the range from 6 to 8 T, it turns out that it is not single mode oscillation. As a cause, it is thought to the parameter of the electron beam that is carrying out incidence that the form of interaction cavity is not the optimal. About this, it is due to improve from now on.

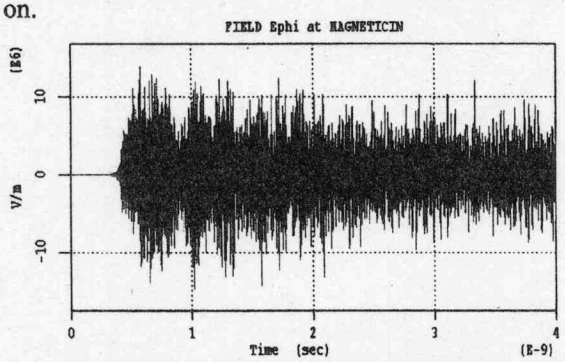

(a) The time history of the electric field E_ϕ

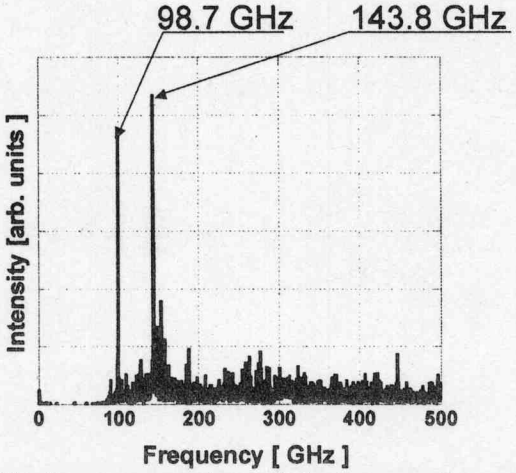

(b) The frequency spectrum of electromagnetic wave was calculated by FFT

Fig. 8 The oscillation frequency

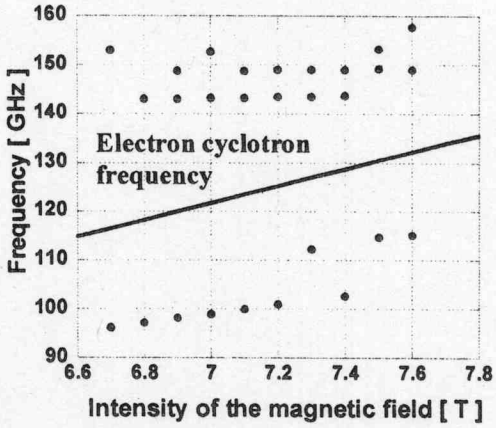

Fig. 9 Dependence of oscillation frequency on magnetic field.

Figure 9 shows the typical waveform of output electro-magnetic power and dependence of output power on intensity of magnetic field obtained by the simulation. The Poynting vector measured at the outlet of waveguide determines the electromagnetic power. As the results, output power can expect about 1 MW.

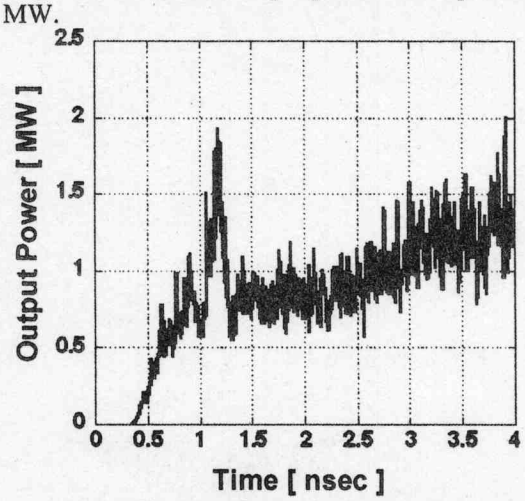

(a) The waveform of output power

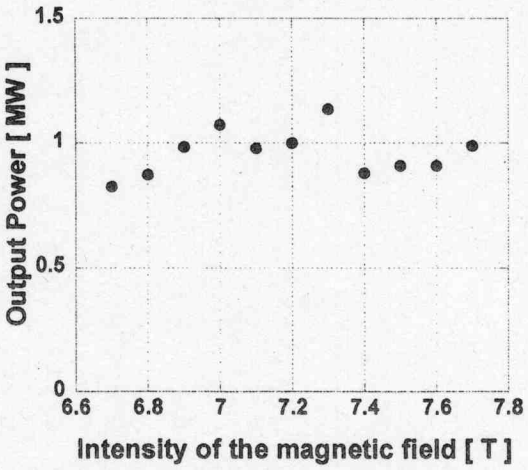

(b) Dependence of output power on magnetic field

III. CONCLUSIONS

Numerical simulations are carried out for large orbit gyrotron (LOG). The simulation model divides the LOG into two portions, the electron diode and the interaction cavity. This paper reports the simulation results on the diode and the interaction cavity. As a result, electron beam from the diode exhibits large energy spread which is considered to be caused by the space charge effect and some mirror effects. It is necessary to improve the diode configuration.

Output power and frequency of the electromagnetic wave are obtained to be ~ 1 MW and ~ 150 GHz, respectively. However, it turns out that, its frequency spectrum had two or more peaks are identified by the FFT and not a single mode oscillation.

REFERENCES

[1] Steven H. Gold, Gregory S. Nusinovich, "Review of high power microwave source research" Rev. Sci. Instrum, Vol.68 , No.11 , pages 3945-3974 (1997)

[2] Y. Itakura, T. Idehara, Y. Yasuoka, " Modern technologies in the far infrared region " , IEEJ Trans. FM (in Japanese), Vol.123, No.10, pages 949-954 (2003)

[3] L. Ludeking, D. Smithe, M. Bettenkausen, S.Hayes, "MAGIC USER'S MANUAL" , Mission Research Co. (1999)

[4] A. Tokuchi, N. Ninomiya, W. Jiang, K. Yatsui, "Repetitive Pulsed-Power Generator ETIGO-IV" , IEEE Trans. Plasma Science, Vol.30, No.5, pages 1637-1641 (2002).

[5] T. Idehara, V.N. Manuilov, O. Watanabe, M. Kamada, La Agusu, K. Yatsui and W. Jiang, "Electron gun for powerful large orbit gyrotron" , Int. J. Infrared and Millimeter Waves, Vol. 25, No. 1, 3-14 (2004).

[6] La Agusu, T. Idehara, M. Kamada, T. Hayashi, V.N. Manuilov, O.Dumbrajs, K. Yatsui and W. Jiang, "Design of cavities for a short pulse powerful large orbit gyrotron" , Int. J. Infrared and Millimeter Waves, Vol. 26, No. 5, 637-655 (2005).

[7] James Benford, John Swegle, "High-Power Microwaves" , Artech House, pages 261-306 (1991)

[8] K. Naitou, W.Jiang, K. Yatsui, M. Kamada, T. Idehara " Three dimentional Particle-in-Cell simulation of Large Orbit Gyrotron " , The 4th Asia-Pacific International Symposium on the Basics and Applications of Plasma Science and Technology, pages 369-373 (2005)